

INTRACELLULAR FORCES AND NUCLEAR MECHANOBIOLOGY DURING
CONFINED CELL MIGRATION IN 3-DIMENSIONS

A Dissertation

Presented to the Faculty of the Graduate School

of Cornell University

In Partial Fulfillment of the Requirements for the Degree of
Doctor of Philosophy in the Field of Biomedical Engineering

by

Jeremy Thomas Keys

August 2022

© 2022 Jeremy Thomas Keys

INTRACELLULAR FORCES AND NUCLEAR MECHANOBIOLOGY DURING CONFINED CELL MIGRATION IN 3-DIMENSIONS

Jeremy Thomas Keys, Ph. D.

Cornell University 2022

Cell migration is a required step in many biological and pathological processes.

During wound healing, embryogenesis, and immune surveillance, cells migrate to sites where they can repair, develop, and protect tissues, which are all essential for maintaining healthy physiology. In contrast, during cancer metastasis, individual cancer cells escape from the primary tumor and migrate into blood and lymphatic vessels, where they spread through the body to form secondary tumors. This process of cancer metastasis is responsible for 90% of cancer related deaths. Despite its centrality to these essential phenomena, there is still much that is unknown about how cells migrate *in vivo*.

The nucleus limits the rate at which cells can migrate through tissues, as it is the largest and stiffest organelle in the cell. As cells move through narrow spaces in the dense matrix of endothelial cell layers and extracellular fibers that make up biological tissues, they must apply considerable intracellular force to squeeze the nucleus through these spaces. It is still unclear how exactly cells apply sufficient force to complete this deformation of the nucleus through constrictions.

Here, we established a microfluidic platform for studying nuclear deformation through precisely defined constrictions. Using this platform, we demonstrate evidence of a novel mechanism by which cells push their nucleus through constrictions through contraction of the rear cortex. We subsequently demonstrate that contraction of the rear cortex induces nuclear blebbing in cancer cells through pressure-driven nuclear influx. This rear cortex-contraction mechanism is significant as it represents a previously unrecognized mechanism which enables confined migration, opening future avenues of study which can inform the treatment of metastatic cancer.

We also used this microfluidic platform to evaluate the viability of engineered enucleated mesenchymal stromal cells (MSCs) as a targeted therapeutic delivery system. This work revealed that enucleated cells showed improved invasive ability in comparison to their nucleus-containing counterparts. These findings are significant in that they both support the use of these enucleated MSCs as a targeted therapeutic delivery platform, and that they revealed that cells do not require a nucleus to migrate through 3D constrictions.

Later, we assessed the impact of nuclear size restoring compounds on the invasion of prostate cancer cells. This work identified compounds which reversed nuclear size defects commonly observed in cancer cells, and reduced migration in 2D wound healing assays and Boyden chambers, but not through microfluidic constrictions.

While ample evidence has shown that the deformability of the nucleus limits its ability to squeeze through constrictions, changes in nuclear size have not shown a consistent

relationship with cell's invasive ability. These findings are significant as they provide evidence that a variety of compounds may present viable treatments for reducing the metastatic capacity of some cancer cell lines. However, it is unclear whether the principal mechanism which reduces migration is directly related to the observed changes in nuclear size.

This thesis expands the existing knowledge on the role of the nucleus in confined migration, and the impact of intracellular force generation on nuclear movement.

BIOGRAPHICAL SKETCH

Jeremy Keys received his Bachelor's Degree in Mechanical Engineering from the University of Massachusetts Amherst in 2016. As an undergraduate, Jeremy pursued a diverse array of scientific (and non-scientific) interests, including developing surgical tools for sports medicine injuries during a Co-Op at Johnson and Johnson, designing a retrofitted seatbelt system for buses in the UMass Center for eDesign, working with the UMass Independent Film Production Club, and teaching with the UMass Center for Teaching and Learning. His work in the lab of Dr. Maureen Lynch at the University of Massachusetts helped to launch his career in biomedical engineering research, where he studied the biophysical interplay between bone metastases and native bone cells. In this work, Jeremy developed an interest in how human cells interact with the mechanical environment, and how those interactions presented opportunities for improving the treatment of human disease. In Dr. Jan Lammerding's lab at Cornell University, he found the ideal space in which to continue those pursuits. The Lammerding Lab is an interdisciplinary research group which studies human disease, especially cancer metastasis and muscular dystrophy, through the lens of cell-level biomechanics. In this lab, Jeremy applied his mechanical engineering background to improve the understanding of how individual cancer cells generate intracellular forces to migrate through constrictions, informing principal mechanisms which may drive the metastatic process. Upon the completion of his doctoral studies, Jeremy will pursue his interest in teaching at the college level at Northwestern University, where he will work as an Assistant Professor of Instruction in the Department of Mechanical Engineering.

Dedicated to my Mom and Dad, who together instilled in me both a love of science and the importance of having compassion for others, both of which have been invaluable to me in my growth as a scientist and as a person.

ACKNOWLEDGMENTS

I would like to thank my research advisor, Dr. Jan Lammerding, for his unparalleled and unwavering support throughout my time at Cornell. His boundless enthusiasm was crucial to my success, as he helped me to maintain a positive attitude towards my research and my future, even during the most challenging periods of my graduate work. Jan's commitment to supporting his students is remarkable, making time to answer scientific questions or provide words of encouragement at truly any hour of the day. I would also like to thank my committee members, Dr. Matthew Paszek and Dr. Mingming Wu, for their scientific insights and support throughout my PhD. I would also like to thank all the members of the Weill Institute for Cell and Molecular Biology, the Nancy E. and Peter C. Meinig School of Biomedical Engineering (especially Dr. Warren Zipfel and Dr. Rebecca Williams for their support of my microscopy work, and Belinda Floyd for supporting my transition into graduate school), and the Weill Hall Building Staff for making all of my work possible.

My work in the Lammerding Lab was made possible by learning through many of the exceptional scientists who I have had the pleasure of working with over the past 6 years, including Philipp Isermann, Dr. Gregory Fedorchak, Dr. Ashley Earle, Dr. Alexandra McGregor, Dr. Jeremiah Hsia, Dr. Pragya Shah, Dr. Tyler Kirby, Dr. Emily Bell, Dr. Laith Kadem, Dr. Melanie Maurer, Dr. Noam Zuela-Sopilniak, Dr. Alexander Sopilniak-Mints, Jawuanna McAllister, Maggie Elpers, Dr. Hind Zahr, Dr. Alice Anais-Varlet, Dr. Julien Morival, Dr. Julie Heffler, Jacob Odell, Richa Agrawal, Hannah Fong, and Aaron Windsor. The Lammerding Lab has always been a joy to

work in due to the kindness of everyone listed above, and I cannot thank you all enough for that.

I must also extend a thank you to my many collaborators who have played a key role in expanding the scientific opportunities that I was able to work on during my graduate thesis, including Brian Cheung and Dr. Mingming Wu of Cornell University, Dr. Panagiotis Mistriotis, Dr. Emily Wisniewski, and Dr. Konstantinos Konstantopoulos of Johns Hopkins University, Dr. Eric Schirmer of the University of Edinburgh, and Dr. Huawei Wang and Dr. Richard Klemke of the University of California San Diego School of Medicine.

My research would not have been possible without the financial support provided by the Kavli Institute at Cornell, through the Knight@KIC Graduate Fellowship program.

To complement my graduate research, I had the pleasure of pursuing many teaching opportunities which will be invaluable in my future career, teaching at the university level. I would like to thank Dr. Yadong Wang, who supported me through my teaching assistantship through the uniquely turbulent spring 2020 semester. I am thankful for the support of Jennifer Davis, who gave me the opportunity to teach online courses on Intro to Engineering and Intro to Biomedical Engineering through the Cornell Adult University Teen and Youth program. I would also like to thank Dr. Celia Evans, Katie Adler, Andrew Kang, and all of the other members of the

Engineering Learning Initiatives group for enabling my role as a TA Development Consultant, where I was able to develop my skill and confidence as an educator.

I am extremely grateful for the friendships that helped me through my many years at Cornell: from my fellow (and former) graduate students, especially Dr. Sarah Snyder and Matthew Tan for their exceptional kindness (and occasional dog-sitting services); from my many friends (human and canine) at the Ithaca Dog Park, especially Tom Blecher; for Dr. Corey Myler and the exceptional support of Cornell's CAPS program; and for everyone else who helped me made my journey here possible who I neglected to mention by name. And finally, I am most grateful for the loving support of my partner, Amaris Cuchanski, who has made my last year at Cornell an absolute joy, and whose kindness makes every day brighter than the last.

LIST OF ABBREVIATIONS

| | |
|-----------|---|
| 2D | Two Dimensional |
| 3D | Three Dimensional |
| BFP | Blue Fluorescent Protein |
| FRET | Förster-Resonance Energy Transfer |
| GFP | Green Fluorescent Protein |
| GTP | Guanosine Triphosphate |
| LINC | Linker of Nucleoskeleton and Cytoskeleton |
| MEF | Mouse Embryonic Fibroblast |
| MLC | Myosin Light Chain |
| MSC | Mesenchymal Stromal Cell |
| NSR | Nuclear Size Rectifier |
| PDMS | Poly dimethyl siloxane |
| pMLC | Phosphorylated Myosin Light Chain |
| RhoGTPase | Rho family guanosine triphosphate-binding protein |
| ROCK | Rho-associated protein kinase |

TABLE OF CONTENTS

| | |
|--|-----|
| BIOGRAPHICAL SKETCH..... | iv |
| ACKNOWLEDGMENTS..... | vi |
| SUMMARY | xi |
| CHAPTER 1 - INTRODUCTION | 15 |
| CHAPTER 2- ASSEMBLY AND USE OF A MICROFLUIDIC DEVICE FOR THE STUDY OF CONFINED MIGRATION..... | 29 |
| CHAPTER 3- CONTRACTION OF THE REAR CORTEX SUPPORTS CONFINED MIGRATION THROUGH A PRESSURE INDUCED NUCLEAR TRANSIT MECHANISM | 58 |
| CHAPTER 4- PRESSURE IN THE POSTERIOR COMPARTMENT OF MIGRATING CELLS INDUCES NUCLEAR INFLUX..... | 107 |
| CHAPTER 5 – ENUCLEATED CELLS INVADE MORE RAPIDLY THROUGH CONSTRICTIONS | 141 |
| CHAPTER 6 - EFFECTS OF NUCLEAR SIZE RECTIFYING COMPOUNDS ON CONFINED MIGRATION..... | 169 |
| CHAPTER 7 – CONCLUSIONS AND PERSPECTIVES | 191 |
| APPENDIX A: NUCLEAR POSITIONING IN HL-60S DURING CONFINED MIGRATION | 197 |
| APPENDIX B: TEACHING AND OUTREACH..... | 202 |
| REFERENCES..... | 215 |

SUMMARY

Chapter 1: Introduction. I provide an introduction to the role of intracellular forces in confined migration, and how these forces interact with the cell nucleus. I discuss the biological signaling which enables force generation within cells and how those forces are transmitted to the environment. I summarize current literature which describes the role of the nucleus in confined migration, and how various cytoskeletal structures apply pushing and pulling forces to mediate nuclear transit through constrictions. I then list a set of tools which have been developed to study intracellular force generation, and how these tools can be applied to the study of nuclear transit.

Chapter 2: Assembly and Use of a Microfluidic Device for the Study of Confined Migration. I describe the design and utility of a microfluidic device which can aid in the study of confined cell migration. I outline the necessary steps to produce a microfluidic device using photolithography and soft lithography techniques. Then, I demonstrate how such a device can be coated with extracellular matrix proteins and seeded with cells to mimic the environment of cells migrating through constrictions in vivo.

Chapter 3: Contraction of the Rear Cortex Supports Confined Migration Through a Pressure Induced Nuclear Transit Mechanism. I show that contraction of the rear cortex facilitates nuclear deformation and movement through constrictions during 3D migration. We find that multiple cell lines form a rounded, rear cortex

behind the nucleus during nuclear transit, and that this cortex enables more rapid movement through constrictions. Using fluorescently tagged actin and myosin, as well as a FRET-based biosensor for RhoA, we reveal that this contraction depends on actomyosin contractility in the rear cortex, which can be abolished through inhibition of ROCK. Using a laser ablation assay, we reveal that rear cortex contraction applies a pushing force behind the nucleus through increased intracellular pressure in the rear compartment of the cell. These findings represent a novel, previously unrecognized mechanism for facilitating nuclear transit through constrictions.

Chapter 4: Pressure in the Posterior Compartment of Migrating Cells Induces

Nuclear Influx. I show that nuclear blebbing is caused by the influx of cytoplasmic material into the nucleus, which depends on elevated compartmentalized pressure in the rear of the cell. Nuclear influx is measured using a photoactivatable cytoplasmic GFP which flows into the nucleus of cells migrating through microfluidic channels.

Upon laser ablation of actomyosin in the rear cortex of these cells, the rate of nuclear influx is significantly reduced. These findings show that cells migrating through channels increase compartmentalized intracellular pressure in the cell rear through contraction of the rear cortex, and that this pressure results in the formation of nuclear blebs.

Chapter 5: The Effect of Nuclear Size Defects on Nuclear Transit. Metastatic cancer cell lines frequently display changes in nuclear size which correlate with poor patient outcomes. Through a screening of chemical compounds which reverse these changes in nuclear size, we aimed to determine whether this was sufficient to reduce the ability of metastatic cancer cells to invade through constrictions. Our findings indicate that nuclear size rectifying compounds reduced migration in 2D wound healing assays and Boyden chamber assays, but not through microfluidic constrictions. It is unclear whether the observed migration defects induced by these compounds is directly related to their impact on nuclear size. These studies provide a proof of principle that some of these identified compounds may be valuable, cell-type-specific treatments to aid in the prevention of cancer metastasis.

Chapter 6: Enucleated Cells Invade More Rapidly Through Constrictions.

Engineered, enucleated mesenchymal stromal cells (MSCs) have been developed as a prospective tool for targeted delivery of therapeutics. Here we show that enucleated MSCs invade through microfluidic constrictions more rapidly than their nucleus-containing counterparts. These findings indicate that cells are able to migrate through 3D environments in the absence of a nucleus. Using a mouse model of inflammation, these enucleated cells are used to deliver therapeutics directly to the site of inflammation. Through enucleation and engineering of cells to express tissue-specific homing receptors, these cells provide significant advantages over previous targeted drug delivery systems and ameliorate many of the concerns which have limited their clinical translation, to date.

Chapter 7: Conclusions and Perspectives. Here I discuss the impact of the findings made during my graduate research. These works have contributed to an improved understanding of the relationship between the mechanics of the cell nucleus and intracellular force generation during confined migration. Through demonstration of a novel mechanism by which cells push their nucleus through constrictions, and work which showed a relationship between altering nuclear size and reduced migratory capacity, these works have opened up a variety of avenues of investigation which can lead to improvements to cancer therapies. My work in assessing the viability of enucleated cells as a drug-delivery vehicle may lead to great improvements for the efficacy of targeted drug therapies, and the reduction of off-target treatment effects.

CHAPTER 1 – INTRODUCTION

Cell Migration Overview

The migration of animal cells is an essential step in many physiological and pathological processes. During wound healing, embryogenesis, and immune surveillance, cells must migrate across great distances and through tissues in order to perform essential biological functions. Meanwhile, in diseases such as cancer, migratory cells lead to metastasis, which is the cause of 90% of cancer related deaths. Though migration is fundamental aspect of each of these biological phenomena, much is still unknown about the principal mechanisms which drive cell migration in vivo.

Though often studied through the lens of biochemical signaling pathways, cell migration is also a fundamentally mechanical process. Cell migration requires the transmission of mechanical forces between cells and their surrounding environments to propel the cell forward. Whether migrating on top of a 2D surface or navigating through a 3D matrix, cells must deform their cell membrane to change shape (Maeda et al., 2008), mediate tension throughout the cell body (Hetmanski et al., 2019; Houk et al., 2012), reposition intracellular cargo (Wu et al., 2014), and apply forces to their surroundings (Legant et al., 2010; Mulligan et al., 2019) in order to achieve forward movement. These mechanical factors are especially important in 3D migration, as 3D environments present physical barriers which cells must squeeze through (Doyle et al., 2013). Cells migrating through biological tissues must interact with and navigate

through physical obstacles, such as extracellular matrix fibers and endothelial cell layers, whereas cells migrating along 2D surfaces face no such barriers. As a result of these complex environmental factors, cells migrating in 3D must utilize unique biophysical mechanisms to overcome their confining surroundings. These mechanisms include proteasomal degradation of the surrounding matrix, realignment of the surrounding matrix through adhesive traction forces, and substantial deformation of the cell body to squeeze in between extracellular confinements (Provenzano et al., 2008; Wolf et al., 2013).

While cells can radically change their shape to fit through highly constrictive environments, the nucleus, which is 2 to 10 times stiffer than the surrounding cell membrane and cytoplasm, limits the cell's ability to pass through extracellular confinements (Davidson et al., 2014; Wolf et al., 2013). Unlike in 2D migration, where the nucleus may be pulled along as passive cargo in the cell, cells must use distinct mechanisms to translocate their nucleus through 3D constrictions (Graham et al., 2018; Khatau et al., 2012). Recent studies have revealed a variety of mechanisms by which cells apply force to translocate their nucleus during 3D migration (Marks & Petrie, 2022; McGregor et al., 2016). However, it is still not yet precisely clear how cells “choose” between these various mechanisms, or how specific these mechanisms are to particular cell types, or environmental factors.

Consequences of Nuclear Deformation in Confined Migration

As the nucleus passes through constrictions, it undergoes substantial physical deformation which results in strain on both the nuclear envelope and the DNA contained within it (Davidson et al., 2015). If this strain is sufficiently great, it may result in DNA damage and nuclear rupture (Denais et al., 2016; Irianto et al., 2016; Raab & Discher, 2017; Shah et al., 2021). These consequences may be dangerous in the case of cancer metastasis, as further instability to the genome of metastasizing cells may lead to further malignant transformation (Nader et al., 2021), potentially resulting in evasion of chemotherapies.

Nuclear deformation can also result in changes in chromatin organization which may impact the migratory behavior of cells (Damodaran et al., 2018; Golloshi et al., 2022; Hsia et al., 2022). Growing evidence suggests that nuclear deformation leads to decondensation of chromatin, which reduces nuclear stiffness, thus enabling migration through constrictions (Fischer et al., 2020; Wang et al., 2018). Such dynamic changes to nuclear architecture indicates that the nucleus acts a mechanosensor during confined migration. Indeed, such sensitivity has been demonstrated in microfluidic migration studies which show that the nucleus can sense confinement, as nuclear envelope strain releases intracellular calcium and triggers enzymes which can lead to increased cellular contractility (Lomakin et al., 2020; Renkawitz et al., 2019).

In this thesis, I will investigate the role of intracellular forces on mediating nuclear transit through confined environments. I aim to determine how cytoskeletal forces are transmitted to the nucleus, and what biological signaling factors enable these forces.

As there are multiple suspected mechanisms which drive nuclear transit, I will investigate what factors lead cells to use one mechanism over another.

Actomyosin Forces During Migration

In order to migrate, cells must generate forces which are transmitted to their surroundings and result in forward movement. Historical studies on the migration of animal cells predominantly relied on observations of cells cultured on 2D substrates (Stossel, 1993). These early works revealed a cyclical process by which cells receive a biochemical signal to initiate directional migration which leads to protrusion formation at the leading edge, adhesion of these protrusions to the underlying substrate, contraction of actin filaments, and trailing edge detachment, which results in forward movement of the cell (Ridley et al., 2003). Contraction of cytoskeletal actin filaments is central to the generation of intracellular forces which enable migration. This contraction is regulated through the Rho-ROCK-myosin II signaling pathway. In brief, when the Rho family guanosine triphosphate (GTP)-binding protein (RhoGTPase) RhoA is converted into its active GTP-bound state, it binds to Rho-associated protein kinase (ROCK). Upon this binding, ROCK phosphorylates myosin light chain (MLC) which causes crosslinking of actin filaments through interactions with myosin II, leading to the formation and contraction of bundles of actomyosin fibers. These actomyosin fibers form connections to extracellular proteins through focal adhesions to transmit intracellular forces to the surrounding environment, thus leading to forward cellular movement.

To complicate this model, it has become apparent that the importance of each step in this canonical migration process varies depending on both the environmental context and cell type (Balzer et al., 2012; Geiger et al., 2019; Liu et al., 2015). In 3D environments, cells can “choose” between a set of at least 3 distinct migration modes: mesenchymal, amoeboid, and lobopodial (Yamada & Sixt, 2019). Mesenchymal migration is most similar to 2D migration, where cells exhibit a polarized, elongated morphology, and require adhesions to migrate. Lobopodial migration occurs when actomyosin and intermediate filaments pull the nucleus forward to generate pressure-driven protrusions at the leading edge of the cell, which enables invasion through confined environments (Petrie et al., 2014). Amoeboid cells are able to migrate without forming focal adhesions (Balzer et al., 2012). Instead of transmitting actomyosin forces through adhesions, cells are instead able to migrate through retrograde flow of actomyosin in the cell cortex, which couples to surrounding matrix through normal forces at the cell periphery generated by increased intracellular pressure (Bergert et al., 2015; Liu et al., 2015; Yip et al., 2015). Though cells can switch between these migration modes under varying biological contexts, actomyosin forces are required in all of these migration modes (Sahai & Marshall, 2003; Yamada & Sixt, 2019). Due to this conservation across migration mechanisms, the Rho-ROCK-myosin II pathway represents a promising avenue for preventing cancer metastasis, which requires disseminating cancer cells to undergo confined migration to form tumors in distal sites in the body (te Boekhorst & Friedl, 2016; Vennin et al., 2020).

Prior works have largely focused on the transmission of these internal actomyosin forces to the external environment, rather than how those internal forces facilitate nuclear movement during confined migration. As the nucleus limits the rate of confined migration (Davidson et al., 2014), it will be important to improve the understanding of how actomyosin forces (and other intracellular forces) mediate nuclear movement through constrictions.

Intracellular Forces on the Nucleus

While migrating through biological tissues, cells must significantly deform the nucleus in order to pass through narrow interstitial spaces in between extracellular matrix fibers and endothelial cell layers (Weigelin et al., 2012). Cells must apply considerable intracellular force to deform and move the nucleus through constrictions (Weigelin et al., 2012). It is understood that nuclear movement is regulated through a combination of actomyosin, intermediate filament, and microtubule forces, each of which may (or may not) depend on, (1) adhesions to the surrounding environment, (2) connections to the nucleus through the LINC complex, and (3) cellular contractility. However, it is not clear whether these cytoskeletal forces primarily “push” or “pull” the nucleus through constrictions, though evidence of each of these modes have been recently reported. The relative importance of these “pushing” and “pulling” forces for mediating nuclear transit, and what environmental and biological factors dictate the selection of each of these mechanisms is not fully understood (Marks & Petrie, 2022). A brief summary of the suspected roles of various factors in influencing nuclear transit mechanisms in various migration modes is illustrated below (**Figure 1.1**). Here, I will

summarize the current understanding in the literature on how “pulling” and “pushing” forces have been shown to play a role in nuclear transit.

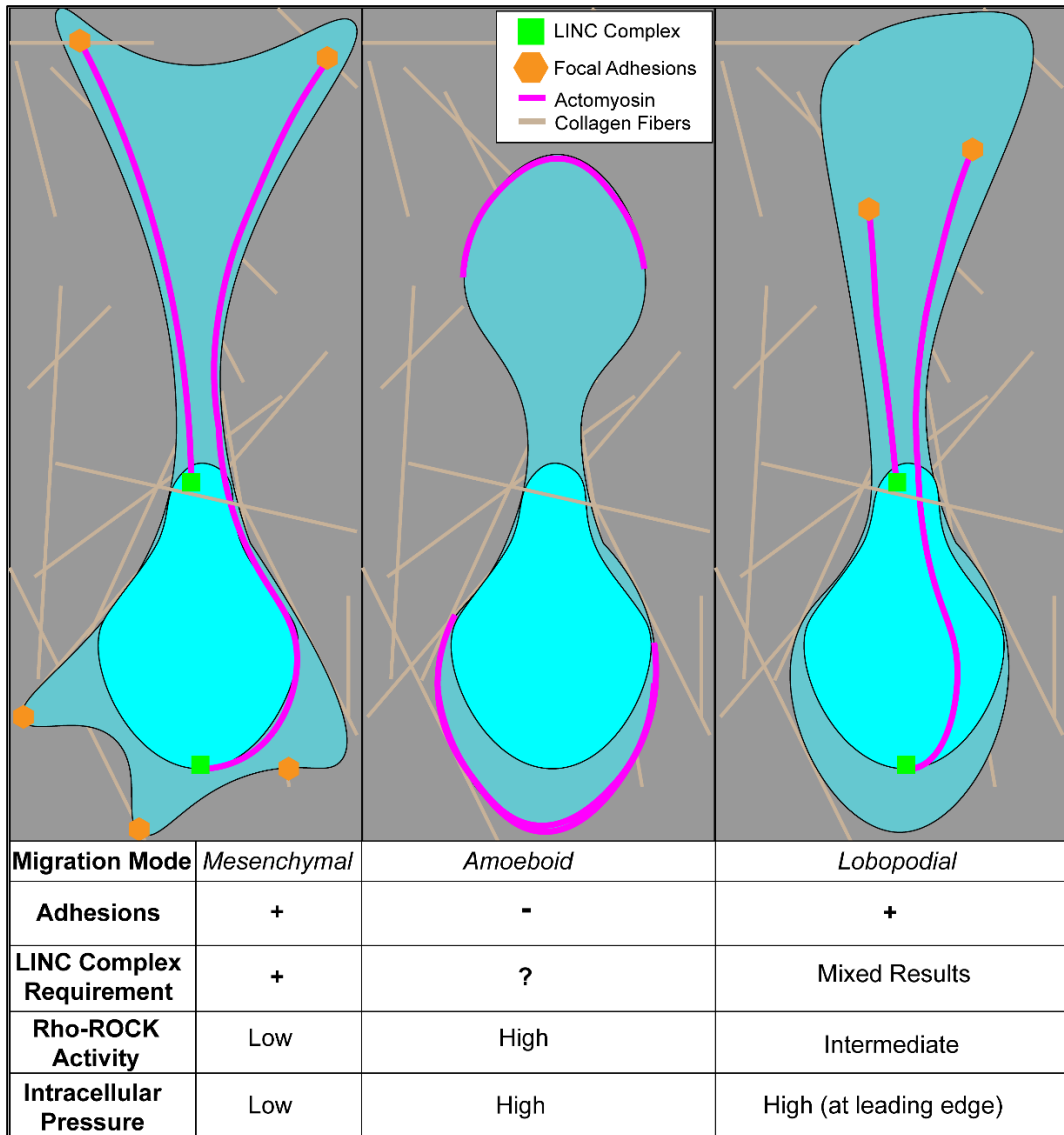


Figure 1.1: Intracellular force transmission to the nucleus varies depending on biological and environmental contexts. (left) Mesenchymal migration occurs in highly adhesive environments in cells with low Rho-ROCK contractility. Nuclear translocation in these cells depends on pulling forces at the leading edge of the nucleus (Davidson et al., 2020). (middle) Amoeboid migration occurs in conditions of high confinement and low adhesion, in cells with high Rho-ROCK contractility (Liu et al., 2015; Ruprecht et al., 2015). These cells show considerable accumulation of actomyosin throughout the cell cortex, and especially in the posterior “uropod”, which is associated with high cortical tension and increased intracellular

pressure (Bergert et al., 2015; Charras & Paluch, 2008). It is unknown how exactly forces are transmitted to the nucleus during amoeboid migration. (right) Lobopodial migration requires adhesions to the environment in order to increase pressure at the leading edge of the cell to form pressure-driven protrusions (Petrie et al., 2014). This mode of migration requires Rho-ROCK driven actomyosin contractility, but results are mixed on whether or not LINC complex connections are required for confined migration in this mode (Lee et al., 2021; Petrie et al., 2014; Thiam et al., 2016).

Pulling Forces on the Nucleus

Connections between the nucleus and cytoskeleton are formed through the Linker of Nucleoskeleton and Cytoskeleton (LINC) Complex. The LINC complex includes a diverse array of Nesprin and Sun proteins which, in combination, facilitate connections between the nuclear envelope and cytoskeletal fibers. When cytoskeletal fibers contract, forces can be transmitted directly from the environment to the nucleus through the LINC complex, in order to pull the nucleus forward (Alam et al., 2015; Arsenovic et al., 2016). These pulling forces at the leading edge of the nucleus can be generated through LINC complex interactions with both actomyosin (Davidson et al., 2020; Khatau et al., 2012; Lombardi et al., 2011; Petrie et al., 2014; Wu et al., 2014) and intermediate filaments (Petrie et al., 2014, 2016) during 2D and 3D migration. Rotational forces acting through the LINC complex can be generated through the microtubule motors kinesin and dynein (J. R. Levy & Holzbaur, 2008; Tsai et al., 2010; Wu et al., 2011; Zhu et al., 2017) though microtubule forces appear to be dispensable for nuclear movement (Norden et al., 2009; Yanakieva et al., 2019).

Though many studies have shown that LINC-complex-dependent pulling forces are important during 3D migration, many cells can move the nucleus through constrictions in the absence of the LINC complex (Ketema et al., 2013; Lee et al., 2021; Lv et al., 2015; Mistriotis et al., 2019; Sharma et al., 2021; Thiam et al., 2016). Whether these forces are mediated through alternate means of direct cytoskeletal interactions with the nucleus, such as through perinuclear actin polymerization (Thiam et al., 2016), or through indirect force transmission remains unclear. One such indirect mode of force transmission between the cytoskeleton and the nucleus is through pushing forces mediated between the contracting rear cortex of the cell and the nucleus.

Pushing Forces on the Nucleus

In contrast to mechanisms involving pulling forces in front of the nucleus, the role of pushing forces in nuclear translocation is less-well examined. Various studies have noted accumulation of actomyosin in the rear of cells migrating in 3D (Lee et al., 2021; Liu et al., 2015; Lorentzen et al., 2011; Martini & Valdeolmillos, 2010; Mistriotis et al., 2019; Poincloux et al., 2011; Ruprecht et al., 2015). This accumulation of actomyosin at the rear of migrating cells has been referred to as the “uropod” in migrating immune cells, and plays a key role in 3D amoeboid migration (Liu et al., 2015). Uropod recruitment of myosin corresponds with increased bleb formation at the sides of cells and at the leading edge which contribute to cell movement and suggest an increase in intracellular pressure (Chi et al., 2014). It has also been noted that uropod formation, and a switch to an amoeboid migration mode

tends to occur under conditions of high cellular contractility in highly confined environments (Liu et al., 2015; Ruprecht et al., 2015). It is still an open question as to how uropod formation, and rear accumulation of myosin contributes to nuclear translocation.

An early study from Lämmermann et al (2008) found that myosin light chain preferentially localized to the rear of dendritic cells migrating through 3D collagen matrix (Lämmermann et al., 2008). Noting that retraction of the cell rear was dependent on myosin activity, they found that blebbistatin delayed rear cortex contraction and also prevented nuclear transit through constrictions (Lämmermann et al., 2008). The authors suggested that this indicated that this demonstrated myosin-dependent pushing forces at the rear of the nucleus which facilitated nuclear transit. Despite these observations, there was still little suggestion of how exactly these actomyosin forces are transmitted to the nucleus, in order to push the nucleus forward. Later works indicated that contraction of the cell rear can drive invasion through a 3D matrix, and depends on ROCK-mediated contractility and recruitment of actomyosin to the cell rear (Lorentzen et al., 2011; Poincloux et al., 2011).

To date, the evidence of pushing forces behind the nucleus which enable nuclear transit are largely descriptive, while a mechanism which demonstrates how these forces are transmitted to the nucleus is still absent. The existing literature proposes both that cells frequently accumulate actomyosin in the rear cortex of the cell, that this accumulation is dependent on Rho-ROCK activity, and that this mechanism may be

connected to amoeboid modes of migration. To closely examine how contraction of the rear cortex contributes to nuclear translocation, it will be necessary to apply a combination of tools which measure force transmission between the rear cortex and the nucleus, and reveal the dynamics of contractile proteins in the rear cortex during nuclear transit.

Methods for Studying Intracellular Forces

Microfluidic devices have been used to recapitulate key features of the *in vivo* migration environment, while supporting higher resolution imaging of cells migrating in 3D (Chaw et al., 2006; Davidson et al., 2015; Huang et al., 2015; Keys et al., 2018). The use of microfluidic devices to mimic the confined environment of migrating cells has enabled considerable insights into the unique factors which drive 3D migration. The development of microfluidic devices for cell migration studies typically involves the etching or imprinting of precisely defined features into a substrate (often PDMS, or another soft polymer) which is then bound to an alternate surface (often a glass coverslip). These features are then filled with fluid, such as a cell media, and are then seeded with cells, which then migrate along the constructed features. The advantage of this approach is the high control that the scientist has over what features can be etched into these devices based on what scientific question is to be answered. Microfluidic devices have been used to study of effect of interstitial flows on migration (Huang et al., 2015), the effect of channel size on migration rate (Jacobelli et al., 2010; Tong et al., 2012), migration through individual constrictions (Davidson et al., 2014;

Lautscham et al., 2015), and transendothelial migration (Han et al., 2012), just to name a few.

Microfluidic devices can supplement other more conventional approaches to studying 3D migration, which include transwell migration assays or 3D collagen matrix migration assays (Chen, 2005; Friedl et al., 1993). In contrast to transwell assays, which allow evaluation of large cell populations after confined migration, microfluidic devices enable the direct observation of confined migration events as they occur. This can help to reveal cell-to-cell variations in migratory behavior, as well as intracellular dynamics which enable migration through confined environments. While migration through 3D collagen matrices may more closely mimic the heterogeneous *in vivo* migration environment, microfluidic devices enable greater control over the biophysical parameters which dictate cellular behaviors during migration. The ability to both precisely control constriction geometries and spatiotemporally resolve intracellular dynamics are especially important during the study of nuclear transit. To reveal how forces are transmitted to the nucleus during confined migration, it will be necessary to observe how proteins localize around the nucleus throughout the nuclear transit process and determine how spatial constraints lead to the use of particular nuclear transit mechanisms.

Like all *in vitro* assays of cell migration, microfluidic devices have unique limitations which must be considered in the interpretation of experimental results. In contrast to biological tissues, microfluidic devices are typically made from PDMS and glass.

These materials are typically much stiffer than most tissues, and consequently may induce different migratory behavior (Geiger et al., 2019). Many cells migrating through tissues can degrade the surrounding matrix using matrix metalloproteinases, which facilitates passage through constrictions (Infante et al., 2018; Wolf et al., 2003). This mechanism is not possible when migrating through constrictions made of PDMS (and other polymers commonly used in microfluidic devices, such as Polyacrylamide) which is non-degradable. These limitations and others suggest that microfluidic devices may be useful for demonstrating biological phenomena, but results from microfluidic devices should typically be complemented by studies in more biologically relevant assays, such as collagen matrices or *in vivo*.

Conclusions

In comparing existing literature supporting either the “pushing” or “pulling” nuclear transit hypotheses, it is clear that the mechanism behind “pushing” forces is considerably less well established. It is known that pulling forces on the nucleus during 3D migration are mediated via connections between the nucleus and cytoskeleton (Déjardin et al., 2020; Petrie et al., 2016). However, while various groups have reported localization of actin and myosin to the rear of migrating cells, and that this localization is dependent on ROCK (Chi et al., 2014; Hetmanski et al., 2019; Mistriotis et al., 2019), none of these studies have produced direct measurements of forces mediated between the rear cortex and the nucleus. In this work, I will investigate how cells apply pushing forces behind the nucleus during confined migration, and examine the impact of these pushing forces on nuclear movement.

CHAPTER 2- ASSEMBLY AND USE OF A MICROFLUIDIC DEVICE FOR THE STUDY OF CONFINED MIGRATION¹

Abstract

Cells migrating in tissues must often pass through physical barriers in their surroundings in the form of fibrous extracellular matrix or other cells. To improve our understanding of how cells move in such confined microenvironments, we have designed a microfluidic device in which cells migrate through a series of three-dimensional polydimethylsiloxane (PDMS) constrictions with precisely controlled geometries that mimic physiological pore sizes. The migration device offers an experimental platform that combines a well-defined three-dimensional (3D) environment with a set-up well suited for imaging confined cell migration at high spatial and temporal resolution. In this protocol, we describe the fabrication and use of these devices using standard soft lithography techniques and light microscopy. Analysis of live-cell time-lapse series of cells with fluorescently labeled nuclear and/or cytoskeletal structures migrating in the devices can reveal new insights into the molecular processes required for confined migration, including the role of the linker of nucleoskeleton and cytoskeleton (LINC) complex, which has been implicated in 3D migration.

¹ This section is adapted from the following publication:
Keys JT, Windsor A, Lammerding J (2018) Assembly and Use of a Microfluidic Device to Study Cell Migration in Confined Environments. *Methods in Molecular Biology*
Contributions: JT Keys wrote the text of this chapter and produced all included figures. A Windsor provided essential insights and editing on sections regarding photolithography.

Introduction

Cell migration represents a crucial step in a variety of biological processes, including cancer metastasis, inflammation, and wound healing. In the *in vivo* tissue environment, interstitial spaces, extracellular matrix networks, and other cells constitute a confined environment for migrating cells. Dense fibrous tissue matrix and layers of endothelial cells form narrow constrictions, which measure 0.1-30 μm in diameter (Doerschuk et al., 1993; Weigel et al., 2012). To move through such tight spaces, cells must produce significant intracellular forces to compress their nucleus, as it is typically the largest and stiffest organelle (Caille et al., 2002; Davidson & Lammerding, 2014; McGregor et al., 2016). Prior work has suggested that the linker of nucleus and cytoskeleton (LINC) complex facilitates the transmission of forces from contractile actomyosin fibers to the nucleus during confined migration (Bone et al., 2016; Jayo et al., 2016; Khatau et al., 2012; Petrie et al., 2014; D. G. Thomas et al., 2015). Consequently, depletion of LINC complex proteins such as Nesprin-2 and Nesprin-3 reduces migration speed through confining environments, and impairs the cell's ability to deform its nucleus (Jayo et al., 2016; Khatau et al., 2012; Petrie et al., 2014; D. G. Thomas et al., 2015). Since the dimensionality of the cell environment modulates migratory behavior, the study of cell migration *in vitro* requires model systems that faithfully reproduce the 3D confinements of biological tissue (Fig. 2.1A-B)(Doyle et al., 2013). Additionally, to elucidate the dynamic nuclear and cytoskeletal processes that mediate nuclear translocation in confined spaces, these model systems must also enable the detailed observation of cells by time-lapse microscopy by confocal or wide field microscopy.

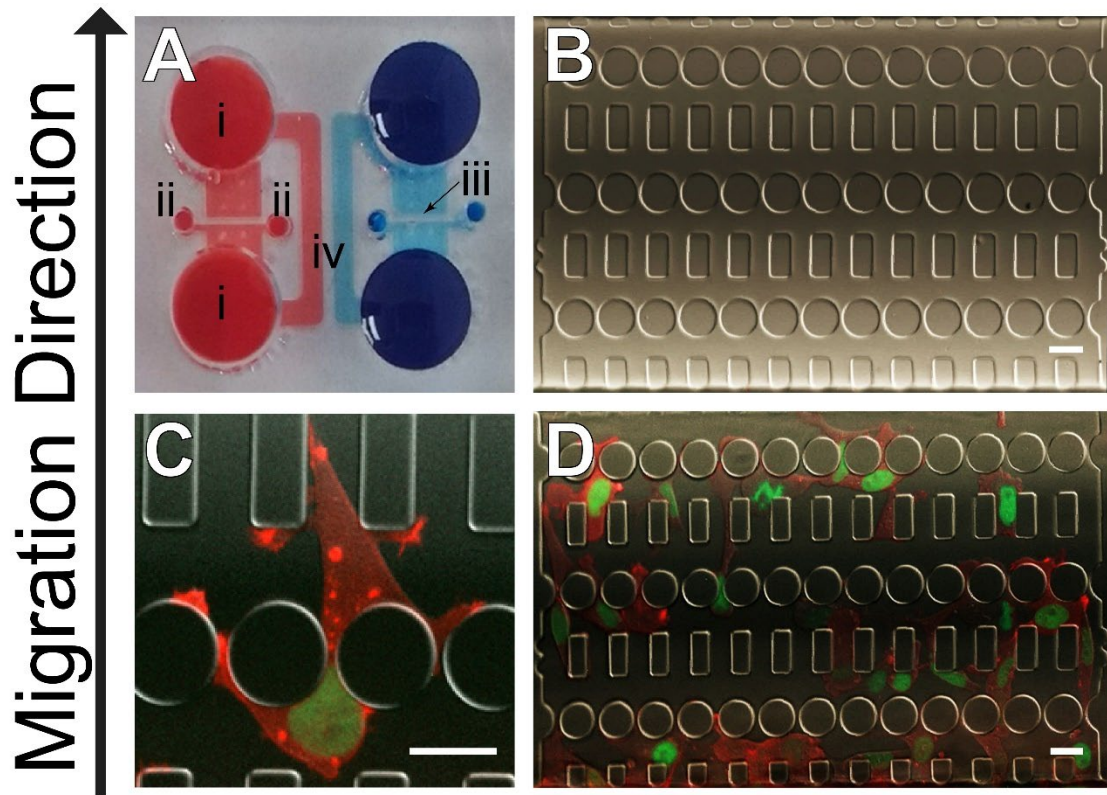


Figure 2.1. Overview of the migration device. **(A)** Top-down view of migration device, with food coloring added to enhance details. Cell culture media is added into the media reservoirs (i). Cells are seeded into the devices through seeding ports (ii) that lead to the 5 μm tall area with the constrictions (iii). Larger bypass channels (iv) allow rapid equilibration of media reservoir levels to prevent flow through constrictions, facilitating formation of a chemotactic gradient by diffusion if serum or growth factors are added to one of the reservoirs. **(B)** Image of the 5 μm tall area of the device with 2 μm wide constrictions without cells present. Scale bar 25 μm . **(C, D)**. Images of constriction area containing MDA-MB-231 breast cancer cells expressing an mCherry-actin chromobody and an mNeonGreen-H2B histone label. Panel **(C)** depicts a cell as it starts to pass through a constriction. Scale bar 25 μm .

Many tools have been developed for the study of confined migration in vitro (Kramer et al., 2013; Lautenschlager & Piel, 2012). One popular group of devices are transwell

invasion assays, such as the Boyden chamber. However, these systems are limited by a limited ability to directly observe cells during migration, as cells in these chambers migrate perpendicular to the imaging plane. Another approach for studying confined migration are extracellular matrix scaffolds (e.g., collagen or Matrigel). These scaffolds are generated through random self-assembly of matrix fibers, which produces an environment that closely mimics biological tissue, but provides only limited control over the size of individual pores. In recent years, microfluidic devices have been developed using soft lithography techniques to reproduce the physical confinements of the *in vivo* tissue environment (Davidson et al., 2015; Lautenschlager & Piel, 2012; Tong et al., 2012). These devices feature channels of defined geometries through which the cells must migrate, either spontaneously or following a chemotactic gradient. These microfluidic platforms are quite versatile as they provide the user with flexibility in the design and layout of constrictions.

In this protocol, we describe the design and use of a polydimethylsiloxane (PDMS) microfluidic device with a series of tight constrictions located between two larger chambers (Fig. 2.2B, C) (Davidson et al., 2015). Cells are seeded in one of the chambers and then migrate through a section 5 μm in height containing constrictions between 1 and 2 μm in width, formed by 30 μm wide circular pillars (Figs. 2.1C and 2.2). Additionally, there is a set of 15 μm wide constrictions, which cells can migrate through without deforming their nucleus, and which serve as an important control to assess effects independent of nuclear confinement. Unlike other microfluidic devices, in which cells often move through long, continuously confining channels, the

confinement in the device described here is limited to a very short segment, i.e., cells move through a single, tight constriction, enter a less confined region, and then encounter the next constriction. This design seeks to reproduce the varied, discontinuous sequence of pores and confinement which cells are subjected to during in vivo migration, such as matrix fibers, or endothelial cell layers (Weigelin et al., 2012; Wolf et al., 2013). These devices have already aided in our initial studies of dynamic processes that occur during confined migration, such as the rupture of the cell nucleus and the essential role of perinuclear myosin IIB in moving the nucleus through narrow constrictions (Denais et al., 2016; D. G. Thomas et al., 2015).

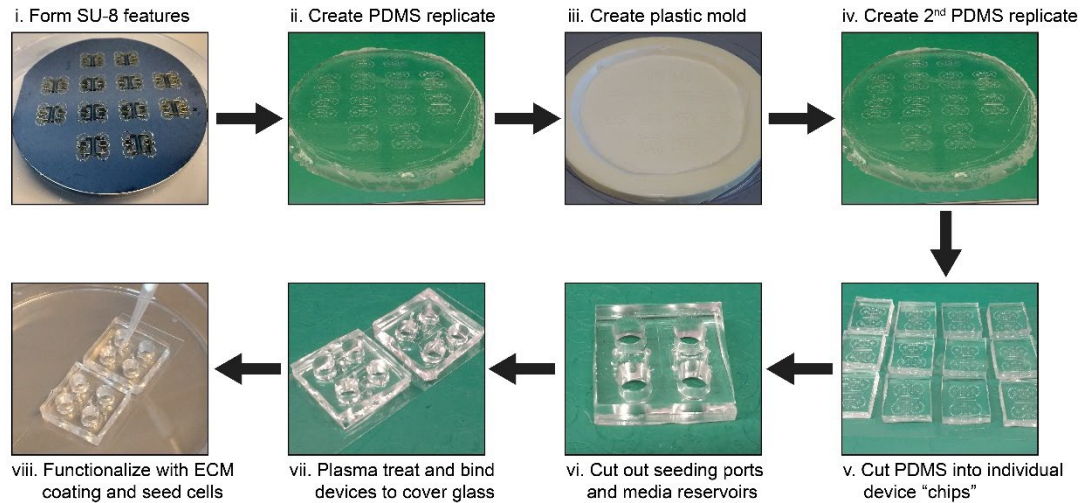


Figure 2.2. Overview of migration device fabrication. *i)* SU-8 microfluidic features are developed onto a silicon wafer through photolithography. *ii)* A PDMS replicate of these features is formed using a 2-part elastomer curing-base mixture. *iii)* Optionally (but recommended), a secondary plastic mold can be cast from the initial PDMS replicate, which will be used to form additional PDMS devices. *iv)* Using a similar process to step *ii*, a PDMS replicate is formed from the secondary plastic mold. *v)* The PDMS replicate is cut into 12 device "chips." Each "chip" contains 2 independent microfluidic devices, each with the features shown in Figure 2.1. *vi)* Media reservoirs (labeled *i* in Figure 2.1A) and seeding ports (labeled *ii* in Figure 2.1A) are cut out using biopsy punches. *vii)* Devices are cleaned with IPA and DI water, treated using a plasma cleaner, and then covalently bound to glass slides. *viii)* Devices are functionalized with extracellular matrix proteins prior to adding cells through the seeding ports (labeled *ii* in Figure 2.1A) and filling reservoirs with cell media. At this point, devices may be incubated until ready for analysis using live cell imaging or immunofluorescence.

To produce these devices, SU-8 microfluidic features are formed onto a silicon wafer through photolithography. Next, a PDMS replica is cast from the SU-8 features, the

PDMS is cut into individual devices, bound to a glass slide, functionalized with extracellular matrix (ECM) solution, and seeded with cells. Following a period of incubation to allow cells to enter the constrictions, analysis of cell migration can be performed by live-cell imaging or standard immunofluorescence techniques. This protocol will outline the procedures necessary for both producing these devices and using them for the study of confined migration (Fig. 2.3). The protocol assumes basic familiarity with SU8 and PDMS soft lithography. For users new to soft lithography, we recommend Qin et al (2010) as a good starting point(Qin et al., 2010).

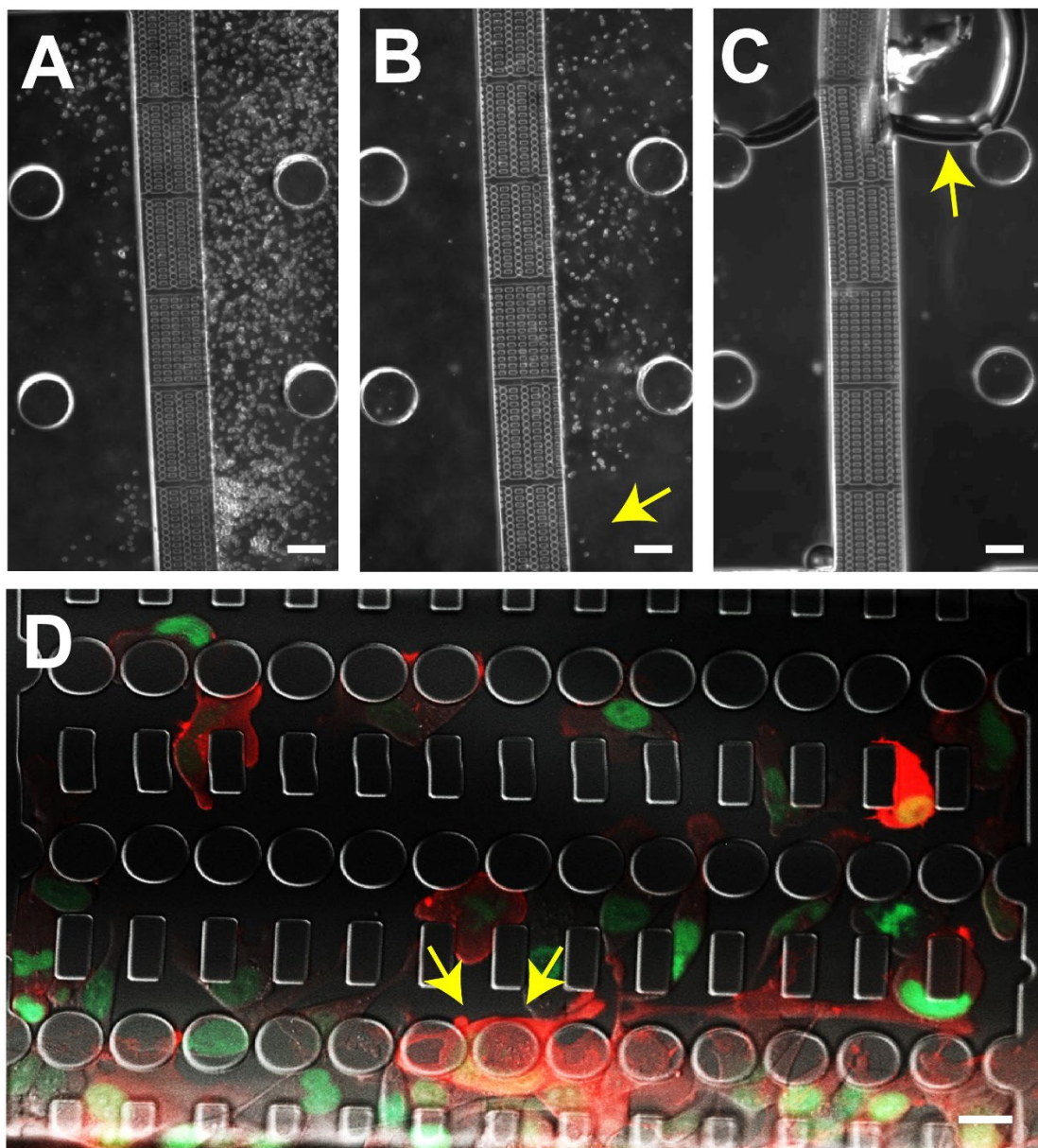


Figure 2.3. Recognizing potential issues with device loading and bonding. **(A)** Properly loaded cells with even distribution across the device. Scale bar 200 μm . **(B)** Uneven loading of cells in front of constrictions; bottom constrictions section has no cells at entrance (arrow). Scale bar 200 μm . **(C)** Air bubbles in cell media formed within the device, blocking entry into the constriction channels. Scale bar 200 μm . **(D)** Cells migrating underneath constriction pillars (arrows), indicating insufficient bonding of PDMS pillars to glass. Scale bar 25 μm .

Materials

2.1 Photolithography

1. CZ silicon wafer, 4 inch diameter, type N, 525 μm thick, <1-0-0> orientation (Silicon Quest International)
2. Chrome photomask on a quartz substrate, 5" \times 5" \times 0.090" (Telic, Valencia, CA)
3. Heidelberg DWL 2000 mask writer (Heidelberg Instruments, Heidelberg, Germany)
4. Long-pass filter for near UV light (PL-360LP from Omega Optical, or equivalent.)
5. AutoCAD software (Autodesk, Mill Valley, CA) or equivalent
6. Mask aligner system (ABM, San Jose, CA)
7. Molecular vapor deposition system (SPTS Technologies, Newport, RI)
8. Kapton polyimide film (Dupont, Wilmington, DE)
9. Oven suitable for temperatures up to 150°C
10. CEE Model 100 spin coater, or equivalent (Brewer Sciences, Rolla, MO)
11. SU-8 2005 photoresist (MicroChem, Newton, MA)
12. SU-8 100 photoresist (MicroChem, Newton, MA)
13. SU-8 developer (MicroChem, Newton, MA)
14. Semiconductor grade acetone
15. Cleanroom swab (Texwipe TX761 Alpha Swab with long handle, or equivalent)
16. CMOS grade isopropyl alcohol (IPA)

17. Deionized (DI) water
18. >95% (1*H*,1*H*,2*H*,2*H*-perfluorooctyl)trichlorosilane (FOTS) (Gelest Inc, Morrisville, PA)

2.2 Casting of migration devices in PDMS

1. 150 mm Petri dish
2. Sylgard 184 silicone elastomer base and curing agent (Dow Corning, Midland, MI)
3. Stirring rod for mixing elastomer base and curing components
4. Vacuum pump (Oerlikon Trivac D2.5E)
5. Vacuum desiccator (Catalog #Fisher 08-594-16C)
6. Oven suitable for temperatures of 65°C (e.g., VWR Gravity Convection Oven, Catalog #414005-108, or equivalent)

2.3 Mounting and seeding of devices

1. Biopsy punches (1.2 mm and 5mm)
2. 24 mm x 60 mm Number 1.5 Micro Cover Glass (VWR, Radnor, PA, Catalog # 48393-251) stored overnight in 0.2 M hydrochloric acid
3. Isopropyl alcohol (IPA)
4. DI water
5. 70% ethanol
6. Oxygen plasma cleaner (Harrick Plasma, Catalog# PDC-001)
7. Type I collagen (50 µg/mL in 0.02M glacial acetic acid) or fibronectin (5

µg/mL in PBS) solution

8. Dulbecco's Phosphate Buffered Saline (DPBS), no calcium, no magnesium (Thermo Fisher, Waltham, MA, Catalog# 14200-075, or equivalent)
9. Cells of interest (see Note 1)
10. Cell culture media appropriate for cells of interest
11. Pipettes and tips for loading devices (20 µL and 200 µL pipettes work well)

2.4 Microscopy and Analysis

1. Inverted fluorescence microscope. Microscope should have objective with 20× magnification and fluorescence excitation/emission filters for GFP and/or other fluorophores of interest.
 2. Stage-top incubation chamber for microscope to maintain temperature at 37 °C. Humidity control is optional, as microfluidic devices can be sealed.
 3. Microscope-mounted CCD or CMOS camera for image acquisition
 4. Image acquisition software, such as ZEN BLUE (Zeiss), Micromanager, or others
- ImageJ, FIJI, MATLAB, or other software for image analysis

Methods

3.1 Photolithography

All photolithography steps should be performed in a dedicated clean room facility under standard clean-room conditions, with protective equipment and sufficient ventilation underneath a fume hood. The development of SU-8 microfluidic features onto a silicon wafer is described below.

1. Generate a design for the mask using CAD software and the downloaded CAD files. The device design and geometry is described in detail in Davidson et al. (2015) (Davidson et al., 2015). The CAD files for the device can be downloaded at <http://lammerding.wicmb.cornell.edu/>.
2. Using a Heidelberg DWL 2000 Mask Writer, develop the chrome photomask based on the CAD design layout. This photomask will be used to expose the design features in SU-8 photoresist onto the silicon wafer using near ultraviolet (UV) light.
3. Clean silicon wafer using standard metal oxide semiconductor (MOS) cleaning procedures (see Note 2) and bake overnight at 90° C to dehydrate.
4. Coat wafer with ~2 mL of SU-8 2005 (MicroChem) and spin down using a spin coater (CEE Model 100 spin coater, or equivalent) at 3000 RPM for 30 seconds (see Note 3) to obtain a 5 μm thick layer, which will be used for the design of the first layer with the 5 μm tall features.
5. Allow the SU-8 to relax for 10 minutes at room temperature (RT). Then remove 5 mm of excess SU-8 from the edge of the wafer perimeter using a cleanroom swab soaked in acetone.
6. Bake the wafer on a hot plate from RT to 65 °C at a rate of 2.0°C per minute, hold at 65°C for 10 minutes, then remove from plate and allow to cool back to RT (see Note 4).
7. Expose the wafer to near UV light at 365nm using an ABM contact aligner with a long pass filter for 40 seconds (see Note 5).
8. An hour after exposure, bake the wafer on a hot plate from RT to 95°C at a

rate of 2.0°C per minute, hold at 95°C for 1 minute, and then leave to cool back to RT.

9. Place wafer in SU-8 developer overnight to remove unexposed SU-8.
10. Rinse wafer with fresh SU-8 developer, then rinse with isopropyl alcohol and deionized water two times each to clean.
11. Bake wafer in an oven from RT to 150°C for 20 minutes. Then shut off oven, and allow wafer to cool to RT. This step is a “hard bake” step, which solidifies the first SU-8 layer, and prevents unwanted merging with the second layer.
12. Dehydrate wafer overnight by baking at 90°C.
13. Cover the alignment marks on the wafer for the 5 μ m layer using Kapton tape (see Note 6).
14. For a thickness of 200 μ m, coat wafer with \sim 2 mL SU-8 100 and spin at 1500 RPM for 60 seconds (see Note 7).
15. Allow the SU-8 to relax for 10 minutes and then remove 5mm of excess SU-8 from the edge of the wafer perimeter using a cleanroom swab soaked in acetone.
16. Bake the wafer on a hot plate with a lid (any cover is sufficient; we use a Pyrex petri dish cover) from RT to 55°C at a rate of 2.0°C per minute for 14 hours, then increase to 60°C at a rate of 2.0°C per minute for 14 hours, then leave to cool back to RT.
17. Score the edges of the Kapton tape with a razor and gently remove from the wafer.
18. Expose the wafer on the contact aligner with a long pass filter for one minute,

six times with one minute of rest in-between (see Note 8).

19. Twenty minutes after exposure, bake the wafer on a hot plate with a lid.
Increase the temperature from RT to 95°C at a rate of 1.5°C per minute, hold at 95°C for 1 minute, and then leave to cool back to RT.
20. Leave wafers in SU-8 developer overnight.
21. Rinse wafer with fresh SU-8 developer, followed by a wash with isopropyl alcohol and deionized water, two times each.
22. Bake wafers from RT to 60°C for two hours in an oven on an aluminum plate to remove moisture and leave to cool in the oven to RT.
23. Coat wafers with FOTS using a Molecular Vapor Deposition (MVD) tool.
24. Wafers can now be removed from the clean room and used for casting into PDMS (Fig. 2.2ii, iv).

3.2 Casting of migration devices in PDMS

From this point on, all components should be handled with nitrile gloves to minimize risk of contamination of devices. All steps may be performed on a lab bench, until devices are assembled, sprayed with ethanol, and moved into a cell culture hood.

1. Place the silicon wafer with SU-8 features facing upward into a 150 mm petri dish (or use secondary plastic mold, see Note 9).
2. Add PDMS base and curing agents into a standard plastic cup at a 10:1 ratio (typically 50 grams of base and 5 grams of curing agent is sufficient for a set of 12 device chips) and stir vigorously for 5 minutes to fully combine. The

stirring of these components will cause many air bubbles to form in the mixture, and these must be removed through degassing prior to curing of the PDMS.

3. Place PDMS mixture into a vacuum desiccator at 30 psi for 20 minutes to eliminate bubbles and accelerate degassing of the polymer.
4. Pour PDMS mixture over wafer (or secondary device mold), and allow 5 to 10 minutes to set at room temperature.
5. Using a very light stream of pressurized air, blow directly over the surface of the PDMS in order to eliminate all remaining bubbles. After this step, PDMS should be completely clear.
6. Preheat an oven to 65°C, and then bake PDMS mixture in oven for at least 2 hours (see Note 10).
7. Remove mold from oven and allow PDMS to cool to room temperature (see Note 11).
8. Using a razor, cut around edges of PDMS mold, ensuring that there is sufficient space in between the cut-edge and device features.
9. Carefully peel PDMS out of the mold, ensuring that PDMS does not tear during removal. The molded PDMS will contain 12 device “chips,” each of which contains 2 migration devices (Fig. 2.1A).
10. Using a razor, cut PDMS into 12 device chip segments (Fig. 2.2v).
11. Place PDMS devices onto clean packing tape, feature-side down, to protect devices from dust during storage.
12. Store devices at room temperature, or proceed immediately to mounting onto

glass slides for use with cells.

3.3 Mounting and seeding of devices

1. Prior to mounting, store glass slides overnight in 0.2 M hydrochloric acid (see Note 12).
2. Remove a device chip from packing tape and immediately prepare for cleaning.
3. Cut out holes for seeding ports and media reservoir into PDMS using biopsy punches (Fig. 2.1A, i and ii). Location of holes is marked on PDMS as part of the mask design. Media reservoirs are cut out using a 5 mm punch, while the seeding inlets should be cut out with a 1.2 mm punch (see Note 13).
4. Hold device with forceps and rinse with isopropyl alcohol (IPA), followed by deionized water. Repeat once (see Note 14).
5. Using pressurized air, dry device thoroughly, and then place inside of plasma cleaner, feature side up.
6. Repeat washing and drying steps on cover glass slides and place inside of plasma cleaner alongside device (see Note 15).
7. Close plasma cleaner and turn on pump and power switches. Wait a few minutes to allow the plasma cleaner to warm up, and then turn on the RF level (which regulates the intensity of plasma within the chamber) to High.
8. Plasma treat the PDMS devices and glass cover slides for five minutes, adjusting the air intake in order to keep the plasma active (a bright pink color) throughout the treatment procedure (see Note 16).

9. Turn off the plasma cleaner and release the air pressure very slowly.
10. Remove the treated glass slide and PDMS device from the plasma cleaner, and place the device onto the glass slide, feature-side down (see Note 17).
11. Using your thumb, press the device down firmly onto the glass slide. Press around the device to ensure that the whole device is firmly bonded to the glass cover slide (see Note 18).
12. To improve adhesion of the PDMS to the glass, place the bonded device onto a hot plate at 95°C for 5 minutes (see Note 19).
13. Remove the device from the hot plate and allow the device to cool for a few minutes, before spraying the outside of the device completely with ethanol, and moving the device into a cell culture hood.
14. Fill the media reservoirs with ethanol and allow the device to incubate for 10 minutes at RT for sterilization.
15. Remove ethanol from the device and rinse the media reservoirs three times with PBS for 5 minutes each. Each device will hold between 150 and 200 μL of fluid.
16. At this stage, the inside surfaces of the device can be functionalized with various biologically relevant coating, depending on the cell line to be used and the experimental goals. We use fibronectin or collagen coatings for most cell lines. To functionalize the inside of the device, fill devices with protein solution through seeding ports (Figure 2.1A, ii) and allow the coatings several hours to set to the device surface (see Note 20, Table 1).
17. Remove coating solution and rinse the inside of the device three times using

180 μ L of cell culture media applied to one of the reservoirs, allowing 5 minutes of incubation between each rinse.

18. Prepare cells for seeding into devices (see Note 21, Table 1).
19. Completely aspirate all media from devices, ensuring that bypass channels and device features are clear.
20. Pipette 6 μ L of cell suspension into the seeding port on the same side of the device as the bypass channel (Fig. 2.1A). Seed cells into the right port on left device, and left port on right device (see Note 22).
21. Check seeding of the cells underneath a bright field microscope. The cells should be distributed evenly across the front of the device constriction channels (Fig. 2.3A). If the cells are biased towards one end of the constrictions (Fig. 3B), aspirate cells from the device and repeat seeding process.
22. Slowly add 180 μ L of cell culture media into the media reservoir at the end of the device opposite from where cells were seeded (Fig. 2.1A, into top reservoirs). When media is added to one reservoir, it will flow through the constrictions and bypass channels to fill the reservoir on the opposite side. By adding media on the reservoir on the end of the device opposite the seeding channels, this prevents the inflow of media from pulling cells off of the glass and potentially pushing them prematurely into the constrictions.
23. Check cell seeding under microscope after this step to ensure that addition of media did not move cells from their original, uniformly seeded position.
24. Place the device with cells into a 37°C cell culture incubator and incubate until

ready to image.

3.4 Time-Lapse Imaging and Analysis of Cell Migration

Time-lapse imaging of cells requires a microscope with an incubation chamber to maintain optimal cell culture conditions (i.e., adequate temperature, CO₂ concentration, humidity) throughout the imaging process (see Note 23). When using fluorescence microscopy, the experiments may require some troubleshooting to determine suitable excitation intensity, imaging intervals, exposure times, and imaging duration to avoid phototoxicity caused by repeated imaging throughout the experiment. Here, we will briefly outline our analysis protocol for studying nuclear transit in confined migration, after a time series of migrating cells within these devices has been collected. Alternatively, cells can also be fixed within migration devices and processed with standard immunofluorescence staining techniques for further analysis of nuclear and cytoskeletal elements involved in nuclear translocation (see Note 24).

1. Place the migration device in the microscope incubation chamber and bring the cells into focus. We find that a single region of constrictions is best visualized under 20× magnification to measure transit times, but higher magnification may be required to capture subcellular dynamics.
2. Let the microscope with mounted migration device thermally equilibrate for 15-30 minutes to avoid drift of focus.
3. Set up image acquisition software to capture region of interest within the device at regular time intervals (minimum of 1 frame every 10 minutes, more frequent imaging may be necessary for faster migrating cells). Each device has

6 regions to capture, representing areas with different constriction sizes (three with $1 \times 5 \mu\text{m}^2$ constrictions, two with $2 \times 5 \mu\text{m}^2$ constrictions, and one with $15 \times 5 \mu\text{m}^2$ constrictions), and each chip contains two devices.

4. Acquire time-lapse image series of all regions of interest overnight (see Note 25).
5. Using ImageJ, or an equivalent image analysis software, define the nuclear perimeter of each cell throughout the time series of images. If using cells modified to express fluorescently labeled proteins within the nucleus, you may define the nuclear perimeter using an intensity threshold (see Fig. 4).
6. For each cell attempting to pass through a constriction, define the time point at which the cell has “committed” to enter the constriction. This can be done by noting when the front of the nucleus crosses an imaginary line parallel to the center of the constriction (see Fig. 2.4, and Note 26). Similarly, define the time point at which the nucleus has exited the constriction, either when the rear of the nucleus crosses a second imaginary line towards the rear of the constriction (successful pass, see Fig. 2.4), or when the nucleus backs out of the constriction, i.e., the front of the nucleus is no longer inside the region between the imaginary lines (unsuccessful attempt). For successful passes, the ‘transit time’ is defined as the time between the entry and exit point.
7. Repeat this process for cells in the $15 \mu\text{m}$ wide channels. This measurement is crucial when comparing different cell lines or treatment conditions, which may affect the overall motility of cells, regardless of nuclear confinement (see Note 27).

8. Normalize the transit time of cells moving through the 1 μm and 2 μm wide constrictions to the average transit time of cells under the same condition (genotype, treatment) moving through the 15 μm wide channels. This is considered the ‘normalized transit time’ and describes the effect of the nuclear confinement on the migration efficiency.
9. Compare normalized transit times between different constriction sizes (e.g. 1 μm vs. 2 μm wide constrictions), genotype, or treatment (e.g., LINC complex disruption vs. mock control) for analysis of migration times throughout the device.

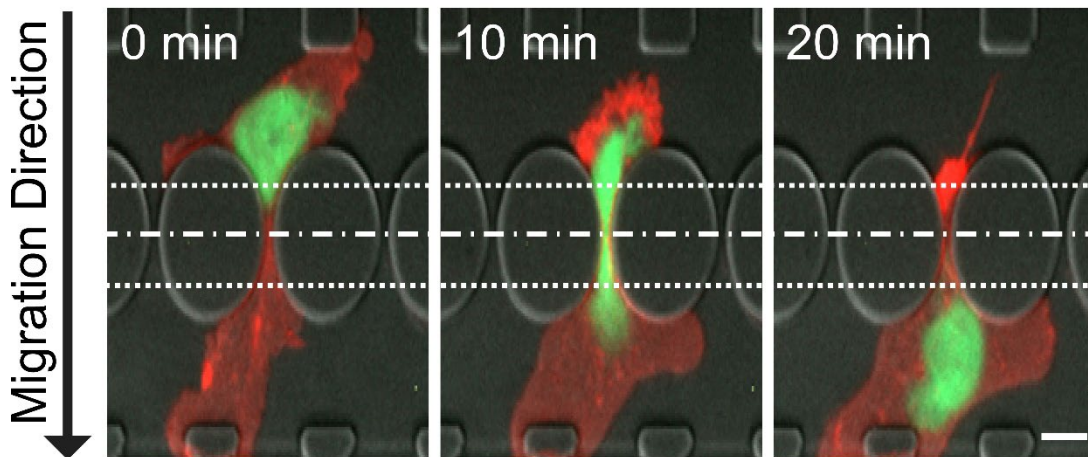


Figure 2.4. Analysis of nuclear transit time through constriction. Nuclear transit time is defined as the time for a cell to completely translocate its nucleus through a single constriction. The most robust metric for this measurement is the time from when the nucleus “commits” to enter a constriction (i.e., crossing an imaginary dashed line, located 7 μm outside the constriction center, top dashed line) and begins to deform, to when it has fully passed the constriction (i.e., the trailing edge of the nucleus has passed an imaginary line 7 μm past the constriction center, bottom dashed line). This analysis can be performed manually or using automated particle tracking programs. The example shows an MDA-MB-231 breast cancer cell expressing an mCherry-actin Chromobody and an mNeonGreen-H2B histone label. Scale bar 10 μm .

Notes

1. Most migratory cell lines should work well in these devices. We have had success with HT1080 fibrosarcoma cells, mouse embryonic fibroblasts, differentiated HL60 neutrophil-like cells, MDA-MB-231 metastatic breast cancer cells, and a variety of other invasive breast cancer cell lines.

2. MOS Cleaning is a 10 minute base dip in 1 part NH_4OH , 1 part H_2O_2 and 6 parts water for 10 minutes, DI water rinse and an acid dip in 1 part HCl , 1 part H_2O_2 and 6 parts water for another 10 minutes with a final DI water rinse.
3. It is important to slowly ramp up, and ramp down from the 3000 RPM top speed to ensure even spreading of the SU-8. The spin protocol we have found to be successful is: ramp up to 500 RPM at 100 RPM/sec for 10 sec, increase to 3000 RPM at 300 RPM/sec for 30 sec , then ramp down to 100 RPM at 100 RPM/sec for 30 sec before stopping.
4. This pre-exposure baking step removes excess solvents, improves the photoresistive profile of the SU-8, and prevents adhesion to the contact mask.
5. ABM Contact Aligner dose with long pass filter: 8.8 mW/cm^2 at 365 nm wavelength and 12.9 mW/cm^2 at 405 nm wavelength. Long pass filter is a PL-360LP from Omega Optical, or equivalent.
6. Tape may be forgone by using a cleanroom wipe with acetone to remove the freshly spun SU-8 from the alignment marks.
7. Same as in Note 2: ramp up to 500 RPM at 100 RPM/sec for 10 sec, increase to 1500 RPM at 300 RPM/sec for 30 sec, and ramp down to 100 RPM at 100 RPM/sec for 15 sec before stopping.
8. It may be possible to use shorter exposure times, but 1 minute exposure is typically sufficient to achieve good SU-8 feature sizes. The UV lamp intensity can decrease over its lifetime, and therefore the optimal exposure time for this step may vary. Over- or underexposure will affect the dimensions of the SU-8 features and of the final PDMS device. Thus, constriction dimensions should

be validated for new devices. This can be done by imaging the SU-8 features, or by filling the assembled PDMS devices with fluorescently labeled dextran or other fluorescent solution and acquiring confocal image stacks of the constriction channels.

9. In order to protect the silicon wafer and delicate SU-8 features from damage during regular device production, we recommend that the first set of PDMS cast migration devices is used to produce a secondary plastic mold. This plastic mold should then be used for subsequent reproduction of migration devices. Detailed notes on producing a secondary plastic mold can be found in Desai et al. (2009) (Desai et al., 2009).
10. Ensure that the mold sits completely flat in the oven to prevent PDMS from tilting during curing. Tilted devices can still be used; however the devices will vary in thickness and therefore will not be able to hold the same volume of cell media.
11. When using a secondary plastic mold to make devices, the PDMS can be immediately removed following baking. When using the silicon wafer as your device mold, be sure to allow the device to cool completely before proceeding to avoid damaging SU-8 features.
12. 0.2M hydrochloric acid (HCl) solution should be replaced on a weekly basis. Over time, HCl will evaporate, and devices will not properly adhere to glass slides.
13. During this step, be very careful with the placement of the punch-outs. The 1.2 mm punch sits between the bypass channel and the constrictions; interference

- with either will likely affect your results. It is also advised that you punch through the PDMS with the feature-side up to prevent poorly located cut-outs.
14. When rinsing device, hold device upward, above your hands and pour IPA and water downwards onto device. Otherwise, run-off of material from gloves may fall onto device and prevent adhesion between PDMS and the glass slide.
 15. During drying of cover glass with pressurized air, hold glass firmly and slowly increase air pressure, blowing parallel to the length of the glass to prevent bending and breaking of the glass.
 16. This will activate the surface of the PDMS, allowing better adhesion between the device features and the glass slide. Pay close attention and adjust air intake to keep plasma bright pink throughout cleaning, as we have found that poor device adhesion often results from poor plasma cleaning technique.
 17. At this stage, ensure that you do not touch the surface of the glass slide nor the device-side surface of the PDMS. Additionally, check orientation of the device constrictions and place very carefully, as you will not be able to adjust the orientation after it contacts the glass. Orientation of devices is entirely up to the user, but if mounting multiple devices on a single glass slide, analysis is generally easier if all cells are migrating in the same direction. Generally, we align the devices so that the cells will migrate “upward” (i.e., in the y-direction) while observing under a microscope.
 18. This step may take some trial and error: if the PDMS device is not pressed sufficiently firmly against the glass, some device features may not fully adhere to the glass. In this case, cells can migrate underneath the PDMS pillars

(Figure 2.3D). If the PDMS device is pressed too hard against the glass, the features may collapse, preventing cells from migrating through the device. We have found that gently pressing around the device perimeter, then evenly rolling one finger across the whole device with very light pressure works best.

19. At this step, the device can be inspected underneath a bright field microscope to see if the PDMS features are fully adhered. There will be a notably different color coming through regions of the device that are not bonded to the glass.
20. When coating, check the inside of the device for pockets of air bubbles, which may form during addition of protein solutions into the device. These air bubbles can form around constrictions, which can prevent the protein from coating these features. To eliminate the bubbles, vigorously pipette protein solution through the device. Optimal seeding densities of cells and concentrations of ECM solutions that we have determined are found in Table 2.1.

Table 2.1: Optimal cell seeding densities and concentrations of ECM coating to prepare migration devices

| Cell Line | Cells Seeded per Device | ECM Coating | ECM Incubation |
|---------------------------|--|---|---|
| HT1080 | 80,000 cells seeded minimum 2 hours before imaging | 50 µg/mL Corning 354236 Rat Tail Collagen Type I diluted in 0.02M Acetic Acid | 4°C overnight or longer |
| MDA-MB-231 on collagen | 50,000 seeded minimum 2 hours before imaging | 50 µg/mL Corning 354236 Rat Tail Collagen Type I diluted in 0.02M Acetic Acid | 4°C overnight or longer |
| MDA-MB-231 on fibronectin | 30,000 seeded 24 hours before imaging | 5 µg/mL Millipore FC010 Human Plasma Fibronectin diluted in PBS | 4°C overnight or longer, or 4 hours at 37°C |
| Human fibroblasts | 30,000 seeded 24 hours before imaging | 3 µg/mL Millipore FC010 Human Plasma Fibronectin diluted in PBS | 4°C overnight |

21. The exact number of cells to be seeded will be dependent on the specific cell line, and may require optimization depending on what cell density is desired for the experiments. We have found that seeding 30,000 MDA-MB-231 cells per device works well for live-imaging experiments. In order to concentrate this number of cells into 6 µL of cell suspension, cells should be suspended in media at a concentration of 5 million cells per mL.
22. Cells must be seeded slowly and steadily with the pipette. Pushing the cells into the device too quickly may lead to the cells spreading unevenly across the device (Fig. 3B). Additionally, when seeding cells, do not dispense the pipette past the first point of resistance; injection of air behind the cells results in the

formation of bubbles within the device and can hinder cell migration (Fig. 2.3C).

23. If necessary, HEPES or other buffers may be added to cell culture media to maintain pH balance, particularly for longer duration studies. To prevent evaporation of cell media, devices should be sealed with cover glass laid across the media reservoirs before moving to microscope. In experiments that run longer than 12 hours, it may be necessary to change cell culture media on a regular basis (typically every 24 hours).
24. Fixation and staining of cells can be performed using standard immunofluorescence protocols; however it is recommended that longer times are used for each incubation and washing step to ensure that reagents have sufficient time to distribute completely throughout the microfluidic device. For immunofluorescence studies, cells should be seeded at lower densities, as large numbers of cells can block up the entry to the constrictions channels, preventing staining reagents from reaching some cells within the devices. Alternatively, experiments can be performed with devices without covalently attaching the PDMS to the glass slides (i.e., without plasma treatment). In this case, the PDMS can be removed after fixing the cells inside the devices, and staining can be performed on cells adhering to the glass slide. The fixation step may require some optimization to identify conditions that promote cells to preferentially adhere to the glass cover slide and not the PDMS features.
25. Total imaging time is up to the user and depends on the cell line being used. For most cell lines, imaging overnight (12-14 hours) is sufficient to yield a

good number of cells passing through constrictions (10 – 30 cells per region of interest). For longer studies, it may be necessary to periodically replace cell media to keep cells healthy.

26. We have found that the most consistent measurement for a ‘point of commitment’, i.e. when a cell is attempting to pass through a constriction, is an imaginary line drawn 7 μm away from the centerline of the constrictions, towards the entry side (Fig. 2.4). Another imaginary line can be drawn on the opposite side centerline to define when the nucleus has fully passed through the constriction. It is also necessary to check image sequences for signs of potential issues with the constrictions, which would result in exclusion of the affected cells. For example, if it appears that some part of the nucleus or the cell body passes underneath the device pillars during migration, instead of in between the pillars that form the constriction, this indicates that the PDMS pillars were not sufficiently bonded to the glass and the nucleus is not fully confined.
27. As in Note 26, is also important to establish criteria for exclusion of particular cells migrating through the 15 μm channels. For example, when determining the migration speed or nuclear transit time of cells in the 15- μm wide channels, it may be necessary to exclude cells that spontaneously switch their migration direction, as this would affect the results.

**CHAPTER 3- CONTRACTION OF THE REAR CORTEX SUPPORTS
CONFINED MIGRATION THROUGH A PRESSURE INDUCED NUCLEAR
TRANSIT MECHANISM²**

Abstract

As cells migrate through biological tissues, they must frequently squeeze through micron-sized constrictions in the form of interstitial pores between extracellular matrix fibers and/or other cells. Although it is now well recognized that such confined migration is limited by the nucleus, which is the largest and stiffest organelle in the cell, it remains incompletely understood how cells apply sufficient force to move their nucleus through the constrictions. Here, we report a novel mechanism by which contraction of the cell rear cortex pushes the nucleus forward to mediate nuclear transit through constrictions. Laser ablation of the rear cortex reveals that pushing forces behind the nucleus are the result of increased intracellular pressure in the rear compartment of the cell. The pushing forces behind the nucleus depend on accumulation of actomyosin in the rear cortex and are abolished when inhibiting Rho-kinase (ROCK). Collectively, these results suggest a novel, additional mechanism by which cells generate elevated, intracellular pressure in the posterior compartment to facilitate nuclear transit through 3D constrictions.

Key words: Nucleus, Confined Migration, Invasion, Cortex, Mechanobiology;

Pressure

² Portions of this work are in preparation for submission as
Keys JT, Cheung B, Wu M, Lammerding J. (2022) Contraction of the Cell Rear Drives
Nuclear Translocation Through Confined Environments

Contributions: JT Keys performed all experiments, data analysis, and wrote text for this chapter. B Cheung assisted in set-up and interpretation of RhoA FRET experiments.

Introduction

The migration of cells through tissues is essential to many biological processes, including embryogenesis, immune surveillance, wound healing, and cancer metastasis (Doyle et al., 2013; Yamada and Sixt, 2019). During *in vivo* migration, cells must navigate through a confining, 3D environment of extracellular matrix fibers and layers of endothelial cells which form constrictions as small as 1 to 2 μm in diameter (Bone et al., 2016; Khatau et al., 2012; Weigelin et al., 2012; Wolf et al., 2013), which is substantially smaller than the size of the cell and the nucleus. To pass through these constrictions, cells must radically alter their shape. Although cells can readily alter their morphology through cytoskeletal reorganization, the deformation of the nucleus represents a unique physical challenge, as it is the largest and stiffest organelle in the cell (Caille et al., 2002; Denais et al., 2016; Khatau et al., 2012; McGregor et al., 2016; Wolf et al., 2013). Because of its size and stiffness, cells must generate substantial intracellular force to deform the nucleus through constrictions. The process of deforming and moving the nucleus through these narrow spaces, henceforth referred to as “nuclear transit,” limits the rate at which cells migrate in confined 3D environments (Davidson et al., 2015; Denais et al., 2016; Harada et al., 2014; Jayo et al., 2016; McGregor et al., 2016; Rowat et al., 2013; Thomas et al., 2015; Tollis et al., 2022; Wolf et al., 2013; Yadav et al., 2018).

Various mechanisms have been proposed to explain how cells accomplish nuclear transit through confined environments (Marks and Petrie, 2022; McGregor et al., 2016). One commonly described mechanism suggests that actomyosin and

intermediate filaments at the front of the cell pull the nucleus forward (Davidson et al., 2020; Jayo et al., 2016; Petrie et al., 2014). Other studies have implicated pushing forces, mediated through perinuclear actomyosin fibers, which wrap around the nucleus (Thomas et al., 2015), and Arp2/3-mediated perinuclear actin polymerization in the process (Thiam et al. 2016). Each of these mechanisms depend on physical connections between the nucleus and cytoskeleton. Another proposed mechanism suggests that the nucleus is pushed forward by contraction of actomyosin in the rear cortex of migrating cells (Hetmanski et al., 2019; Lämmermann et al., 2008; Lee et al., 2021; Mistriotis et al., 2019; Poincloux et al., 2011). Evidence of pushing forces behind the nucleus derive from the observation that cells migrating in 3D environments commonly accumulate actin in the trailing edge of the cell, and that contraction of the cell rear often precedes nuclear transit (Hetmanski et al., 2019; Lämmermann et al., 2008; Mistriotis et al., 2019; Thiam et al., 2016). However, functional evidence for this mechanism is still lacking, including how forces from the contraction of the rear cortex are transmitted to the nucleus. Lastly, many cell lines have shown the ability to migrate using multiple modes, such as adhesion-independent “amoeboid” migration and “mesenchymal” migration, depending on cellular contractility and environmental adhesiveness (Liu et al., 2015; Sahai and Marshall, 2003). This plasticity of migration modes suggests that it is possible that cells may similarly switch between nuclear transit mechanisms in differing biological contexts (Marks and Petrie, 2022).

Despite extensive previous research, several questions remain regarding the potential mechanism cells use to apply cytoplasmic forces to the nucleus during confined migration, including (1) how forces are transmitted from the contracting cell rear to the nucleus, and (2) to what extent contraction of the cell rear contributes to or is necessary for nuclear transit. Using microfluidic devices that mimic confined interstitial spaces, along with advanced imaging and cellular manipulation approaches, we here identified a novel mechanism by which actomyosin in the rear cortex contracts to push the nucleus forward through constrictions. This mechanism depends on elevated RhoA-ROCK signaling in the cell posterior, resulting in the colocalization of actin and active myosin in the rear cell cortex. Contraction of the rear cortex results in elevated intracellular pressure in the posterior compartment of the cell, which pushes the nucleus from behind to support migration through confined spaces.

Results

Contraction of the posterior actin cortex promotes nuclear transit through constrictions

To model cell migration through confining environments, we seeded cells into microfluidic devices that enables the close observation of nuclear transit through precisely defined constrictions at high spatiotemporal resolution (Davidson et al., 2015; Keys et al., 2018). In this device, cells migrate on a collagen-coated surface through constrictions measuring 1 to 2 μm in width and 5 μm in height ($\leq 2 \times 5 \mu\text{m}^2$), formed by poly-dimethyl siloxane (PDMS) pillars (**Fig. 3.1A**). The device also

features wider control channels ($15 \times 5 \mu\text{m}^2$) that do not require substantial nuclear deformation during migration (**Fig. 3.1A**) (Davidson et al., 2015). The size of the narrow constrictions reflects the geometries of small pore sizes that migrating cancer cells encounter *in vivo* (Weigelin et al., 2012), while the width of the control channels was chosen to be wider than the typical diameter of nuclei (Lammerding, 2011) and corresponds to the upper range of interstitial spaces (Weigelin et al., 2012). We have previously demonstrated that the $5 \mu\text{m}$ height is sufficient to vertically confine migrating cells, and that cells adhere to both top and bottom surfaces of the cell, plus the vertical walls (Davidson et al., 2015, 2014), thereby creating true 3D confined environments that model confined migration *in vivo* (Denais et al. 2016; Wang et al. 2022). These devices provide several advantages over imaging cells migrating through collagen matrices, as they enable long-term imaging of cells migrating along a single focal plane, through precisely defined constriction geometries. In contrast, *in vitro* assembled collagen matrices have heterogeneous, randomly distributed constriction geometries and often lead to cells migrating out of the imaging plane during prolonged image acquisition series.

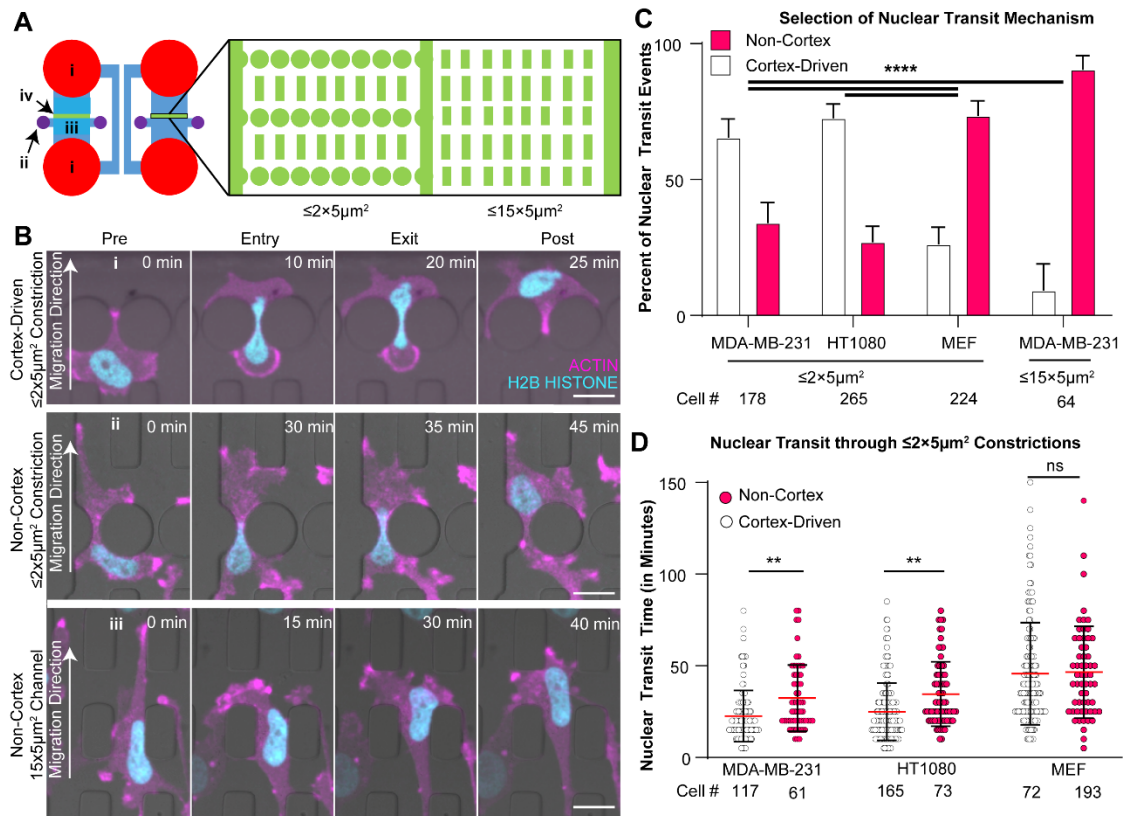
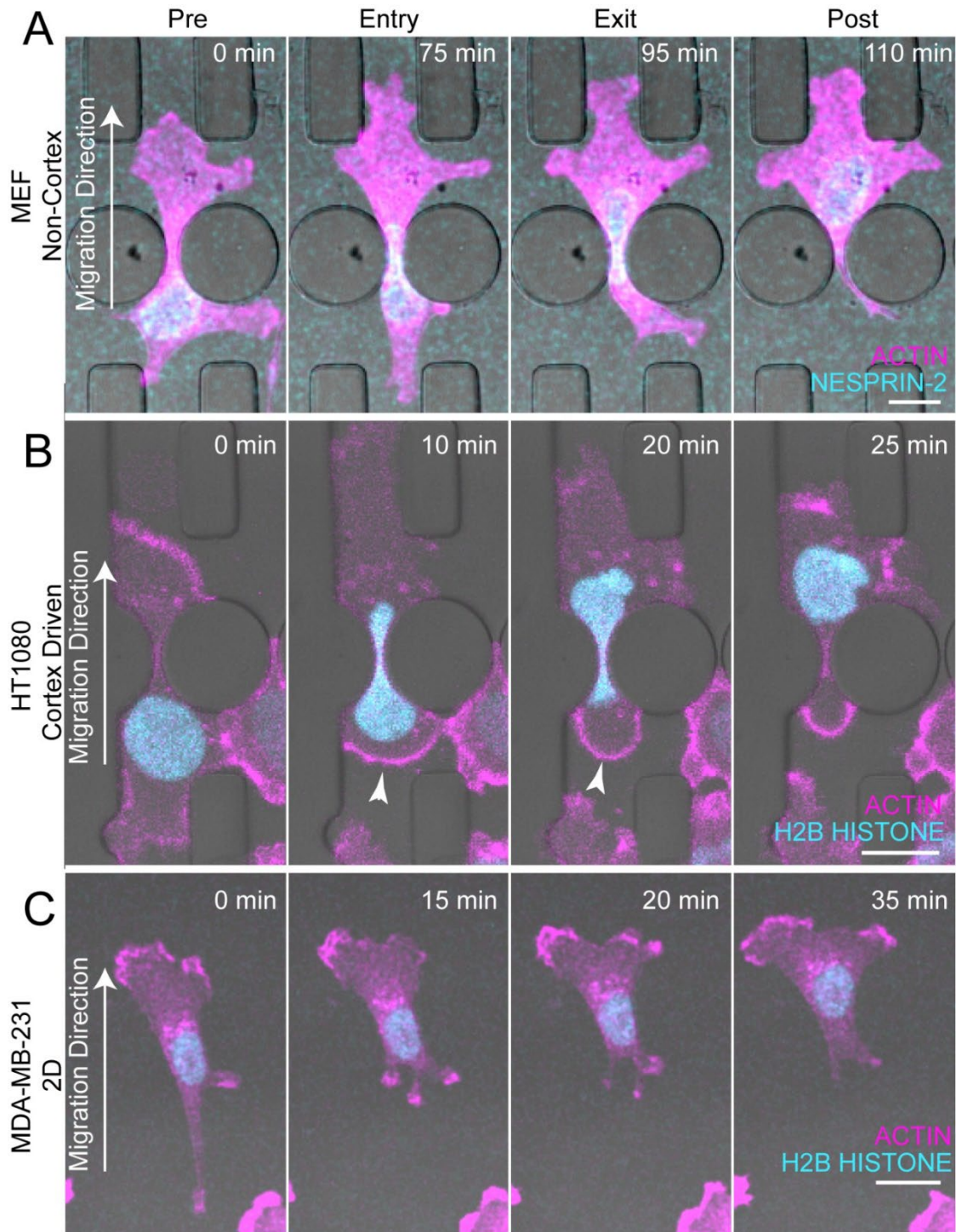


Figure 3.1. Cortex-driven nuclear transit provides an advantage to cells migrating through narrow constrictions. (A) Schematic layout of microfluidic device used to study confined migration through precisely defined constrictions. (i) Reservoirs for cell media; (ii) seeding ports to add cells; (iii) seeding area where cells attach prior to migration through constrictions; (iv) constriction area, shown in detail in inset, to the right. (B) MDA-MB-231 cells adopt varying morphological characteristics as the nucleus squeezes through microfluidic constrictions using either (i) a rear cortex-driven mechanism, or (ii) a non-cortex driven mechanism. Scale bar: 20 μm . (C) Relative frequency of cortex-driven and nuclear transit mechanisms in varying cell types migrating through either narrow constrictions ($\leq 2 \times 5 \mu\text{m}^2$) or wider control channels ($15 \times 5 \mu\text{m}^2$). Error bars represent 95% confidence intervals. ****, $p < 0.0001$, based on a Chi-Squared test of independence. (D) Nuclear transit times through $\leq 2 \times 5 \mu\text{m}^2$ constrictions of different cell types, subdivided into cortex-driven and non-cortex driven

nuclear transit mechanisms. Red line represents sample mean. Error bars represent standard deviation. **, $p < 0.01$, ****, $p < 0.0001$, based on one-way ANOVA.



Supplementary Figure 3.2: Nuclear transit mechanisms depend on cell type and confinement. Representative time-lapse series of different cell morphologies observed during nuclear transit of MEF (top) and HT1080 (middle) cells in microfluidic devices and MDA-

MDA-MB-231 cells (bottom) migrating on a collagen-coated glass cover slip. MEF cells tend to use a non-cortex driven mechanism (top) in contrast to HT1080 cells, which use a cortex-driven mechanism (middle; arrows) while passing through narrow constrictions in the microfluidic migration devices. The cortex-driven mechanism used by MDA-MB-231 cells in Fig. 3.1B is unique to confined environments and is not observed during migration on collagen-coated 2D glass substrates (bottom). Scale bars: 20 μm .

Movie 3.1: MDA-MB-231 cells use a cortex-driven mechanism to support nuclear transit through constrictions. Representative time-lapse sequence of an MDA-MB-231 cell expressing mCherry2-Actin chromobody (magenta) and mNeonGreen-H2B Histone (cyan) transiting through a $\leq 2 \times 5 \mu\text{m}^2$ constriction by contracting the rear cortex to push the nucleus forward. Scale bar: 10 μm

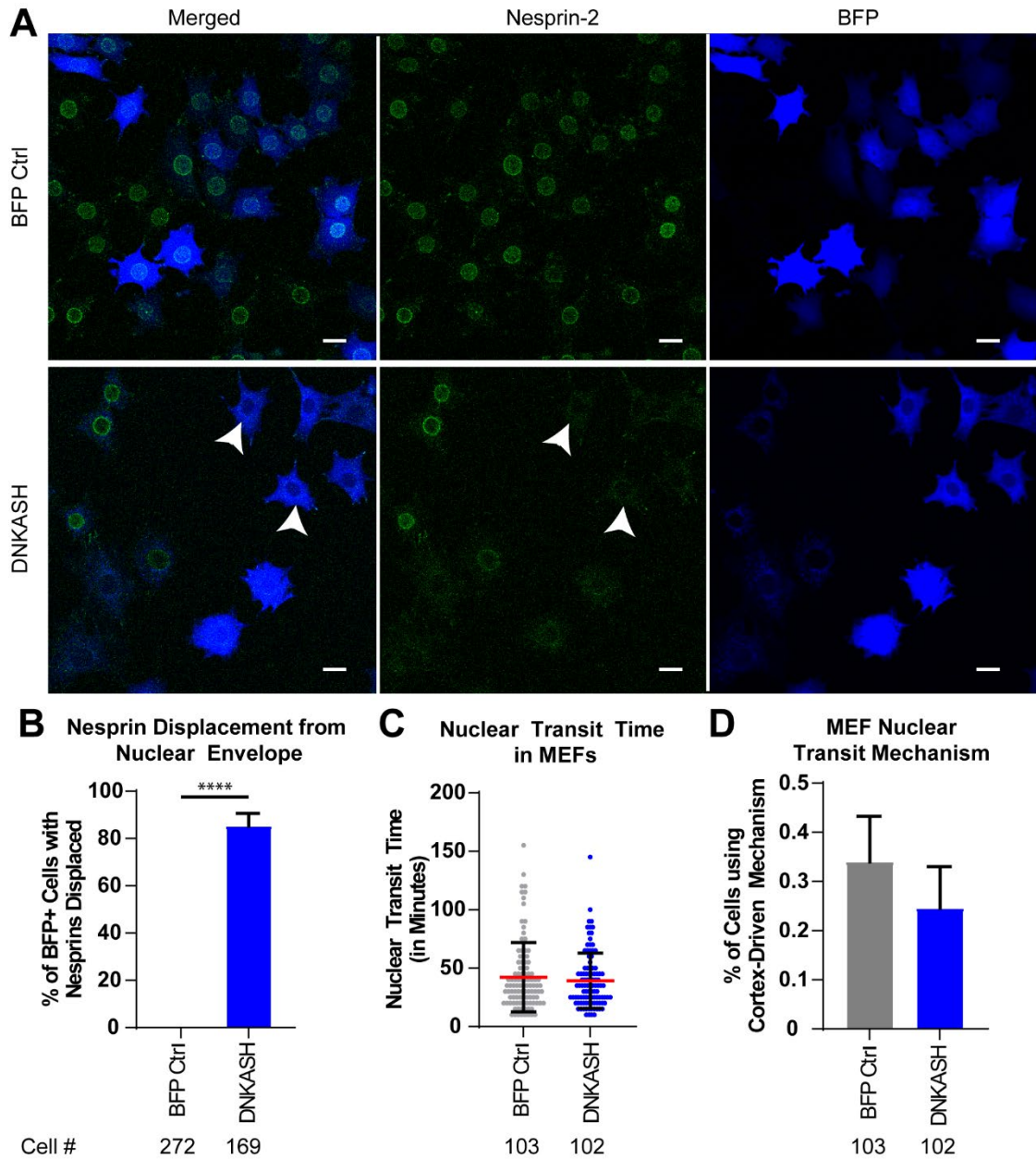
Movie 3.2: MEF cells complete nuclear transit without contracting the rear cortex. Representative time-lapse sequence of a MEF expressing mCherry2-Actin chromobody (magenta) and GFP-Nesprin-2 (cyan) transiting through a $\leq 2 \times 5 \mu\text{m}^2$ constriction forming actin fibers that pull at the leading edge of the nucleus. Scale bar: 10 μm

We chose to study MDA-MB-231 metastatic breast cancer cells, because they exhibit the ability to switch between different migration modes, and therefore may use multiple mechanisms to drive nuclear transit (Geiger et al., 2019; Sahai and Marshall, 2003). MDA-MB-231 cells stably expressing fluorescently labeled histones (mNeonGreen-H2B Histone (Davidson et al. 2015)) and actin (mCherry2-actin chromobody (Chromotek)) exhibited two distinct patterns of actin accumulation around the nucleus while migrating through constrictions in microfluidic migration

devices. Most cells formed a rounded, actin-enriched cortex in the rear of the cell, which's contraction was associated with the nucleus squeezing through the constriction (**Fig. 3.1B-i, Movie 3.1**). In other cells, the nucleus transited through the constriction without the cell forming a rounded rear cortex (**Fig. 3.1B-ii**). Notably, whereas the formation of the rear cortex was observed in the majority of MDA-MB-231 cells migrating through narrow constrictions, it was rarely observed in cells migrating through the larger control channels, nor in cells migrating on 2D glass substrates (**Fig. 3.1B-iii, 3.1C, Supp. Fig. 3.1C**). We observed similar patterns of actin accumulation in MDA-MB-231 cells migrating through 3-dimensional collagen matrices (**Supp. Fig. 3.1**), indicating that these nuclear transit mechanisms are relevant during migration in vivo. We hypothesized that the differences in cytoskeletal organization prior to and during nuclear transit indicate two distinct nuclear transit mechanisms, which may correspond with the previously described “pushing” and “pulling” forces. Accumulation of actin in the rear cortex suggests a “cortex-driven” pushing of the nucleus from behind, whereas accumulation of actin in front of the nucleus suggests “non-cortex-driven” pulling at the front of the nucleus. We recorded similar actin dynamics in HT1080 fibrosarcoma cells in microfluidic migration devices (**Fig. 3.1C, Supp. Fig. 3.2B**), another cancer cell line that shows considerable plasticity in its migratory mode (Petrie et al., 2016; Wolf et al., 2003). In contrast, mouse embryonic fibroblasts (MEFs), which tend to use a mesenchymal migration mode (Gadea et al., 2007), predominantly used a non-cortex driven nuclear transit mode (**Fig. 3.1C, Supp. Fig. 3.2A, Movie 3.2**).

Based on these observations, we hypothesized that the rear cortex contraction may aid MDA-MB-231 and HT1080 cells in nuclear transit through narrow constrictions by applying a “pushing” force to the nucleus from the back of the cell. To determine whether the rear cortex contraction produced more rapid nuclear transit, we compared the transit times between cells using either (rear) cortex-driven or non-cortex driven nuclear transit for each of the cell lines. In MDA-MB-231 and HT1080 cells, cortex-driven cells translocated their nuclei significantly faster through narrow constrictions than non-cortex-driven cells (**Fig. 3.1D**), suggesting that in these cell types, the rear cortex contractions provides an advantage over non-cortex driven migration. In contrast, we did not find any differences in nuclear transit time in in MEFs using either the cortex or non-cortex driven mechanism (**Fig. 3.1D**). The preference towards a cortex-driven mechanism seen in MDA-MB-231 and HT1080 cells, in contrast to MEFs, may be due to the greater migratory plasticity that is commonly observed in these cancer cell lines (Sahai and Marshall 2004). As MDA-MB-231 and HT1080 cells are capable of migrating using both mesenchymal and amoeboid migration modes, depending on environmental and biological factors, they may be able to use this additional cortex-driven nuclear transit mechanism to support passage through narrow constrictions. MEFs, in contrast, are more conventionally mesenchymal in their migration (Gadea et al. 2007), and therefore may be less able to use this additional migration mechanism. Taken together, these results suggest that rear cortex contraction may act as an alternative or supplemental mechanism in confined migration, which enables more rapid migration through constrictions but is not necessarily required for nuclear transit.

Since previous studies had suggested that pulling forces at the leading edge of the nucleus require connections between the nucleus and cytoskeleton (Petrie et al. 2014, Davidson et al. 2021), we investigated whether disruption of the linker of nucleoskeleton and cytoskeleton (LINC) complex caused a switch to a cortex-driven nuclear transit mechanism. MEFs expressing GFP-Nesprin-2 (Davidson et al. 2021) and mCherry2-Actin chromobody were transfected with a BFP-tagged dominant-negative KASH construct (DN-KASH), which binds with Sun proteins at the nuclear envelope and prevents the association between Sun proteins and endogenous Nesprin proteins, thereby disrupting force transmission between the cytoskeleton and nucleus (Lombardi et al. 2011). Whereas GFP-Nesprin-2 was localized to the nuclear envelope in non-modified cells and in cells expressing the BFP-control constructs, in DN-KASH expressing MEF cells, Nesprin-2 was mislocalized from the nuclear envelope to the ER (**Supp. Fig. 3.3A & B**), confirming disruption of the LINC complex by the DN KASH construct. Surprisingly, LINC complex disruption did not correspond with increased nuclear transit times, nor in a shift towards a cortex-driven mechanism (**Supp. Fig. 3.3C & D**). These findings suggest that nuclear transit can be accomplished in the absence of the LINC complex, and neither cortex-driven nor non-cortex driven nuclear transit mechanisms require an intact LINC complex.



Supplemental Figure 3.3: Disruption of the LINC Complex does not alter migration rate or nuclear transit mechanism in MEFs. (A) MEFs expressing GFP-Nesprin-2 and cytoplasmic BFP or BFP-tagged DN-KASH constructs. Arrows point to DN-KASH-expressing cells with Nesprin-2 displaced from the nuclear envelope. Scale bar: 20 μ m. (B) Percentage of BFP-expressing MEFs with Nesprin-2 displaced from the nuclear envelope.

****, $p < 0.0001$ based on Chi-squared test. (C) Nuclear transit times of MEFs migrating through $\leq 2 \times 5 \mu\text{m}^2$ constrictions. (D) Nuclear transit mechanism used by MEFs migrating through $\leq 2 \times 5 \mu\text{m}^2$ constrictions. Cell counts for each group listed below graphs. Results collected from two independent experiments. Differences between groups in panels C and D were not statistically significant.

Pushing forces behind the nucleus are generated by actomyosin contraction in the rear cortex

We hypothesized that cortex-driven cells localize contractile machinery to the rear cortex to push the nucleus through constrictions. Previous studies found that non-muscle myosin II is important for force generation during 3D confined migration (Davidson et al., 2020; Thomas et al., 2015); thus, we performed time lapse video microscopy on MDA-MB-231 cells transfected to express GFP-myosin IIA and mCherry-myosin IIB in the migration devices. Both myosin II isoforms localized to the rear cortex of cells as the nucleus squeezed through constrictions (**Fig. 3.2A**). Notably, the accumulation of myosin II at the rear cortex was only observed in cells migrating through narrow constrictions, whereas in cells migrating through larger control channels or on 2D surfaces, i.e., in situations not utilizing rear-cortex driven nuclear transit, myosin II was localized to the front of the cell body or the leading edge of the nucleus (**Fig. 3.2A, Supp. Fig. 3.4A-B**). Importantly, our studies also revealed that individual cells can switch between non-cortex-driven and cortex-driven mechanisms during nuclear transit. In some instances, cells that entered constrictions with GFP-myosin II initially primarily localized at the leading edge of the nucleus

failed to pass through constrictions. When the nuclear transit attempt was not successful, the cells backed out of the constriction, and re-entered the constriction with GFP-myosin IIA localized to the rear cortex, using rear cortex contraction to successfully push the nucleus through the constriction (**Movie 3.3**). These findings suggest that cells may actively choose between nuclear transit modes while squeezing through constrictions.

To map myosin activity, rather than just the distribution of myosin, we immunofluorescently labeled cells fixed inside the microfluidic devices for phosphorylated myosin light chain (pMLC), an indicator of active actomyosin contractility. Cells in which the nucleus had just begun to enter the narrow constrictions displayed characteristic pMLC localization at the rear cortex of cells, indicating that the rear cortex actively contracts with the onset of nuclear transit (**Supp. Fig. 3.4C**). Importantly, the localization of pMLC to the rear cortex was only observed in cells undergoing nuclear transit through narrow constrictions, and was not seen in cells migrating through wider control channels or on 2D substrates, consistent with our prior observations that cells only use the cortex-driven mechanism when encountering small constrictions (**Supp. Fig. 3.4C**). Of note, pMLC was also found at the leading edge of the nucleus, suggesting that cortex-driven cells may also apply complimentary pulling forces at the leading edge of the nucleus or that myosin II activity is required for the protrusion and extension of the leading edge (**Supp. Fig. 3.4C**).

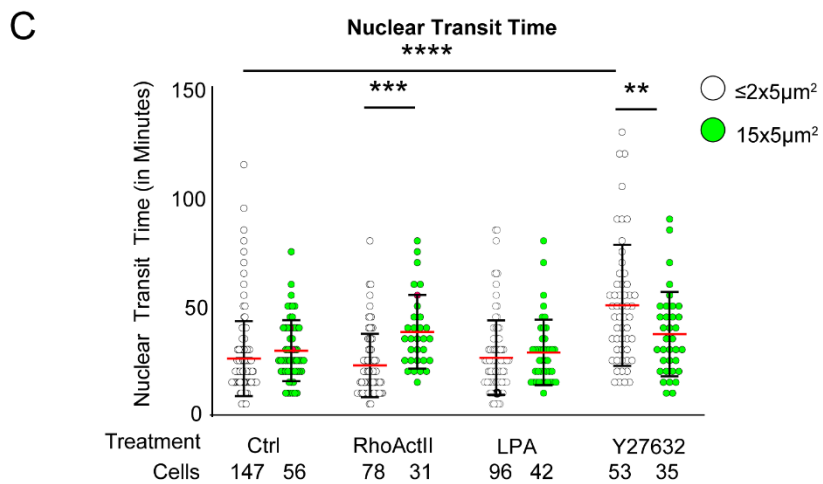
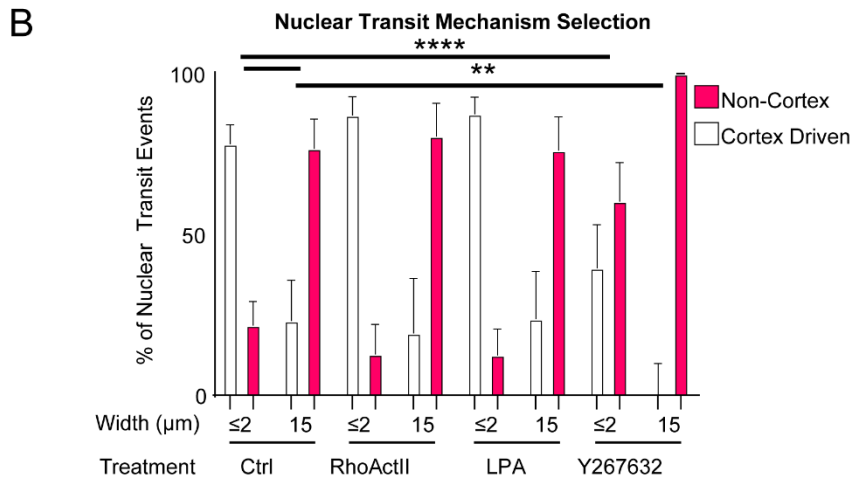
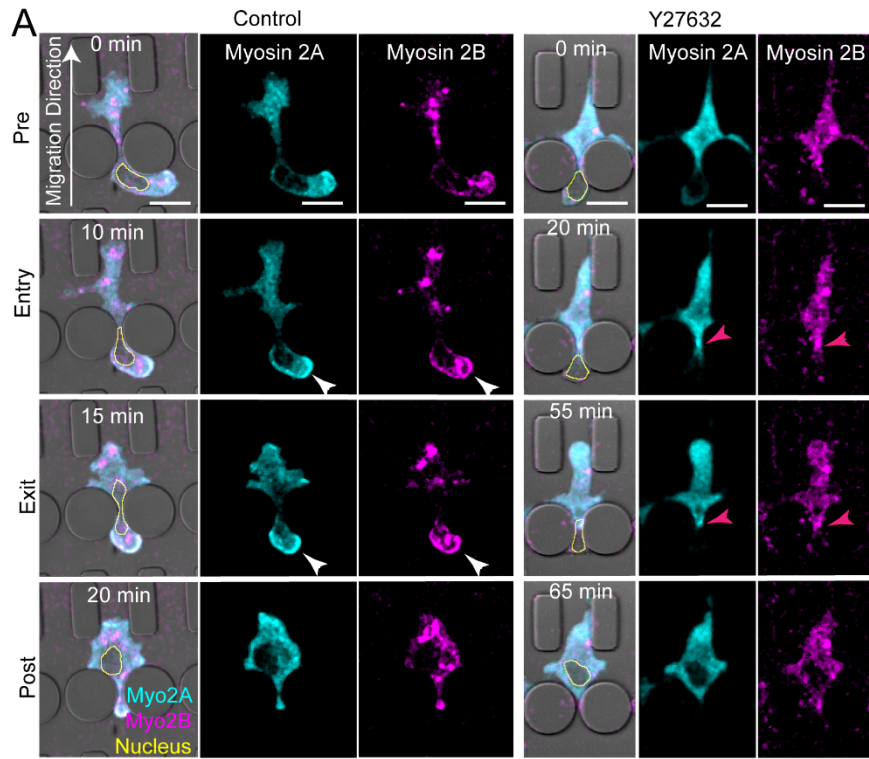
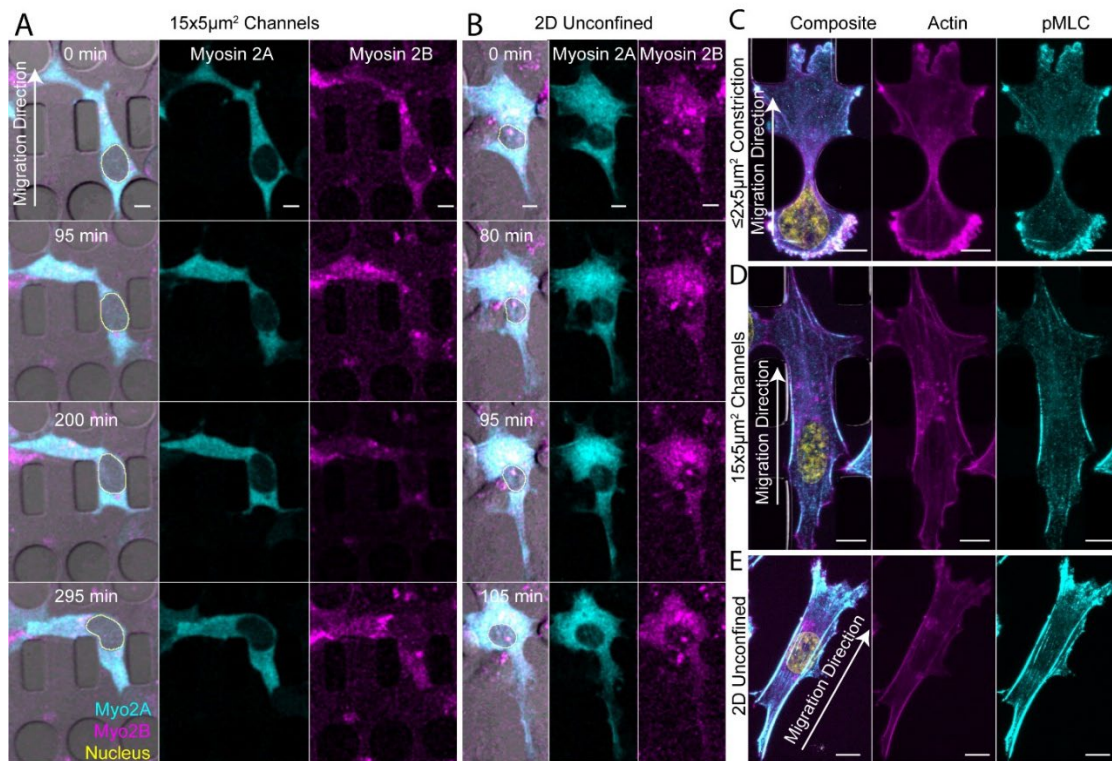


Figure 3.2: Rear cortex driven nuclear transit is associated with localization of myosin II to the rear cortex. (A) Representative time-lapse series of MDA-MB-231 cells expressing GFP-myosin IIA and mCherry-myosin IIB migrating through microfluidic migration devices. White arrows indicate accumulation of myosin II at the rear cortex. Magenta arrows point to accumulation in front of the nucleus. The nucleus is outlined in yellow for better visibility in the merged image. Scale bars: 20 μm (B) Percentage of nuclear transit events using cortex-driven or non-cortex driven modes in either $\leq 2 \times 5 \mu\text{m}^2$ or $15 \times 5 \mu\text{m}^2$ constrictions following treatment with either RhoA activators (RhoActII or LPA), ROCK inhibitor (Y27632), or vehicle control. Error bars represent 95% confidence intervals. **, $p < 0.01$, ****, $p < 0.0001$ using a Chi-Squared Test of Independence. (C) Nuclear transit times of MDA-MB-231 cells migrating through constrictions following treatment with RhoA activators (RhoActII or LPA) or ROCK inhibitor (Y27632). Red line represents mean. Error bars represent standard deviation. **, $p < 0.01$, ***, $p < 0.001$, ****, $p < 0.0001$ using a one-way ANOVA. Number of cells in each group indicated below the graphs.



Supplementary Figure 3.4: Localization of myosin II to rear cortex is unique to MDA-MB-231 cells migrating through narrow constrictions and not observed during migration through $15 \times 5 \mu\text{m}^2$ control channels or on 2D surfaces. (A) Representative time lapse imaging series of MDA-MB-231 cells expressing GFP-myosin IIA and mCherry-myosin IIB migrating through $15 \times 5 \mu\text{m}^2$ control channels. (B) Representative time lapse series of MDA-MB-231 cells expressing GFP-myosin IIA and mCherry-myosin IIB migrating on collagen coated glass coverslips. (C) MDA-MB-231 cells fixed inside $\leq 2 \times 5 \mu\text{m}^2$ constrictions (“3D confined”), $15 \times 5 \mu\text{m}^2$ control channels (“3D unconfined”), or on a 2D glass coverslip, and fluorescently labeled with Hoechst (DNA), Phalloidin (Actin), and antibodies against pMLC. Scale bars: 10 μm .

Movie 3: MDA-MB-231 cells can dynamically change nuclear transit modes during migration through constrictions. Representative time-lapse sequences of an MDA-MB-231

cell expressing GFP-Myosin IIA (cyan) and mCherry-Myosin IIB (magenta) migrating through a $\leq 2 \times 5 \mu\text{m}^2$ constriction. Upon first entering the constriction, myosin II localizes to the leading edge of the nucleus, suggesting a non-cortex driven nuclear transit mechanism. After failing to complete transit, the cell backs out of the constriction, myosin II re-localizes to the rear cortex, and the cell passes through the constriction in a cortex-driven mode.

Since myosin contractility is regulated through RhoA and Rho-associated protein kinase (ROCK) (Ridley 2003), we hypothesized that cells locally activate RhoA in the rear cortex to generate actomyosin contractile forces to push the nucleus from behind. To record the spatiotemporal dynamics of RhoA activation during nuclear transit, we stably modified MDA-MB-231 cells with a previously established FRET-based biosensor for RhoA activation (Pertz et al., 2006) and imaged the cells as they migrated through constrictions. Local RhoA activity was determined by measuring the average FRET ratio in either the rear cortex, front cortex, or directly in front of the nucleus (**Supp. Fig. 3.5A**). Since levels of the RhoA sensor inside the nucleus were very low, as expected, which could negatively affect the robustness of ratiometric FRET analysis, the nucleus was masked-out and excluded from the analysis (**Supp. Fig. 3.5A**). FRET ratios of the RhoA biosensor were evaluated prior to nuclear transit (“Pre”), during nuclear entry into a constriction (“Entry”), immediately upon nuclear exit from the constriction (“Exit”), and after the cell had left the constriction (“Post”) (**Fig. 3.3A**). In cells migrating through narrow constrictions, RhoA activity was elevated in the rear cortex relative to the rest of the cell body throughout nuclear transit (**Fig. 3.3B**). Of note, RhoA activity in the rear cortex was unique to cells

migrating through narrow 3D constrictions and was not observed in cells migrating through the wider control channels or on 2D substrates (**Supp. Fig. 3.5B**). RhoA activity in the rear cortex increased as the nucleus entered the constriction, and then returned to baseline levels during the later stages of nuclear transit (**Fig. 3.3C**). Unlike RhoA activity at the rear cortex, RhoA activity in the front cortex remained constant throughout nuclear transit (**Supp. Fig. 3.5D**). RhoA activity in front of the nucleus (**Supp. Fig. 3.5A, yellow zone**) did not increase upon nuclear entry into the constriction but increased at the end of nuclear transit (**Supp. Fig. 3.5C**). Collectively, these observations suggest a sequential process in which RhoA is first activated at the posterior of the cell, causing contraction of actomyosin in the rear cortex to push the nucleus into a constriction, followed by activation of RhoA in front of the nucleus to contract actomyosin at the leading edge of the nucleus to pull the nucleus through the constriction.

As the cortex-driven nuclear transit mechanism was associated with active RhoA and myosin II in the rear cortex, we hypothesized that the cortex-driven nuclear transit mechanism would depend on the level of Rho-ROCK activity. We treated cells with either ROCK inhibitor (Y27632) or RhoA activators (LPA or RhoA Activator II) and measured nuclear transit times in the microfluidic devices. ROCK inhibitor treatment significantly slowed nuclear transit through the constrictions but did not slow migration through unconfined channels (**Fig. 3.2C**), suggesting that ROCK activity is particularly important for confined migration. Interestingly, ROCK inhibition increased the frequency of non-cortex driven nuclear transit events and altered

localization of myosin IIA and IIB during nuclear transit, causing myosin to localize towards the front of the nucleus, rather than in the rear cortex as is seen in vehicle control cells (**Fig. 3.2A-B**). As ROCK inhibition slowed down nuclear transit through narrow constrictions but not through unconfined channels, this also suggests that the role of ROCK in pushing the nucleus from behind is unique to nuclear transit through narrow constrictions. This mirrors our earlier observation that cells in unconfined channels rarely use a cortex-driven migration mode. Ectopic activation of RhoA with either LPA or RhoA Activator II had no effect on the nuclear transit rate or nuclear transit mechanism in MDA-MB-231 cells (**Fig. 3.2C**). The lack of impact of RhoA activators on nuclear transit rate or mechanism may indicate that RhoA in these cells was already highly activated by FBS in the cell media, or that global RhoA activation without spatial control within the cell is insufficient to activate the cortex-driven transit mechanism. Although actomyosin contractility likely plays a role in both cortex-driven and non-cortex driven mechanisms, these results further suggest that cortex-driven nuclear transit requires a particularly high level of Rho-ROCK mediated contractility in contrast to non-cortex driven nuclear transit.

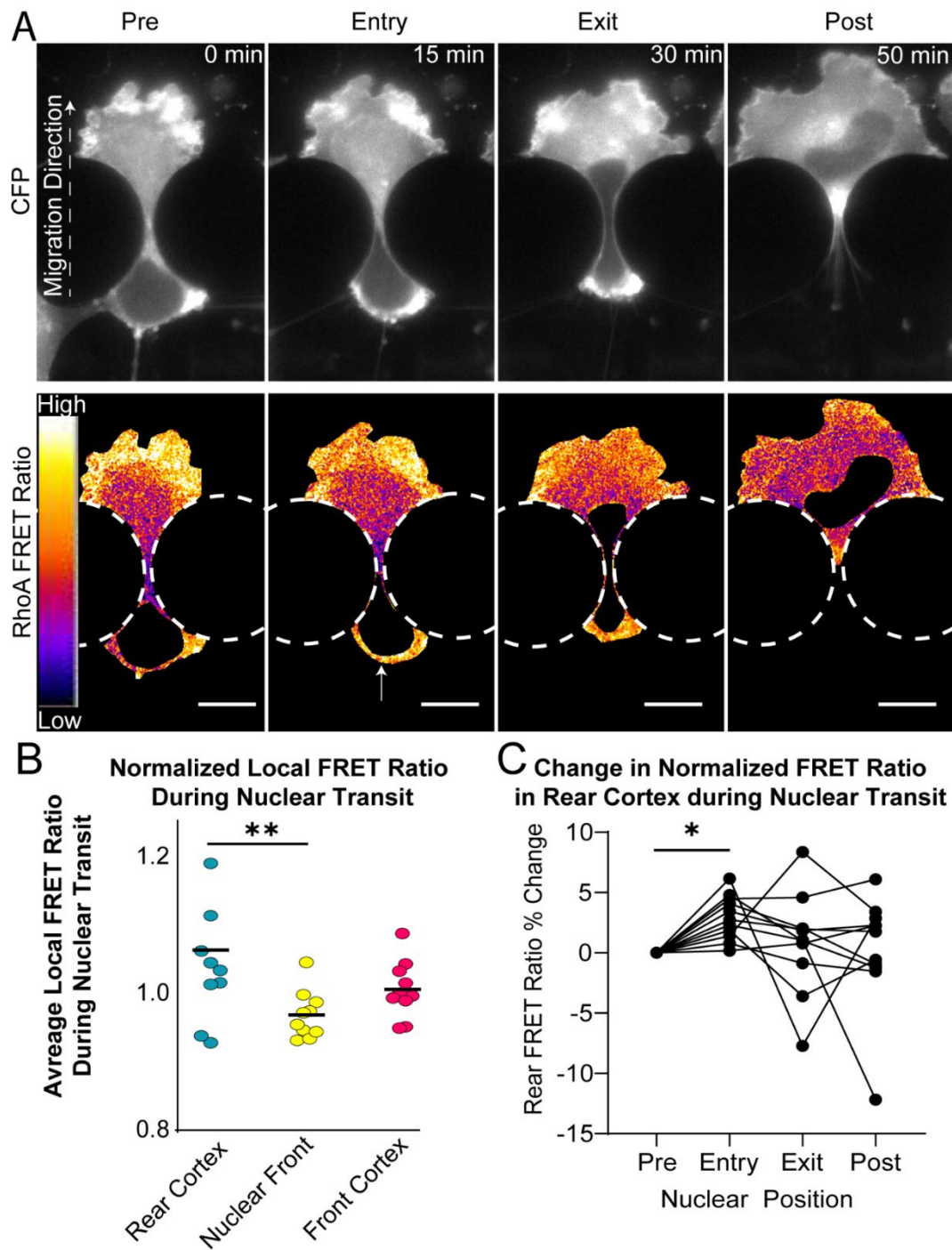
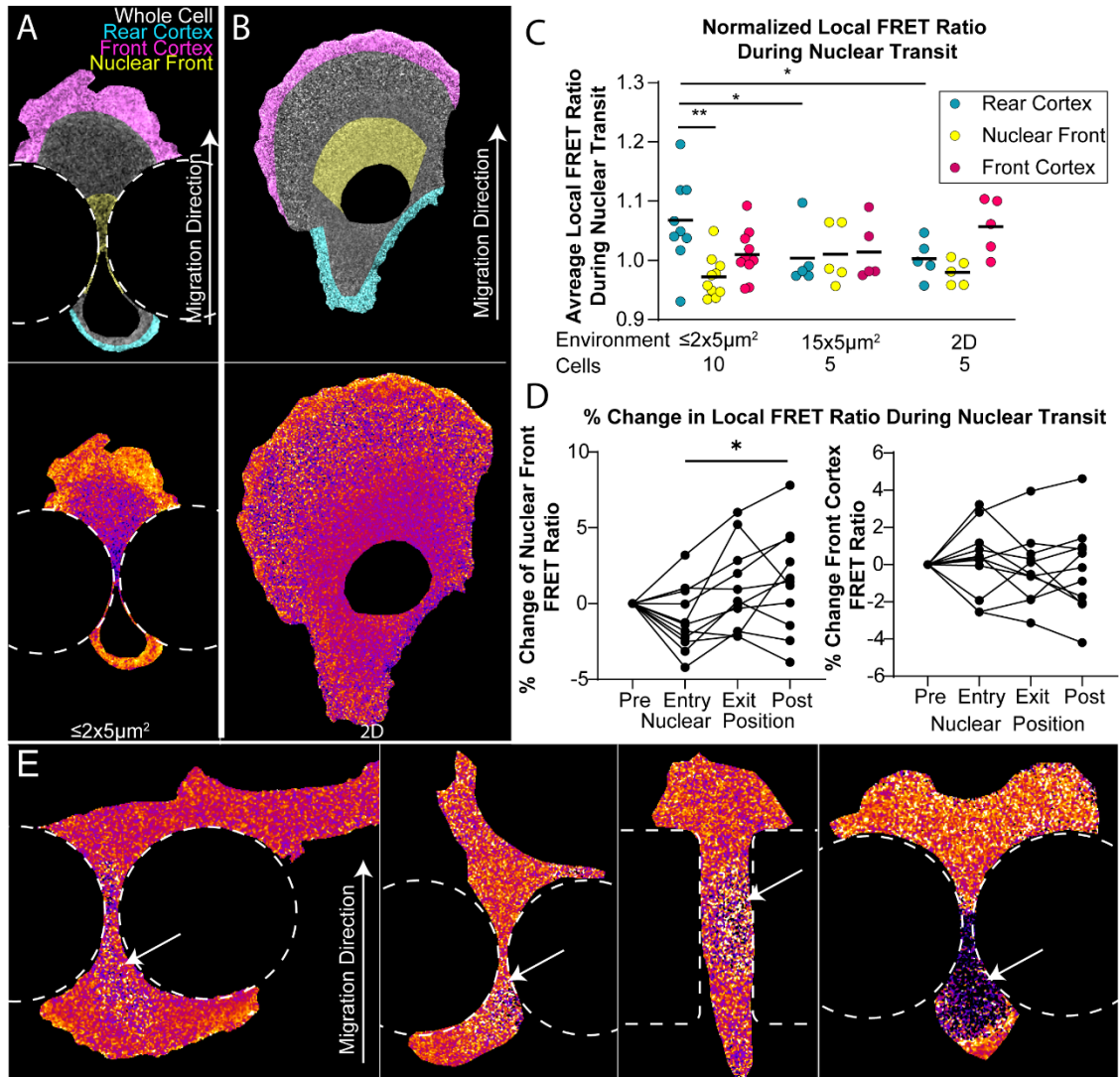


Figure 3.3. Cortex-driven nuclear transit is associated with increased RhoA activity at the rear cortex. (A) Representative time lapse series of FRET ratio of MDA-MB-231 cell expressing RhoA-FRET biosensor migrating through a microfluidic constriction. The bottom series shows the RhoA-FRET ratio during nuclear transit, illustrating increased RhoA activity

at the rear cortex (arrow) and the leading edge of the cell. Scale bars: 20 μm **(B)** Comparison of RhoA activity at different intracellular locations based on the recorded RhoA-FRET values for cells migrating through $\leq 2 \times 5 \mu\text{m}^2$ constrictions. Each data point represents local RhoA FRET measurements averaged across all time points during a single nuclear transit event. Black lines represent the mean for each group. **, $p < 0.01$ using paired non-parametric Wilcoxon test. **(C)** Time course of FRET ratio within rear cortex of individual cells (normalized to average FRET ratio of whole cell) at each phase of nuclear transit through $\leq 2 \times 5 \mu\text{m}^2$ constrictions. *, $p < 0.05$ using paired non-parametric Wilcoxon test.



Supplementary Figure 3.5. Distribution of active RhoA differs in cells migrating in 2D and 3D. Localization analysis of RhoA-FRET sensor for cells migrating (A) through $\leq 2 \times 5 \mu\text{m}^2$ constrictions, or (B) on a 2D glass coverslip. Greyscale image is highlighted in color for measurement regions for “Rear Cortex” (cyan), “Front Cortex” (magenta), or “Nuclear Front” (yellow). Heat map of measured FRET ratio for each cell is shown below. (C) Average FRET ratio in each local region normalized to average FRET ratio of whole cell grouped by environmental conditions. Black lines represent the mean for each group. **, $p < 0.01$ using paired non-parametric Wilcoxon test for comparisons within individual cells. *, $p < 0.05$ using

unpaired non-parametric Kruskal-Wallis test comparing cells in different conditions. **(D)** Time course of FRET ratio in Nuclear Front and Front Cortex regions in individual cells normalized to average FRET ratio of whole cell during each phase of nuclear transit through an individual constriction **(E)** Representative images of FRET ratios of RhoA-FRET expressing MDA-MB-231 cells without nuclear masking. Arrows point to the location of the cell nucleus.

Laser ablation of the cell cortex reveals a pressure-driven nuclear transit mechanism

Having established that cortex-driven cells localize actomyosin and active RhoA to the rear cortex at the beginning of nuclear transit, we hypothesized that contraction of the rear cortex pressurizes the rear compartment of the cell relative to the front compartment, pushing the nucleus forward through the constriction. To probe differences in intracellular pressure generated by rear cortex contraction, we used a two-photon laser to ablate specific cytoskeletal regions of migrating cells while they squeezed their nucleus through microfluidic constrictions (**Fig. 3.4A**). As the nucleus transits through a constriction, the cytoskeletal forces pushing or pulling on the nucleus are counteracted by the resistance of the constriction in the form of the friction and the normal forces at the interface between the nucleus and the constriction (**Supp. Fig. 3.6B-C**).

Targets for laser ablation were selected based on previously hypothesized roles in applying pushing or pulling forces on the nucleus during nuclear transit, including: (i) perinuclear actin filaments at the leading edge of the nucleus (“Nuclear Front”), which pull the nucleus forward, (ii) the rear cortex, whose contraction pushes the nucleus from behind (“Rear”), (iii) the front cortex at the leading edge of the cell, which may retain pressure in the front compartment of the cell that could inhibit nuclear transit (“Front”), (iv) both cortexes simultaneously to compare compartmentalized pressure in the front and rear of the cell body (“Both”), and (v) non-ablated cells to control for spontaneous movement of the nucleus during

experiments (**Fig. 3.4A**). If contraction of the rear cortex pushes the nucleus forward, then ablation of the rear cortex during nuclear transit is expected to result in the nucleus falling backwards (**Supp. Fig. 3.6C**). On the other hand, if the nucleus is pulled forward by actomyosin fibers at the leading edge of the nucleus, as has been previously shown in MEFs (Davidson et al., 2020), then ablation at the nuclear front should result in the nucleus moving backwards (**Supp. Fig. 3.6C**). In contrast, ablation of the front cortex, which may inhibit forward movement of the nucleus through maintaining increased pressure in the front compartment of the cell (Petrie et al., 2014), is expected to result in forward movement of the nucleus (**Supp. Fig. 3.6C**). In all cases, movement of the nucleus in response to laser ablation is expected to occur almost instantaneously, as ablation should immediately disrupt the balance of forces acting on the nucleus, and nuclear movement will only be resisted by viscous forces within the cytoplasm (in the case of rearward movement) or the resistance of microfluidic constrictions (in the case of forward movement).

As seen in previous studies (Charras et al., 2005; Mistriotis et al., 2019; Tinevez et al., 2009), ablation of the cell cortex caused the formation of a large plasma membrane bleb, indicating the release of cytosolic pressure (**Fig. 3.4B, Arrow**). Ablation of the rear cortex and formation of the bleb at the cell posterior led to transient rearward movement of the cell nucleus (**Fig. 3.4B-D**). This observation supports our hypothesis that contraction of the rear cortex pushes the nucleus from behind by increasing intracellular pressure in the rear compartment. Furthermore, recovery and contraction of the bleb within a minute of the initial laser ablation resulted in forward movement

of the nucleus (**Fig. 3.4B-D**), indicating that restoration of the cell rear cortex increased intracellular pressure in the back of the cell and pushed the nucleus forward.

Following ablation of the front cortex of cells, the nucleus moved forwards, suggesting that prior to ablation, pressure in the front compartment of the cell impeded forward movement of the nucleus (**Fig. 3.4 C-D, Supp. Fig. 3.6A**). However, the magnitude of the nuclear forward movement was less than the rearward movement observed when ablating the rear cortex, suggesting that pressure in the rear compartment may be greater than the pressure in the front compartment (**Fig. 3.4 C-D**). To directly assess whether the that pressure is greater in the rear compartment of the cell than in the front compartment, we ablated both front and rear cortexes of the cell simultaneously (**Fig. 3.4 C-D**). Ablation of both cortexes led to a rearward shift of the nucleus, confirming that the pushing force generated by the pressure from the rear cortex contraction was greater than the resisting force generated by pressure from the front compartment (**Fig. 3.4 C-D**).

As an additional means of comparing pressure between the front and rear compartments of the cell, we measured the size of blebs in the cell cortex formed as a result of cortex ablation (**Fig. 3.4E**). Previous work had demonstrated that bleb size following laser ablation increases as a consequence of elevated intracellular pressure, and is limited only by the elasticity of the cell membrane (Tinevez et al., 2009). Thus, increased bleb sizes following laser ablation indicate increased intracellular pressure prior to ablation. Following simultaneous ablation of the front and rear cortexes, blebs

formed in the rear compartment were significantly larger than blebs in the front compartment, indicating that pressure in the rear of the cell is greater than pressure in the front compartment (**Fig. 3.4E**). Collectively, these findings confirm that increased pressure at the cell rear helps to push the nucleus forward through constrictions.

Ablation directly in front of the nucleus led to a subtle rearward shift of the nucleus, suggesting the presence of pulling forces at the leading edge of the nucleus (**Fig. 3.4 B-C, Supp. Fig. 3.6A**), consistent with previous findings (Davidson et al., 2020). However, the rearward movement of the nucleus was very modest in comparison to the movement following rear cortex ablation (**Fig. 3.4D**). These findings indicate that the cortex-driven cells may rely more heavily on pushing forces from behind the nucleus, than on pulling forces at the nuclear front, which is also consistent with the faster nuclear transit in the cells using the cortex-driven mechanism.

We hypothesized that these intracellular pressure-driven pushing forces resulted from the accumulation and contraction of actomyosin in the rear cortex during cortex-driven nuclear transit. As we observed that ROCK-inhibition reduced myosin accumulation in the rear cortex, we hypothesized that ROCK inhibition would reduce intracellular pressure behind the nucleus. Following Y27632 treatment, nuclear movement following rear cortex ablation was reduced, whereas nuclear shift in response to ablation of the nuclear front was unaffected (**Fig. 3.4D**), indicating that pushing forces between the rear cortex and nucleus result from ROCK-dependent actomyosin contractility. Additionally, ROCK inhibition led to a substantial decrease in the size of

blebs formed following laser ablation (**Fig. 3.4E**), further confirming that ROCK mediated actomyosin contractility drives contraction of the rear cortex and increased cytosolic pressure in the rear compartment of the cell.

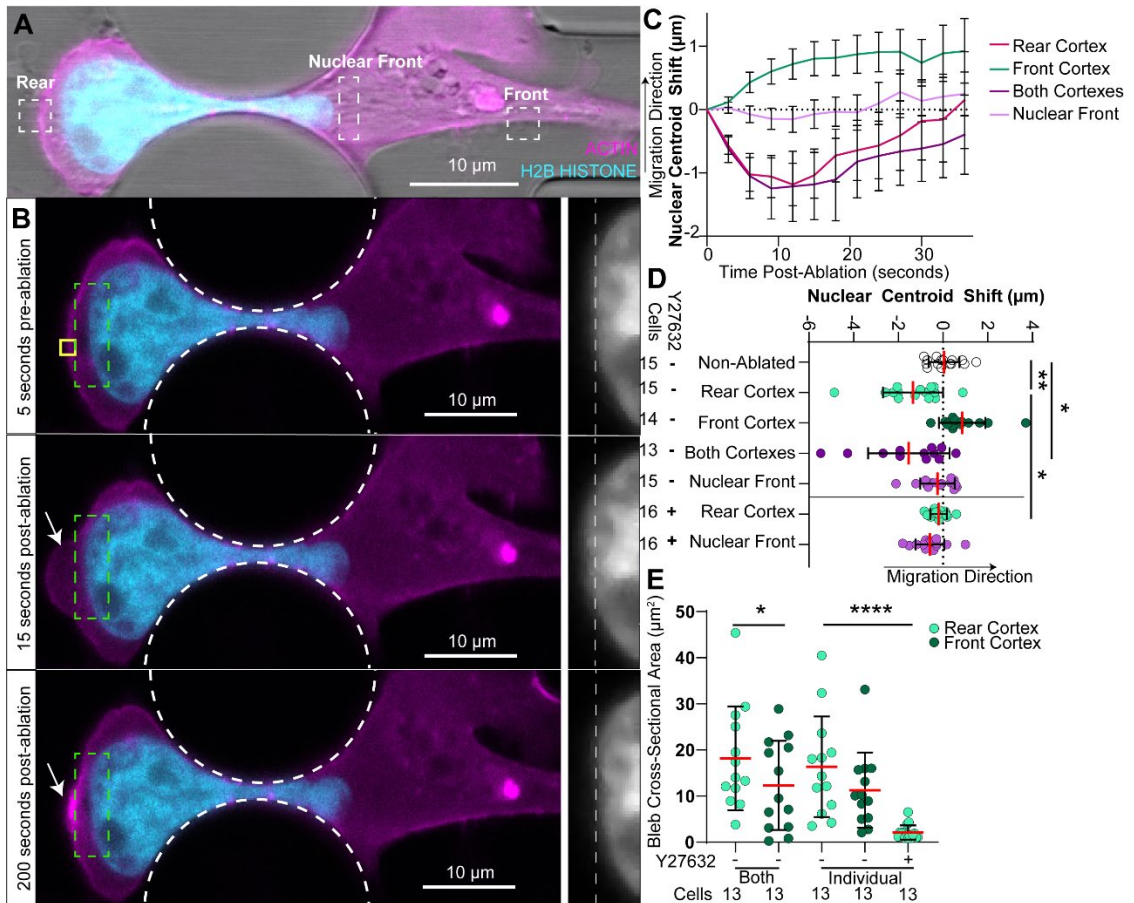
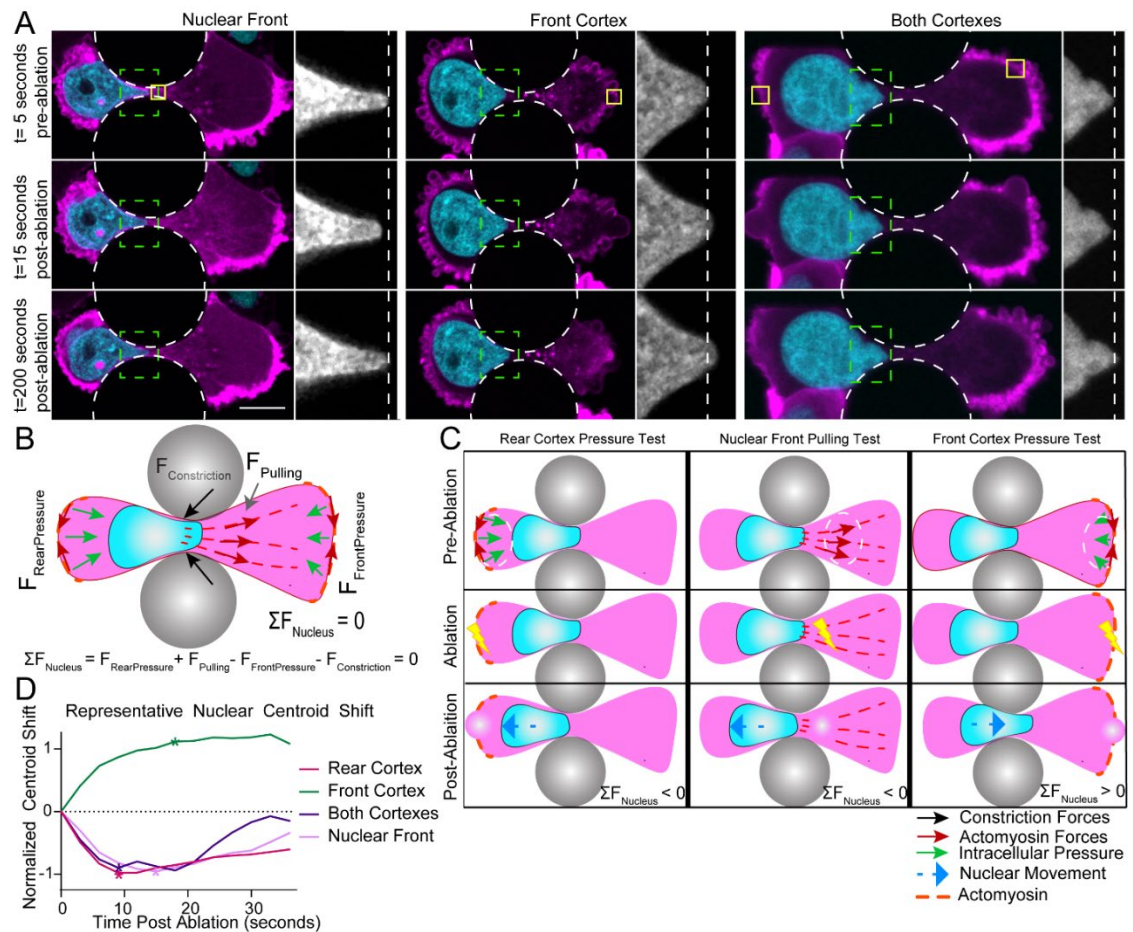


Figure 3.4. Nuclear movement following laser ablation of local actin cytoskeleton reveals that cortex-driven nuclear transit results from increased pressure in the rear compartment. (A) Laser ablation set-up. Dashed boxes represent regions targeted for laser ablation in cells starting to undergo nuclear transit through a small ($\leq 2 \times 5 \mu\text{m}^2$) constriction. Cells stably express mNeonGreen-H2B and mCherry actin-chromobody to visualize nuclear movement and actin cytoskeleton, respectively. (B) Representative time lapse series of cell ablated at the rear cortex. Yellow box represents laser ablation target. Arrow shows plasma membrane bleb formation post-ablation. Dashed green box corresponds with inlay of mNeonGreen-H2B Histone signal on right. In inlay region: dashed white line represents starting point of leading edge of nucleus. (C) Trace of nuclear centroid shift following laser ablation. Error bars represent mean \pm SEM, based on 13-16 cells per condition. (D)

Quantification of peak nuclear centroid shift immediately following nuclear ablation. Red line represents mean, black error bars represent standard deviation. *, $p < 0.05$, **, $p < 0.01$ based on unpaired non-parametric Kruskal Wallis test. (E) Cross-sectional area of blebs formed after cortex ablation. *, $p < 0.05$ for paired non-parametric Wilcoxon test. ****, $p < 0.0001$ based on unpaired non-parametric Kruskal-Wallis test. Cell counts per condition shown below graph. Red lines represent mean, black error bars represent standard deviation.



Supplementary Figure 3.6. Nuclear movement following laser ablation of specific cytoskeletal regions reveals intracellular forces acting on the nucleus during confined migration. (A) Representative time-lapse sequences of laser ablation experiments for each test

group (Nuclear Front, Front Cortex, and Both Cortices). Yellow box represents region targeted by laser ablation. Dashed white circles represent constrictions. Dashed green box corresponds with inlay of mNeonGreen-H2B Histone signal on right. In inlay region: dashed white line represents starting point of leading edge of nucleus. **(B)** Schematic illustration of forces acting on the nucleus in equilibrium during movement through a constriction. $F_{RearPressure}$ and $F_{Pulling}$ support forward movement of the nucleus, whereas $F_{FrontPressure}$ and $F_{Constriction}$ resist forward movement of the nucleus. While the nucleus is stuck within the constriction, and thus has zero acceleration, the sum of forces acting on the nucleus are zero. If the sum of forces exceeds zero, the nucleus will move forward, if the sum of forces falls below zero, the nucleus will move backward. Green arrows represent forces resulting from intracellular pressure generated by the front and rear cortex. Red arrows represent actomyosin forces. Dotted orange lines represent actomyosin fibers **(C)** Schematic illustration of laser ablation experiment. The laser ablation target regions for each hypothesis to be tested are noted by dashed white circle. The sum of forces acting on the nucleus are assumed to be in equilibrium as the nucleus is stuck in constriction. By eliminating a subset of these forces, the balance of forward and rearward forces is disrupted, and the nucleus will then move in the direction of the removed forces, following the explanation provided for (B). Blue arrow represents predicted movement of the nucleus following ablation of the specified region. **(D)** Representative trace of nuclear centroid position over time following laser ablation at each target region. Initial nuclear movement occurs in response to ablation, whereas the subsequent return to the initial position and further advancement shows recovery of actin structures after ablation. Asterisks mark measurement point of peak nuclear shift used for comparison.

Discussion

In this study, we investigated the cytoskeletal dynamics and intracellular forces acting on the nucleus as cells migrate through confined spaces. We identified a novel mechanism by which contraction of actomyosin at the rear cortex pushes the nucleus through constrictions during 3D migration. Our results suggest that cortex-driven nuclear transit is a distinct mechanism from alternative “non-cortex-driven” mechanisms, which have been previously described (Davidson et al., 2020; Petrie et al., 2014). In the cortex-driven nuclear transit mechanism, pushing forces at the cell rear are generated through contraction of actomyosin in the posterior cortex, which elevates cytosolic pressure behind the nucleus to push the nucleus forwards (**Fig. 3.5**). This lies in contrast to “non-cortex-driven” modes, in which pulling forces, through actomyosin or intermediate filaments, are mediated through physical connections between the nucleus and cytoskeleton (Davidson et al., 2020; Petrie et al., 2014; Thomas et al., 2015) (**Fig. 3.5**). Our studies suggest that some cell lines are able to use both mechanisms to achieve nuclear transit, though individual cell lines may have a propensity to use one mechanism over another. It is still not clear whether these pushing and pulling mechanisms work independently to accomplish nuclear transit, or whether they act complementarily.

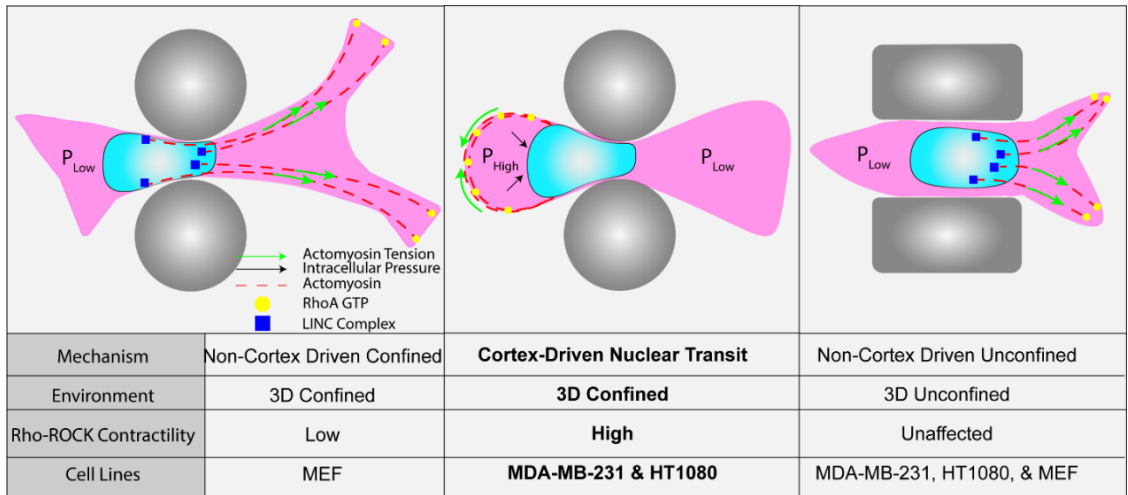


Figure 3.5: Model of alternate mechanisms of nuclear transit through constrictions.

Pushing forces are generated through contraction of the posterior cortex, caused by co-localization of active RhoA, Myosin II, and Actin. Co-localization of these same proteins at the leading edge of the nucleus can generate pulling forces at the front of the nucleus, mediated through the LINC complex.

Mirroring our findings in microfluidic devices and collagen matrices, accumulation of actomyosin in the rear of cells migrating in 3D has been observed in MDA-MB-231 cells invading through Matrigel (Poincloux et al., 2011) and in vitro models of transendothelial migration (Chen et al. 2016), indicating that cortex-driven nuclear transit may play an important role in these physiological processes. Earlier studies of 3D dendritic cell migration reported that retraction of the cell rear preceded nuclear squeezing through constrictions (Lämmermann et al., 2008). These studies showed that inhibition of contractility through treatment with blebbistatin and Y27632 delayed contraction of the cell posterior, which corresponded with a reduced migration rate in confined environments (Lämmermann et al., 2008; Schaar and McConnell, 2005).

However, it was unclear whether this retraction represented a direct transmission of force between the rear cortex and the nucleus, or whether rear retraction followed the forward movement of the nucleus. More recent findings have found elevated RhoA activity and myosin at the rear of cells migrating through 3D channels and showed evidence that this resulted in increased intracellular pressure behind the nucleus (Mistriotis et al., 2019). However, these studies did not address how intracellular pressure could contribute to nuclear transit through constrictions. Our results build upon these prior findings by confirming that retraction of the rear cortex pushes the nucleus forward during nuclear transit, and by demonstrating a functional role for cortex-driven pressure generation in confined 3D migration.

Our findings compliment prior studies which have probed intracellular forces acting on the nucleus during cell migration. One such set of studies evaluated the role of pulling forces at the front of the nucleus, which increase intracellular pressure in the front compartment of fibroblasts and HT1080 cells migrating through 3D environments (Petrie et al., 2016, 2014). In contrast with our work, these studies used a probe to directly measure intracellular pressure in cells migrating through 3D cell-derived matrix. They found that actomyosin and intermediate filaments at the nuclear front pulled the nucleus forward to increase pressure at the leading edge of cells, which generated “lobopodia” to enable invasion through 3D environments. However, subsequent studies in mesenchymal stem cells migrating in 3D alginate hydrogels have indicated that pulling forces at the leading edge of the nucleus are not necessary for the formation of lobopodia (Lee et al., 2021). In the absence of nesprins, the

nucleus was still able to move forward into constrictions to pressurize the front compartment of cells, while the authors noted an accumulation of pMLC in the rear cortex. These results mirror our findings of active RhoA and pMLC in the rear cortex during nuclear entry to constrictions, supporting the idea that elevated pressure at the cell rear is increased at the beginning of nuclear transit.

One limitation of our studies is that our detection of intracellular forces must be inferred from protein localization and changes in nuclear position following laser ablation, rather than measuring these forces directly, as the PDMS enclosure of the microfluidic migration devices prevents direct access to the migrating cells. Our laser ablation assay is limited as an indirect measurement of intracellular pressure (or other cytoskeletal forces), as it only reveals forces acting on the nucleus at a single point in time, though the pressure throughout the cell body during nuclear transit may be highly dynamic as the nucleus shifts from the rear compartment of the cell to the front compartment. Additionally, the laser ablation likely disrupts not only actomyosin but also other force-generating cytoskeletal structures within the target region, including intermediate filaments and microtubules, which could further contribute to the force transmission and force generation. Nonetheless, as we found that the cortex-driven mechanism strongly depends on the Rho-ROCK-myosin pathway, we believe that this mechanism principally depends on actomyosin activity, though our results cannot rule out potential contributions of other cytoskeletal elements, which have previously been implicated in nuclear movement (Petrie et al., 2014; Tsai et al., 2010).

A recent report demonstrated the role of pulling forces in mediating nuclear transit in MEFs (Davidson et al., 2020). Similar to our results in MDA-MB-231 cells, the authors demonstrated that ROCK inhibition increase nuclear transit times of MEFs migrating through narrow constrictions, but not through unconfined 3D channels (Davidson et al., 2020). Using a laser ablation assay, as we have used here, they found that ablation in front of the nucleus caused a rearward shift in the nucleus whereas ablation at the cell rear had no effect on nuclear movement. They also found that the rearward shift in nuclear position following ablation at the nuclear front was dependent on connections between the nucleus and cytoskeleton. These results contrast with our own, as we detected almost no nuclear shift following ablation of the nuclear front, a significant rearward shift of the nucleus after rear cortex ablation, and LINC complex disruption did not impede nuclear transit (**Supp. Fig. 3.3**). This difference in results could be attributable to our findings that MEFs scarcely use the cortex-driven nuclear transit mechanism in comparison to MDA-MB-231s, which very frequently used the cortex-driven mode. These two findings are complimentary in that they highlight a key difference between MEFs, which in the “non-cortex-driven” mode apply pulling forces at the front of the nucleus (Davidson et al., 2020), and cortex-driven MDA-MB-231 cells which push the nucleus from behind through intracellular pressure generated by the rear cortex.

While we have noted a cell-type specific preference towards the cortex-driven mechanism, and that the mechanism depends on high Rho-ROCK-mediated contractility, it remains unclear what causes cells to use a particular mechanism in a

given situation. As others have found that pulling forces at the front of the nucleus depend on the LINC complex (Davidson et al., 2014; Petrie et al., 2016), it is possible that the cortex-driven mechanism could compensate for a lack of pulling forces in specific scenarios. For example, pulling forces at the leading edge of the cell require adhesions to the surrounding environment. Thus, cells that migrate in an adhesion-independent “amoeboid” migration mode may require cortex-driven forces for nuclear transit through narrow constrictions, or cells may benefit from an additional ‘boost’ from the cortex-driven pressure when pulling forces are insufficient to move the nucleus through a constriction. Future studies will be necessary to determine the specific factors determining the selection of a particular migration mechanism, and whether this is an active decision-making process requiring specific signaling pathways, or whether cells use multiple migration modes in parallel, with a specific mode dominating depending on the particular microenvironment.

Methods

Cell Culture

MDA-MB-231 metastatic breast adenocarcinoma cells were purchased from American Type Culture Collection (ATCC); HT1080 fibrosarcoma cells were a gift from Peter Friedl and Katarina Wolf, originally purchased from DSMZ in Braunschweig, Germany; MEFs expressing GFP-Nesprin-2 were a gift from Cecile Sykes; MDA-MB-231 cells expressing the RhoA-FRET biosensor were a gift from Louis Hodgson. All cell lines were cultured in Dulbecco’s Modified Eagle Medium (DMEM) supplemented with 10% (v/v) fetal bovine serum (FBS, Seradigm VWR), and

penicillin and streptomycin (50 U/mL, ThermoFisher Scientific) and were maintained at 37°C and 5% CO₂. Cell lines were modified to express fluorescently tagged proteins using lentiviral vectors (pCDH-mCherry2-Actin Chromobody-puro and pCDH-mNeonGreen-H2B Histone-puro). Transient expression of CMV-GFP-NMHC-IIA (Addgene #11347) and mCherry-MyosinIIB-N-18 (Addgene #55107) was achieved using a Nucleofector II electroporator and the Cell Line Nucleofector Kit V (Lonza Biosciences). MEF were modified using BFP and DN-KASH expression plasmids in a doxycycline-inducible Piggybac plasmid backbone (Addgene #s Not Yet Available). Cell lines were tested for mycoplasma infection following completion of experiments. Human cell lines were verified through the ATCC Cell Line Authentication Service.

Viral and Piggybac Modification

Pseudoviral particles were produced using 293TN cells (System Biosciences, SBI) were transfected with the lentiviral plasmid of interest as well as lentiviral packaging and envelope plasmids (psPAX and pMD2.G, gifts from Didier Trono) using PureFection transfection reagent (SBI), per manufacturer's protocol. Supernatants were collected at 48, 72, and 96 hour intervals post-transfection and were passed through a 0.45 µm filter. Cells to be transduced were cultured for 24 hours prior to transduction at a confluency of 50% and were then cultured in lentivirus-containing media with polybrene (8 µg/mL). Lentivirus containing media was removed after 24 hours, and following an additional 24 hours of recovery time, cells were selected using 1 µg/mL of puromycin (Invivogen) for 3 days. For Piggybac modifications, MEFs

were seeded into 6-well plates and were transfected with 1.75 μg of Piggybac plasmids and 0.75 μg of a hyperactive transposase using PureFection Transfection reagent (SBI), per manufacturer's protocol. Transfected cells were selected using 800 $\mu\text{g}/\text{mL}$ G418 for 3 days. Cells were sorted using flow assisted cell sorting (FACS) in order to obtain consistent expression levels.

Microfluidic Device Preparation

Microfluidic devices were prepared as previously described (Davidson et al., 2015; Keys et al., 2018). Briefly, microfluidic devices were made through soft lithography by curing polydimethylsiloxane (PDMS) in a plastic mold containing microfluidic features at 65C for 2 hours. After removing cured PDMS from the mold, PDMS features were cut out using biopsy punches, and then both PDMS devices and glass coverslips were washed with deionized water and isopropyl alcohol, and then treated in a plasma cleaner (Harrick Plasma) for 5 minutes. PDMS pieces were then bound to activated coverslips and then heated at 95C on a hotplate for 1 minute to improve adhesion. After heating, devices were filled with 70% ethanol to sterilize internal surfaces, rinsed with PBS, and then coated with extracellular matrix proteins. For MDA-MB-231 cells, devices were coated with 50 $\mu\text{g}/\text{mL}$ type-I rat tail collagen (Corning) in 0.02 N glacial acetic acid overnight at 4°C. For MEFs and HT1080 cells, devices were coated with 50 $\mu\text{g}/\text{mL}$ fibronectin (Millipore) in PBS overnight at 4°C. Before seeding with cells, devices were rinsed once with PBS and once with cell media. Devices were then aspirated of all media, and then loaded with cell-containing solution (roughly 20,000-30,000 cells per chamber). In devices, cells were cultured in

Fluorobrite DMEM supplemented with 10% FBS (Seradigm, VWR), pen/strep (50 U/mL, ThermoFisher), GlutaMAX, and 10 mM HEPES (Gibco). Cells were allowed to attach within devices for 8-12 hours before live cell imaging. Cells were imaged for 12-14 hours at 3-to-5-minute intervals on a Zeiss LSM700 laser scanning confocal microscope at 37°C.

Collagen Matrix Cell Migration Assay

Collagen matrix cell migration assays were performed as previously described (Cross et al., 2010). In brief, PDMS wells were formed by punching out 10 mm diameter holes from PDMS slices. PDMS and glass coverslips were treated in a plasma cleaner for 5 minutes, before bonding PDMS to treated glass slides on a 95°C hot plate for 3 minutes. Wells were coated with 1% PIE for 10 minutes, followed by 0.1% Glutaraldehyde for 30 minutes, and then subsequently washed with PBS once, and cell media once, before adding the collagen solution. Collagen matrices were prepared by mixing Type I rat tail collagen (Corning) with DMEM and NaOH (to reach a neutral pH of 7.4) with a solution of cells suspended in complete DMEM to achieve a final density of 80,000 cells/mL. Small volumes of collagen solution (10-15 μ L) were pipetted into the middle of wells, where they were allowed to polymerize at 37°C for 30 minutes. Following polymerization, wells were filled with complete DMEM and were subsequently incubated at 37°C for 48 hours before imaging experiments.

Laser Ablation of Actin

Cells were seeded into migration devices 12-16 hours before ablation experiments. Cells were maintained at 37C in Fluorobrite DMEM containing 10% FBS, 10 mM HEPES (Gibco), GlutaMax, and penicillin and streptomycin (50 U/mL). *Imaging data was acquired through the Cornell Institute of Biotechnology's BRC Imaging Facility with NYSTEM C029155 and NIH S10OD018516 funding for the Zeiss LSM880 inverted confocal microscope. Cells were imaged through a water immersion 40×/NA 1.1 objective (Carl Zeiss Imaging) using 488-nm and 561-nm laser lines. Cells were imaged at 3 second intervals for 63 frames. After 9 seconds, cells were ablated in defined regions using a 780 nm laser produced by a Spectra Physics Insight multiphoton excitation source. Ablation was performed at 40-70% attenuation, following ablation tests at the beginning of each experiment to verify that the laser successfully disrupted the actin cytoskeleton without causing cell death. Cells which exited the constriction, displayed rapid blebbing, or appeared to die following laser ablation were excluded from analysis, while cells which were able to recover following disruption of the actin network were included.*

Image Analysis of Laser Ablation Experiments

Tracking of nuclear movement following laser ablation was achieved using ImageJ/FIJI software and a custom MATLAB script. Briefly, the image channel containing the fluorescent mNeonGreen-H2B Histone signal was processed using a 3-pixel median filter to eliminate noise, and then a binary mask of this signal was generated using ImageJ/FIJI's built-in RenyiEntropy masking function. This binary mask was then processed in MATLAB to track the position of the nucleus' centroid at

each time point. The furthest position of nuclear movement prior to recovery (within 20 seconds of the initial ablation) was considered as the direct result of force disruption as a consequence of laser ablation and was recorded as the peak centroid shift (**Supp. Fig. 3.6D**). Bleb area measurements were performed in ImageJ/FIJI at the time point when the bleb had reached its maximum size. Outer bleb perimeter was traced manually, and inner bleb perimeter was traced at the periphery of the cell at the time point immediately prior to laser ablation.

RhoA FRET Imaging and Analysis

Analysis of RhoA-FRET biosensors was performed as described previously (Cheung et al., 2022). Cells were imaged at regular intervals on a dual channel image acquisition set-up to minimize temporal and spatial misalignment problems which impair FRET result interpretation. Cells were imaged at 5-minute intervals for 12 to 16 hours. Cells were excited with a ET436/20× (CFP Excitation) source for an exposure time of 3 seconds with CFP excitation while CFP and YFP (“FRET”) emission channels were captured simultaneously, by using a W-View Gemini beam splitter (A12801-01, Hamamatsu Photonics) and a T505lpxr dichroic mirror, through ET480/40m and ET535/30m optical filters, respectively. The light source for fluorescence imaging was a xenon arc lamp (Lambda LB-LS/30, Sutter Instruments). An absorptive neutral density filter with OD = 0.3 (NE03B-A, ThorLabs) was used to attenuate light to minimize phototoxicity. All filters and dichroic mirrors were purchased from Chroma Technology. Prior to each experiment, the x-y positions of CFP and FRET channels were adjusted using the W-VIEW Adjustment software

(Hamamatsu Photonics) to achieve a reasonable alignment for easier image registration and processing. The epifluorescence microscope was surrounded by an incubator with a temperature of 37°C, 5% CO₂, and humidity of ~70%.

Field alignment, flatfield correction, and background subtraction were performed as previously described.(Cheung et al., 2022) Images of cells were then manually masked by tracing the outline of cells using the CFP channel in FIJI/ImageJ. Following these corrections to both the CFP and FRET channels, FRET ratios were calculated by dividing the FRET channel by the CFP channel. The sensitivity of the RhoA-FRET biosensor expressed in this MDA-MB-231 cell line to RhoA activation and inactivation was performed under identical experimental conditions on this imaging set-up as described previously (Cheung et al., 2022). Local FRET ratios were then calculated by manually tracing regions as defined in Supp. Fig. 3.5A.

Analysis of Migration Mode and Nuclear Transit Times

Measurements of nuclear transit times were performed as described previously (Davidson et al., 2015). Briefly, cells were imaged at 5-minute intervals on a Zeiss LSM710 laser scanning confocal microscope using 488-nm and 561-nm laser lines as they migrated through migration devices over a period of 12-16 hours. A fluorescent marker of the nucleus (either mNeonGreen-H2B Histone, or GFP-Nesprin2) was used to track the position of the nucleus relative to microfluidic constrictions. An imaginary line 5 microns was marked on either side of the middle of the constriction, to define when the nucleus “enters” and “exits” the constriction. The times at which the nucleus

enters and passes through the constriction were noted, and this interval was recorded as the nuclear transit time. Cells which did not complete nuclear transit following entry to the constriction were excluded from analysis.

Immunofluorescence Imaging

Cells were fixed in PDMS microfluidic devices using a solution of 4% Paraformaldehyde on ice for 10 minutes, washed twice with PBS for 5 minutes, permeabilized with 0.2% Triton in PBS at room temperature, blocked with a solution of Bovine Serum Albumin (3% v/v) with 0.05% Tween and 0.2% Triton in PBS for 1 hour, and then treated with primary antibodies (anti-pMLC, cell signaling 1:100) in blocking solution overnight at 4°C. Cells were then washed 3 times with PBS for 10 minutes each, and then treated with Secondary Antibodies (Alexa Fluor 488 anti-Rabbit), Phalloidin 647 (1:400 dilution), and Hoechst (1:5000 dilution) for 2 hours at room temperature. Cells were washed 3 times with PBS for 10 minutes each. Devices were filled with blocking solution and sealed with glass coverslips prior to imaging.

Statistical Analysis

All experimental data are based on at least three independent experiments, unless otherwise specified. Statistics tests were performed and graphs were created using GraphPad Prism (GraphPad Software, San Diego, USA). Nuclear transit times were compared using a one-way ANOVA. Frequency of nuclear transit mechanism selection was performed using a Chi Squared test of independence. Changes in local FRET ratio during nuclear transit were evaluated using a paired non-parametric

ANOVA test (Wilcoxon). Nuclear centroid shifts following laser ablation were compared using an unpaired non-parametric ANOVA test (Kruskal-Wallis). Bleb formation in cells ablated at a single site were compared using an unpaired non-parametric ANOVA test (Kruskal-Wallis) while bleb formation in cells ablated at both cortexes simultaneously were compared using a paired non-parametric ANOVA test (Wilcoxon).

Acknowledgements

We thank Louis Hodgson for providing the MDA-MB-231 cell line expressing the RhoA-FRET Biosensor, Patricia Davidson for providing the Mouse Embryonic Fibroblast Cell Line expressing Nesprin-2 GFP, and Peter Friedl and Katarina Wolf for providing the HT1080 fibrosarcoma cell line. We thank Klaus Hahn and Louis Hodgson for their advice regarding the use and analysis of FRET biosensors in migrating cells. We thank Philipp Isermann for his help in setting up the initial laser ablation experiments on MDA-MB-231 cells.

Competing Interests

The authors declare no competing interests. Jan Lammerding has received consulting fees from BridgeBio on unrelated projects.

Funding

We acknowledge the support of NYSTEM C029155 and NIH S10OD018516 grants and the help of the Cornell Institute of Biotechnology's BRC Imaging Facility (RRID:SCR_021741) for the use of the Zeiss LSM880 inverted confocal microscope. We thank the Biotechnology Resource Center Flow Cytometry Facility (RRID:SCR_021740) for help with Flow Assisted Cell Sorting. This work was performed in part at the Cornell NanoScale Science & Technology Facility, a member of the National Nanotechnology Coordinated Infrastructure, which is supported by the National Science Foundation (award NNCI-2025233). This work was supported by awards from the National Institutes of Health (R01 HL082792, R01 GM137605, U54 CA210184 to J.L.,) the Department of Defense Breast Cancer Research Program (Breakthrough Award BC150580 to J.L.), the National Science Foundation (CAREER Award CBET-1254846 and URoL-2022048 to J.L.), the Volkswagen Stiftung (A130142 to J.L.), and the Knight@KIC Engineering Graduate Fellowship (to J.K.). The content of this manuscript is solely the responsibility of the authors and does not necessarily represent the official views of the National Institutes of Health.

CHAPTER 4- PRESSURE IN THE POSTERIOR COMPARTMENT OF MIGRATING CELLS INDUCES NUCLEAR INFLUX³

Abstract

Cells migrate in vivo through complex confining microenvironments, which induce significant nuclear deformation that may lead to nuclear blebbing and nuclear envelope rupture. While actomyosin contractility has been implicated in regulating nuclear envelope integrity, the exact mechanism remains unknown. In collaboration with the Konstantopoulos lab at Johns Hopkins University, we argue that confinement-induced activation of RhoA/ myosin-II contractility, coupled with LINC complex-dependent nuclear anchoring at the cell posterior, locally increases cytoplasmic pressure and promotes passive influx of cytoplasmic constituents into the nucleus without altering nuclear efflux. The Konstantopoulos group observed nuclear influx using a photoactivatable, cytoplasmic GFP, which flowed into the nucleus during confined migration. Elevated nuclear influx is accompanied by nuclear volume expansion, blebbing, and rupture, ultimately resulting in reduced cell motility. Through laser ablation of the rear cortex, we revealed that this nuclear influx depends on contraction of the cell rear and increased intracellular pressure in the rear

³ Portions of this section have been adapted from the following publication
Mistriotis P, Wisniewski EO, Bera K, **Keys JT**, Li Y, Tuntithavornwat S, Law RA, Perez-Gonzalez NA, Erdogmus E, Zhang Y, Zhao R, Sun SX, Kalab P, Lammerding J, Konstantopoulos K (2019) Confinement hinders motility by inducing RhoA-mediated nuclear influx, volume expansion, and blebbing. *Journal of Cell Biology*. 218(12):4093-4111

Contributions: This work was primarily performed in the Konstantopoulos laboratory by members of the Konstantopoulos group; JT Keys performed laser ablation experiments and aided in their interpretation; he also trained E Wisniewski and P Mistriotis in the use of microfluidic devices designed in the Lammerding lab (described in Chapter 2) during their week-long research stay in the Lammerding lab. JT Keys also contributed to the editing of the final manuscript.

compartment of the cell. Cumulatively, confinement regulates nuclear size, nuclear integrity, and cell motility by perturbing nuclear flux homeostasis via a RhoA-dependent pathway.

Introduction

Cell migration through tissues is a critical step during the metastatic spread of cancerous cells from primary tumors to distal organs in the body. Metastasizing cells must travel through heterogeneous confining microenvironments in vivo that impose physical cues and initiate intracellular signaling cascades distinct from those experienced by cells during 2D migration (Paul et al., 2017; van Helvert et al., 2018). Specifically, pores in the ECM of tumor stroma and tunnel-like migration tracks are confining topographies that cells must navigate. These tunnel-like tracks may be generated by matrix remodeling of dense ECM by macrophages, cancer-associated fibroblasts, or leader cells, but preexisting, 3D longitudinal tracks are also generated naturally by various anatomical structures (Paul et al., 2017). These paths impose varying degrees of confinement, as cells must travel through confining pores varying from 1 to 20 μm in diameter, or fiber- and channel-like tracks ranging from 3 to 30 μm in width and up to 600 μm in length (Weigelin et al., 2012). As the largest and stiffest cellular component (Lammerding, 2011), the nucleus has a rate-limiting role in cell migration through confined spaces (Davidson et al., 2014; Harada et al., 2014; Rowat et al., 2013; Wolf et al., 2013). In the absence of matrix degradation, tumor cell motility is halted at pore sizes smaller than $\sim 7 \mu\text{m}^2$ due to lack of nuclear translocation (Wolf et al., 2013). Even at larger pore sizes, the nucleus poses a

significant barrier to cell motility, and cells must transmit forces to the nucleus from the cytoskeleton in order to achieve efficient nuclear translocation (McGregor et al., 2016). One possible mechanism is through the linker of cytoskeleton and nucleoskeleton (LINC) complex, a network of SUN and nesprin proteins that mechanically connects the nucleus to the cytoskeleton (Crisp et al., 2005).

Transmission of actomyosin contractile forces to the nucleus is essential for confined migration. When myosin contractility is inhibited, migration of cancer cells through collagen gels is significantly delayed due to insufficient pushing forces at the cell rear (Thomas et al., 2015; Wolf et al., 2013). Additionally, actomyosin contractility, in conjunction with integrins and intermediate filaments, applies pulling forces to the nucleus from the cell leading edge (Petrie et al., 2014; Wolf et al., 2013).

Confinement exerts a mechanical stress on the nucleus, which can cause nuclear pressure buildup and ultimately lead to the blebbing and subsequent rupture of the nuclear envelope, resulting in DNA damage (Denais et al., 2016; Hatch & Hetzer, 2016; Shah et al., 2021; Takaki et al., 2017). Compression of the nucleus by contractile actin fibers surrounding it causes spontaneous nuclear rupture events (Hatch & Hetzer, 2016; Takaki et al., 2017). However, nuclear rupture can occur in the absence of perinuclear actin simply upon mechanical compression of cells (Hatch & Hetzer, 2016). These findings suggest that compression of the nucleus, whether by actin fibers or external forces, is the main driver for nuclear envelope rupture. Consistent with these findings, nuclear rupture occurs at sites of high nuclear curvature (Xia et al., 2018). High actomyosin contractility, which increases cell and

nuclear spreading (Buxboim et al., 2014), promotes nuclear rupture (Xia et al., 2018), while inhibition of actomyosin contractility results in more rounded nuclei with less frequent ruptures (Denais et al., 2016; Xia et al., 2018).

While several studies implicate actin and myosin in confinement-induced nuclear bleb formation and rupture (Denais et al., 2016; Hatch & Hetzer, 2016; Xia et al., 2018), it is unclear how contractile forces specifically promote this process. To address this question, we studied nuclear bleb formation by inducing HT1080 fibrosarcoma cells to migrate via chemotaxis through collagen-coated microfluidic channels with fixed dimensions of 3 μm in height, 10 μm in width, and 200 μm in length. In these confining channels, the nucleus acts as a plug, which compartmentalizes the cell posterior and anterior. We herein demonstrate that elevated and polarized RhoA/myosin-II activity induced by confinement, coupled with LINC complex-dependent anchoring of the nucleus at the cell posterior, locally increases cytoplasmic pressure and promotes passive influx of cytoplasmic constituents into the nucleus. In conjunction with deformation of the nucleus by perinuclear actomyosin bundles, this RhoA/myosin-II-dependent nuclear influx from the cell posterior promotes nuclear volume expansion, nuclear bleb formation, and subsequently nuclear envelope rupture.

Results

Confinement induces nuclear blebbing mediated by an actomyosin-dependent pathway involving the LINC complex

Using HT-1080 fibrosarcoma cells as a model, we observed that ~50–60% of cells migrating inside the physically constricted collagen-coated microchannels (width [W] \times height [H] = $10 \times 3 \mu\text{m}^2$) displayed nuclear blebs, which were identified as spherical-like bulges localized primarily at the leading edge of the nucleus (**Figure 4.1, a and b**). In light of prior work showing that compression of cells between parallel plates is sufficient to induce nuclear bleb formation (Hatch & Hetzer, 2016), we fabricated wide ($W = 50 \mu\text{m}$) microchannels with a fixed height of $3 \mu\text{m}$ to confine cells only in the apicobasal (i.e., top to bottom) direction. Although nuclear blebbing was observed in the $50\text{-}\mu\text{m}$ -wide channels, it was significantly reduced compared with the $10\text{-}\mu\text{m}$ -wide channels, which confine cells on all four sides. Nuclear blebbing was the least frequent on unconfined, 2D surfaces (**Figure 4.1, a and b**). In concert with recent findings (Denais et al., 2016; Raab et al., 2016), formation of nuclear blebs preceded or coincided with nuclear envelope rupture (**Figure 4.1 c**). Nuclear rupture induced the rapid and reversible exchange of material between the nucleus and cytoplasm, as indicated by the use of two spectrally distinct reporters: one normally localized in the nucleus (NUP50-mCherry) and the other one in the cytoplasm (NLS-MBP-GFP-NES(Rev); **Figure 4.1 d**), and was more frequent in confinement than in 2D (**Figure 4.1 e**). Of note, ~50% of cells with nuclear ruptures experienced multiple rupture/repair events at a rate of approximately one rupture per hour during migration through confined channels. In contrast, we did not detect multiple rupture events within the observation period on unconfined 2D substrates.

In light of prior work showing that both membrane bleb formation and nuclear envelope rupture require the activation of actomyosin contractility (Denais et al., 2016; Hatch & Hetzer, 2016; Sahai & Marshall, 2003), we hypothesized that formation of nuclear blebs also requires actomyosin contractility. In line with our hypothesis, inhibition of Rho-associated protein kinase (ROCK) via cell treatment with Y27632 (10 μ M; **Figure 4.1 f**), markedly suppressed nuclear blebbing in confinement, whereas expression of a constitutive active RhoA mutant (Q63L) increased nuclear blebbing (**Figure 4.1 f**). While individual knockdown of *myosin-IIA* (*MIIA* or *MYH9*) or *MIIB* (*MYH10*) had little effect on confinement-induced nuclear blebbing, dual silencing of *MIIA* and *MIIB* repressed nuclear blebbing (**Figure 4.1 g**). Myosin transmits forces to the nucleus via the LINC complex (Petrie et al., 2014). Thus, we next assessed the potential contributions of the LINC complex components SUN1 and SUN2 to nuclear blebbing in confinement. Silencing of *SUN1*, and to a lesser extent *SUN2*, reduced nuclear blebbing in confinement (**Figure 4.1 h**). Together, these results demonstrate that myosin contractility via the LINC complex regulates nuclear bleb formation.

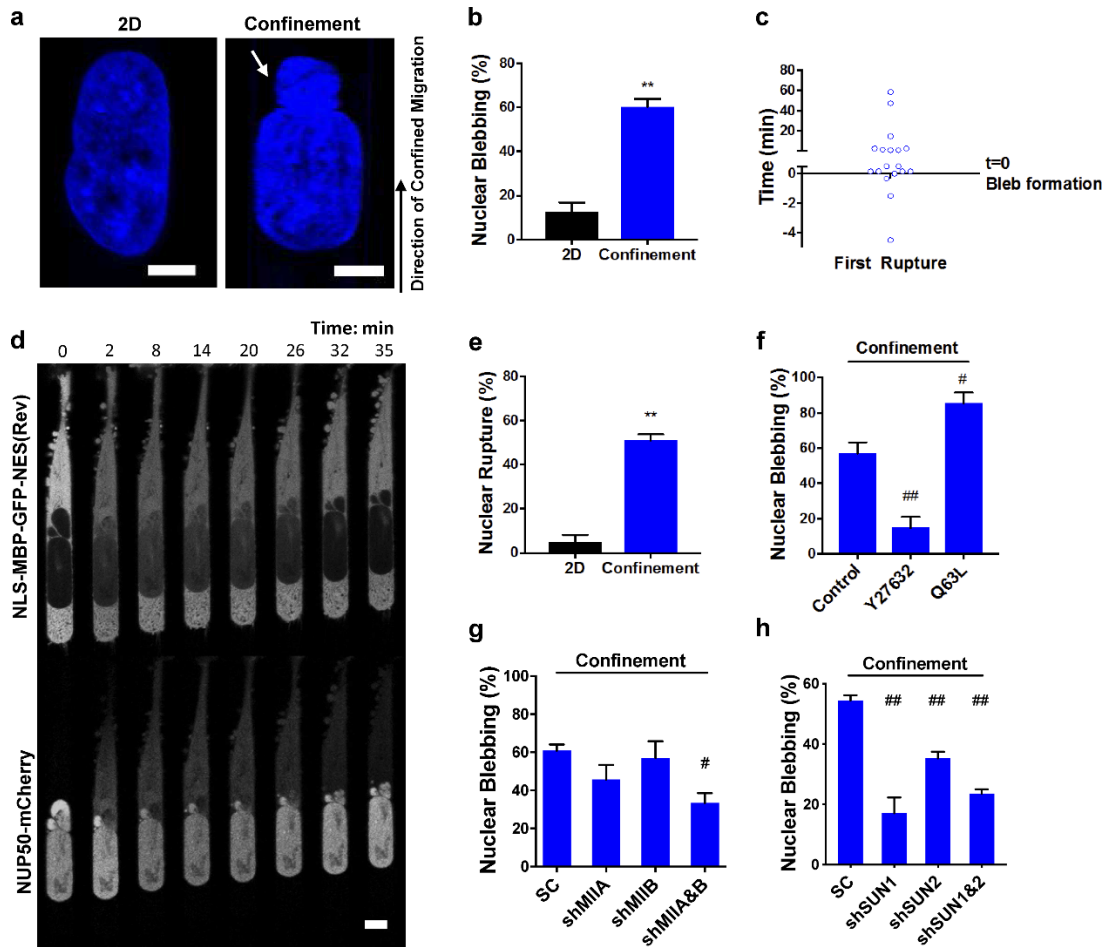


Figure 4.1: Confinement promotes nuclear blebbing and rupture via a

RhoA/ROCK/myosin-II/SUN1/2-dependent pathway. (a) Representative images of the nucleus in 2D and confinement as visualized from cells fixed and stained with Hoechst. White arrow indicates nuclear bleb. Scale bars, 5 μm . (b) Percentage of HT-1080 cells exhibiting nuclear blebbing in 2D versus confinement ($n \geq 3$ independent experiments with a minimum of 30 cells per experiment). (c) Time required for the first incident of nuclear blebbing versus nuclear rupture as observed from HT-1080 cells expressing NLS-MBP-GFP-NES(Rev) and H2B or NUP50-mCherry ($n = 3$ independent experiments with a minimum of five cells per experiment). (d) Image sequence of an HT-1080 cell experiencing transient nuclear rupture in confined channels visualized by NLS-MBP-GFP-NES(Rev) mislocalization in the nucleus and NUP50-mCherry mislocalization in the cytoplasm. Scale bar, 10 μm . (e) Percentage of HT-

1080 cells experiencing nuclear rupture in 2D and confinement, as quantified from mislocalization of NLS-MBP-GFP-NES(Rev) from the cytoplasm to the nucleus ($n = 4$ independent experiments with a minimum of eight cells per experiment). **(f)** Percentage of control, 10 μ M Y27632-treated, and constitutively active RhoA (Q63L) HT-1080 cells displaying nuclear blebbing, as observed from cells fixed and stained with Hoechst ($n \geq 3$ independent experiments with a minimum of 15 cells per experiment). **(g)** Percentage of scramble control, MIIA-knockdown, MIIB-knockdown, and dual MIIA/B-knockdown HT-1080 cells displaying nuclear blebbing, as observed from cells fixed and stained with Hoechst ($n \geq 3$ independent experiments with a minimum of 15 cells per experiment). **(h)** Percentage of scramble control, SUN1-knockdown, and/or SUN2-knockdown HT-1080 cells displaying nuclear blebbing ($n \geq 3$ independent experiments with a minimum of 15 cells per experiment). Values represent mean \pm SEM. **, $P < 0.01$ relative to 2D; #, $P < 0.05$; ##, $P < 0.01$ relative to confined control or scramble control (SC).

Confinement induces RhoA Activation, which induces nuclear blebbing by promoting passive nuclear influx through the nuclear trailing edge

In light of the involvement of the RhoA/ROCK/myosin-II pathway in nuclear blebbing, we sought to determine the mechanism by which these molecules promote nuclear bleb formation in confinement. To explore this, we first quantified RhoA activity of cells in 2D versus confinement using a Förster resonance energy transfer (FRET)-based RhoA activity biosensor (Fritz et al., 2013). Using this biosensor, RhoA activation is detected by increased FRET in the closed conformation, in which the GTP-loaded RhoA domain interacts with the rhotekin Rho-binding domain, bringing the mTFP-1 (cyan) donor and YFP acceptor closer to each other. FLIM

measurements revealed that cells in confinement exhibited overall higher levels of RhoA activity than cells in 2D (**Figure 4.2 a**). Importantly, confined cells displayed spatial regulation of RhoA, with maximal activity observed at the cell poles (**Figure 4.2, b and c**). In contrast, 2D cells had relatively uniform RhoA activity (**Figure 4.2 b**).

In light of the distinct localization of RhoA activity exhibited in confined cells as well as the role of myosin-II in nuclear bleb formation, we examined myosin-II localization in cells in confinement. First, we examined MIIA and MIIB isoforms to determine if they displayed a similar polarization pattern to RhoA activity. Interestingly, MIIA and MIIB showed the highest localization at the cell rear in $\sim 70\%$ of migrating cells (**Figure 4.2 d**). We also examined myosin-II localization around the nucleus. Using super-resolution imaging, we observed distinct MIIA fibers on the apical surface of the nucleus of confined cells (**Figure 4.2 e**). These myosin-II fibers colocalized with actin and strongly accumulated in regions of nuclear deformation, suggesting that these actomyosin bundles deformed the nucleus nonuniformly on its apical surface.

In light of this RhoA/myosin-II polarization in confinement, we hypothesized that elevated actomyosin contractility at the cell rear locally increases cytoplasmic pressure. Because the nucleus separates the posterior and anterior poles of cells in confining channels, the equilibration of differential cytoplasmic pressure throughout the cell could result in fluid flux into the nucleus. In conjunction with increased intranuclear pressure resulting from direct actomyosin compression of the nucleus

(**Figure 2 e**), this influx of cytoplasmic constituents into the nucleus could ultimately pressurize the nucleus, promoting nuclear blebbing and rupture.

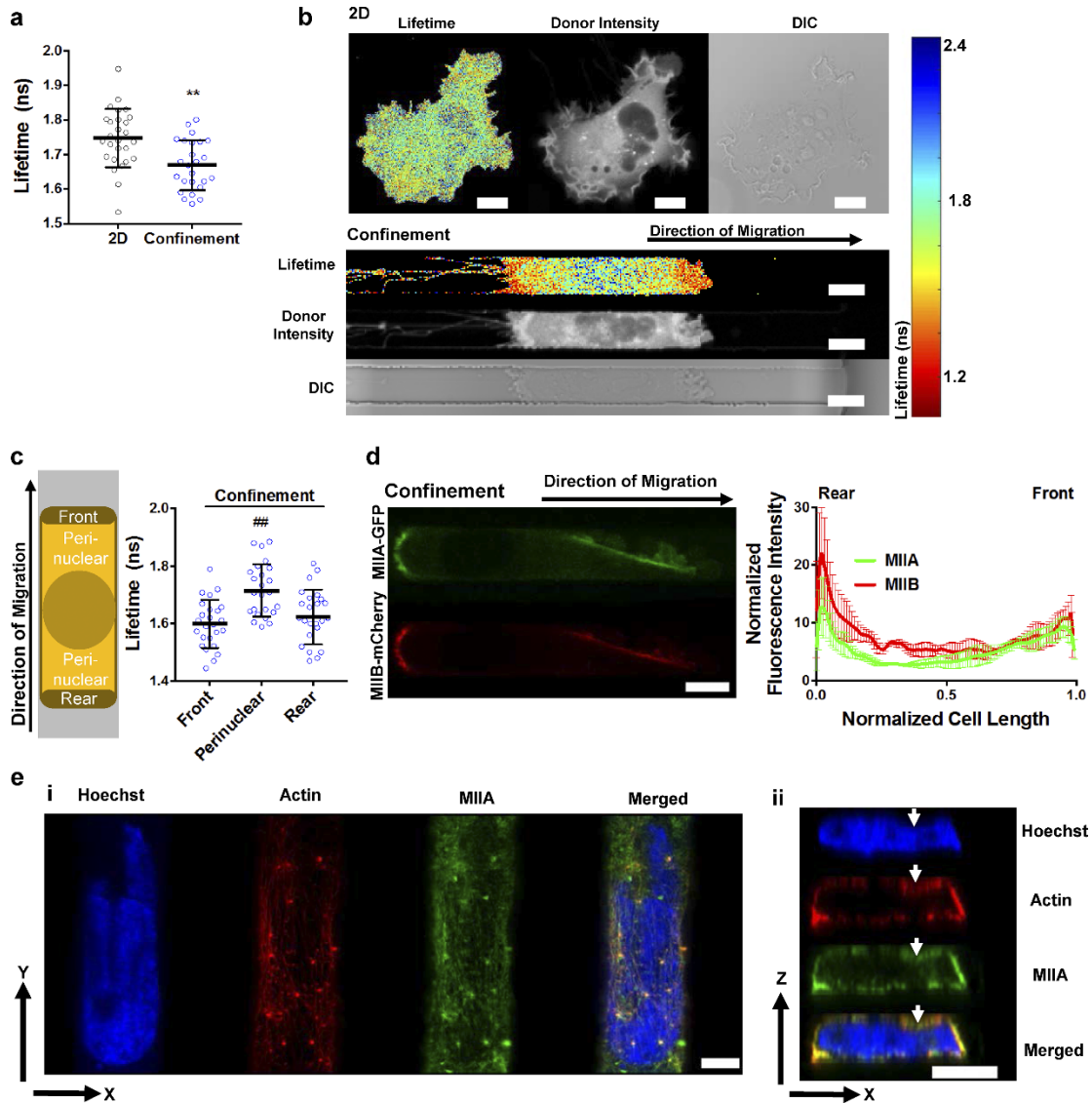


Figure 4.2: Confinement spatially regulates RhoA/myosin-II dependent contractility.

(a) Donor fluorescence lifetime of RhoA activity biosensor on 2D and in confinement, as measured by FLIM-FRET ($n \geq 25$ cells from three independent experiments). (b) Heat map of RhoA activity biosensor in representative cells on 2D or in confinement, as imaged by FLIM-FRET (scale bars, 10 μm). DIC, differential interference contrast. (c) Schematic (left) depicting the front, perinuclear, and rear cell regions and spatial distribution of RhoA activity inside confined microchannels (right) as measured by FLIM-FRET ($n \geq 25$ cells from three independent experiments). (d) Representative image (left) and quantification (right) of the

average intensity of MIIA and MIIB across the cell length of confined cells, as visualized by MIIA-GFP and MIIB-mCherry (quantification from 16 cells). Scale bar, 10 μm . (e) Super-resolution images of the perinuclear actin and myosin-IIA of a representative HT-1080 cell (out of 10 cells analyzed) expressing myosin-IIA-GFP and stained for actin phalloidin (red) and Hoechst (blue) inside a confined channel. (i) XY plane, apical surface; (ii) orthogonal view, XZ plane. Arrows indicate regions of nuclear deformation. Scale bars, 5 μm . Data represent the mean \pm SD. **, $P < 0.01$ relative to 2D; ##, $P < 0.01$ relative to confined front/rear.

Cytoplasmic pressure-driven nuclear intake, which we define as passive nuclear influx, would be feasible for molecules smaller than the estimated size exclusion limit of NPCs ($\sim 40\text{--}60$ kD; (Stewart, 2007)). To test this hypothesis, we transfected HT-1080 cells with a photoactivatable GFP construct (PA-GFP), which has a low molecular mass (~ 25 kD), is distributed throughout the cell, and becomes fluorescent only upon UV-light illumination. By locally activating PA-GFP either in the posterior or anterior cytoplasmic compartment (**Figure 4.3 a**), we monitored PA-GFP entry into the nucleus and calculated the half-time ($t_{1/2}$) of nuclear influx. Confinement induced increased passive nuclear influx selectively from the posterior compartment, as evidenced by lower $t_{1/2}$ compared with those for the anterior compartment and cells on unconfined 2D surfaces (**Figure 4.3 b**).

Interestingly, cells inside wider channels ($W \times H = 50 \times 3 \mu\text{m}^2$) displayed reduced passive nuclear influx from the posterior compared with tightly confined ($W \times H = 10 \times 3 \mu\text{m}^2$) cells (**Figure 4.3 c**). This difference can be explained by the fact that in

wider microchannels, the pressure differential is alleviated since the nucleus does not fully occlude the channels' cross-sectional area and thus pressure can be equilibrated through gaps between the nucleus and side walls of the microchannels. In contrast, in tightly confined cells, the nucleus acts as a plug, which compartmentalizes the cell posterior and anterior, thereby facilitating pressure buildup at the cell rear.

To distinguish the roles of pressure-driven convection versus diffusion of PA-GFP in nuclear influx, we applied either a hypotonic (165 mOsm) or hypertonic (620 mOsm) shock at the cell leading or trailing edge, respectively (**Figure 4.3, d and e**). Exposure to a hypotonic shock at the cell front, which drives water influx and consequently pressure buildup in the cell front compartment, increased PA-GFP nuclear influx from the cell anterior (**Figure 4.3 d**). On the other hand, exposure to a hypertonic shock at the cell rear, which has the exact opposite effect on the cell rear compartment, decreased PA-GFP nuclear influx from the cell posterior (**Figure 4.3 e**). Nuclear influx, but not efflux, increased in bleb-bearing but not bleb-free nuclei (**Figure 4.3 f**), suggesting that actomyosin contractility is required for increased passive nuclear influx. Indeed, ROCK inhibition suppressed passive nuclear influx through the trailing nuclear edge in confined cells (**Figure 4.3 f**).

To verify that actomyosin contractility promotes nuclear influx and bleb formation by increasing cytoplasmic pressure and thus forcing cytoplasmic constituents into the nucleus, we measured nuclear influx after laser ablation of the actomyosin cortex at the cell's trailing edge (**Figure 4.3, g and h**). Upon laser ablation of the rear cortex,

locally accumulated actin is disrupted, and consequently a large pressure-driven membrane bleb formed in the ablated region (**Figure 4.3 h**), thereby allowing relaxation of internal cytoplasmic pressure as previously reported (Tinevez et al., 2009). Importantly, diffuse cytoplasmic GFP stayed within the cytoplasm after ablation, indicating that laser ablation disrupted only the cortical actomyosin network while leaving the plasma membrane intact (**Figure 4.3 h**). Following disruption of the cortical actomyosin, nuclear influx was significantly decreased in laser-ablated cells compared with control cells (**Figure 4.3 g**). These results demonstrate that nuclear influx depends on accumulation of actomyosin to the rear cell cortex, and is driven by elevated intracellular pressure in the rear compartment of the cell.

In light of prior work showing that the LINC complex is important for controlling nuclear position in cells migrating through 3D matrices by directly tethering the nucleus to the cytoskeleton (Petrie et al., 2014), we hypothesized that in confined microchannels, elevated pressure at the cell posterior would push the nucleus toward the leading edge of the cell in the absence of the LINC complex. This forward movement of the nucleus would thus alleviate pressure in the cell's posterior compartment, thereby reducing influx. In agreement with this hypothesis, the nucleus was indeed located closer to the front of the cell when SUN1 was depleted (**Figure 4.3 i**). Moreover, SUN1 knockdown reduced nuclear influx of confined cells (**Figure 4.3 j**), whereas nuclear influx of unconfined cells was unaffected by SUN1 depletion. Collectively, these data suggest that the LINC complex tethers the nucleus closer to

the cell rear, which, in conjunction with the pressure buildup at the cell posterior due to elevated RhoA/myosin-II activity, facilitates nuclear influx.

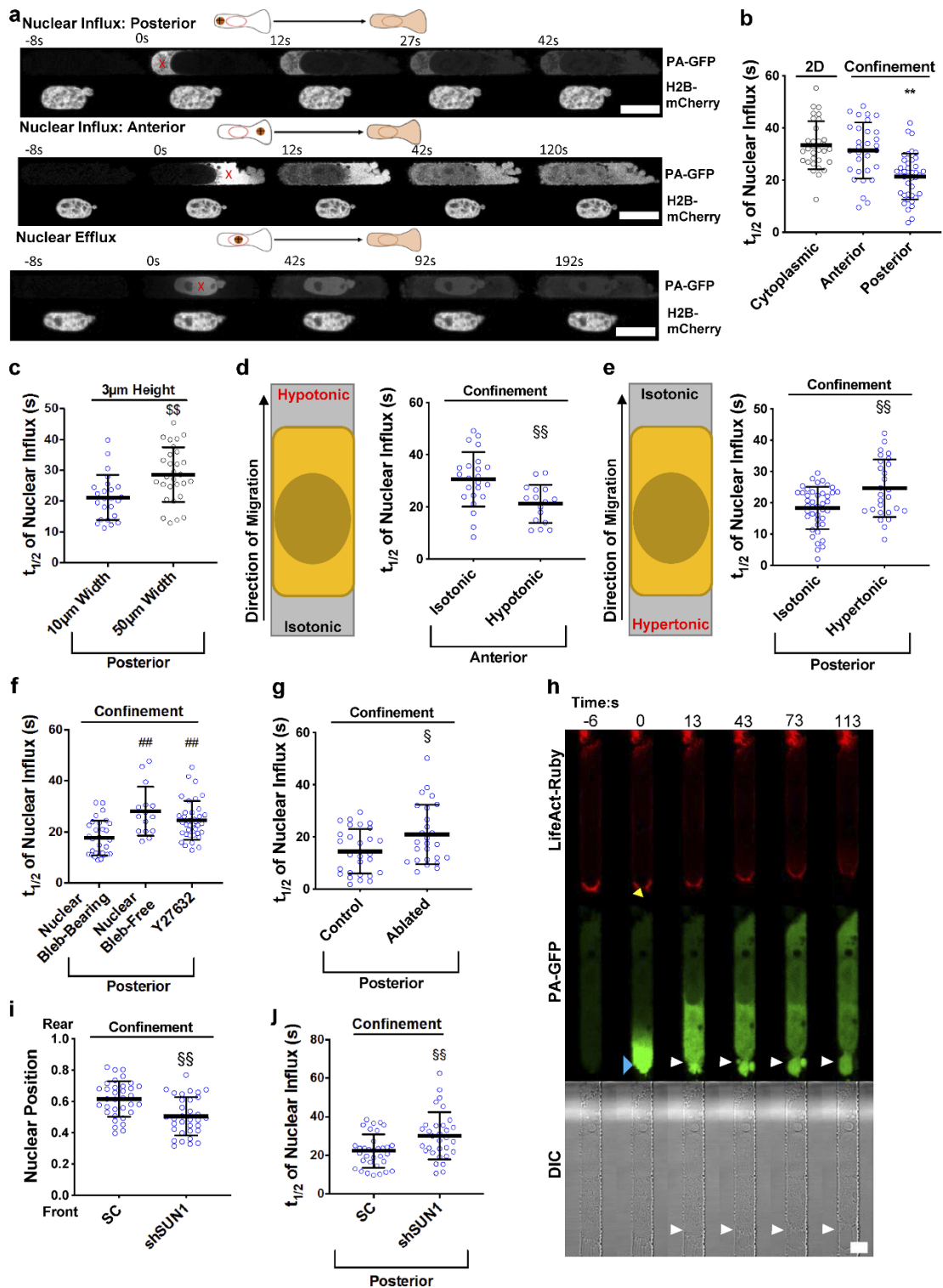


Figure 4.3: Confinement induces elevated nuclear influx that correlates with nuclear blebbing. (a) Time-dependent image sequence of PA-GFP influx into the nucleus from the posterior (top image sequence) or anterior (middle image sequence) compartment, or efflux from the nucleus (bottom image sequence) upon UV excitation in confinement. Red “X” symbols represent points of excitation. Scale bars, 20 μm . (b) Quantification of transport of PA-GFP into the nucleus of HT-1080 cells on 2D or inside confined channels following UV illumination in the anterior or posterior compartments, reported as the $t_{1/2}$ required for the signal (PA-GFP) to reach maximum intensity in the nucleus ($n \geq 27$ cells from three or more independent experiments). (c) $t_{1/2}$ of PA-GFP nuclear influx from the cell posterior for HT-1080 cells inside 10- μm - and 50- μm -wide channels with a fixed height of 3 μm ($n \geq 24$ cells from three independent experiments). (d) Schematic (left) and quantification (right) of $t_{1/2}$ of PA-GFP nuclear influx for confined HT-1080 cells exposed to a hypotonic shock (165 mOsm) at their leading edge ($n \geq 16$ cells from three independent experiments). (e) Schematic (left) and quantification (right) of $t_{1/2}$ of PA-GFP nuclear influx for confined HT-1080 cells exposed to a hypertonic shock (620 mOsm) at their trailing edge ($n \geq 27$ cells from five independent experiments). (f) $t_{1/2}$ of PA-GFP nuclear influx for confined cells with and without nuclear blebs, as well as Y27632-treated (10 μM) HT-1080 cells ($n \geq 15$ cells from four or more independent experiments). (g) $t_{1/2}$ of PA-GFP nuclear influx for control versus actin cortex-ablated HT-1080 cells. Simultaneous photoablation and photoactivation occurred at the cell trailing edge ($n \geq 26$ cells from four independent experiments). (h) Time-dependent image sequence of simultaneous actin cortex ablation (top) and PA-GFP influx into the nucleus (bottom) at the cell posterior. Yellow arrow indicates ablation. Blue arrow indicates photoactivation. White arrows indicate bleb formation as a result of ablation. Scale bar, 10 μm . (i) Nuclear position of scramble control versus SUN1-KD HT-1080 cells ($n \geq 33$ cells from three independent experiments). (j) $t_{1/2}$ of PA-GFP nuclear influx for confined scramble

control cells and SUN1-knockdown HT-1080 cells ($n \geq 31$ cells from three independent experiments). Values represent mean \pm SD. **, $P < 0.01$ relative to 2D cytoplasmic, confinement anterior; \$\$, $P < 0.01$ relative to 10 μm width; ##, $P < 0.01$ relative to confinement nuclear bleb-bearing; §, $P < 0.05$; §§, $P < 0.01$ relative to scramble/isotonic/control.

Discussion

Nuclear envelope blebbing and rupture represent deleterious consequences of confined cell migration, and may have potentially detrimental effects on genomic stability (Denais et al., 2016; Irianto et al., 2016; Raab & Discher, 2017). We herein propose a model by which confinement activates RhoA triggering myosin-II–dependent cortical contractility (Amano et al., 1996) at the cell trailing edge. In light of the direct link between contractility and intracellular pressure (Petrie et al., 2014; Sao et al., 2019), we postulate that elevated contractility along with the preferential tethering of the nucleus toward the cell rear locally increases cytoplasmic pressure in the posterior compartment of the cell, thereby promoting passive nuclear influx through the channels of NPCs. Elevated nuclear influx consequently pressurizes the nucleus, leading to nuclear volume expansion, nuclear envelope blebbing, and rupture. Confinement may also promote nuclear import by directly stretching NPCs and exposing their cytosolic side during nuclear flattening, as recently demonstrated for cells on stiff substrates (Andreu et al., 2022; Elosegui-Artola et al., 2017; Mosalaganti et al., 2022). However, NPC stretching may also result in increased passive nuclear efflux, which we did not observe in our study. This suggests that myosin-II–dependent

buildup of cytoplasmic pressure at the cell posterior is the main driving force for increased nuclear influx. Although pressure was not measured directly in our experiments, several lines of evidence point to a role of posterior cytoplasmic pressure in promoting nuclear influx. Laser ablation of the actomyosin cortex at the cell trailing edge, which has previously been shown to relax cytoplasmic pressure (Tinevez et al., 2009), as well as exposure of the cell trailing edge to a hypertonic shock, which drives water out of the cell, both significantly reduce nuclear influx from the cell posterior. Though indirect measures of intracellular pressure, these findings strongly suggest that cortex contraction forces nuclear influx of cytoplasmic contents into the nucleus, likely through increased intracellular pressure. These findings are complemented by the finding that exposure of the cell leading edge to a hypotonic shock significantly increases nuclear influx from the cell anterior. Furthermore, measurements of PA-GFP flow within the nucleus reveal that flow from the rear to the front of the nucleus is significantly faster than flow in the opposite direction. Collectively, these experiments point to the existence of a pressure gradient, elevated at the cell posterior and decreased at the cell anterior with the nucleus acting as a plug between the two compartments, in tightly confined cells. In the case of nuclear bleb-free cells, cytoplasmic flow around the nucleus is markedly faster than nuclear influx and, as such, pressure is primarily equilibrated through the cytoplasm, thereby preventing nuclear blebbing. In contrast, the $t_{1/2}$ of cytoplasmic flow and nuclear influx are comparable for bleb-bearing cells, suggesting that pressure equilibration must occur through the nucleus and contribute to nuclear blebbing. Taken together, our work

suggests that a cytoplasmic pressure gradient is critical for elevated nuclear influx and nuclear bleb formation.

While our work implicates myosin-II–dependent cytoplasmic pressure at the cell posterior in nuclear bleb formation in confinement, previous studies have demonstrated that myosin-II and vimentin transmit a pulling force to the nucleus after binding with nesprins-3 and pressurize the cell anterior during migration through 3D environments (Petrie et al., 2014). Although we cannot distinguish between nuclear pulling versus pushing, our data using PA-GFP reveal elevated nuclear influx rates at the trailing, but not the leading, edge of confined cells, thus suggesting elevated pressure in the rear compartment of cells in our microfluidic system. While this work does not demonstrate a relationship between this elevated pressure in the rear compartment in the cell and nuclear pushing, this relationship is explored further in Chapter 3. As in the findings presented in Chapter 3, Myosin IIA and Myosin IIB are primarily enriched at the trailing edge of confined cells, and RhoA is active at the polar ends of migrating cells. These findings are consistent with a cortex-driven phenotype, which pushes the nucleus forward through increased cytoplasmic pressure in the cell rear. However, given cells' migratory plasticity, it is likely that cells can switch between myosin-II–mediated pushing and pulling mechanisms in response to the distinct physical cues of the extracellular microenvironment, such as longitudinal migration tracks versus dense ECM, in order to translocate their nucleus most efficiently. Additionally, the mode of migration may dictate whether pulling versus pushing forces dominate. For instance, while cells migrating with a lobopodial

phenotype have been shown to primarily exert pulling forces on the nucleus (Petrie et al., 2014), pushing forces may have a more dominant role in cells that exhibit a bleb-based migration phenotype, as we observe in our system.

In addition to elevated myosin-II at the cell trailing edge, actin and myosin fibers localize on the apical and basal surfaces of the nucleus to deform the nucleus in the dorsoventral direction. Previous studies have demonstrated that pressurization of the nucleus, either by actin deformation or physical confinement, results in nuclear envelope bleb formation and rupture, specifically in areas where the nuclear lamina is not strong enough to withstand this pressure (Hatch & Hetzer, 2016; Kanellos et al., 2015; Takaki et al., 2017; Wiggan et al., 2017). Our results suggest that while perinuclear actomyosin-dependent nuclear deformation is sufficient to induce some nuclear bleb formation in wider microchannels, further pressurization of the nucleus via cortical myosin-II-dependent passive influx from the nuclear trailing edge exacerbates nuclear blebbing in tightly confined channels. In support of this, nuclear influx was significantly reduced in wider ($W = 50 \mu\text{m}$) channels with a fixed height of $3 \mu\text{m}$ as compared with four-walled, tightly confining channels ($W \times H = 10 \times 3 \mu\text{m}^2$), presumably because the nucleus does not compartmentalize the cell in wider channels. Moreover, we predominantly observe blebs on the front of the nucleus, suggesting that pressure-driven flow from the cell rear into the nucleus contributes to nuclear bleb formation. Indeed, by increasing pressure at the cell anterior via the application of a hypotonic shock at the cell leading edge, blebs are formed at the nuclear trailing edge. Taken together, our data suggest synergistic roles of cortical actomyosin-mediated

nuclear influx from the cell posterior and perinuclear actomyosin-dependent nuclear deformation in directional bleb formation.

In order for nuclear blebs to form in these microfluidic channels, force transmission between the cytoskeleton and the nucleus via the LINC complex is critical. The LINC complex connects apical/basal actomyosin fibers to the nuclear envelope to facilitate nuclear deformation (Hatch & Hetzer, 2016; Khatau et al., 2012). Additionally, along with cytoskeletal elements, the LINC complex tethers the nucleus in place, thereby contributing to compartmentalized cellular pressure buildup (Petrie et al., 2014). Our data suggest that in the absence of the LINC complex, the nucleus is unanchored, and therefore susceptible to pressure-driven repositioning within the cell. It is unknown however, whether or not this mechanism is environmentally dependent. If nuclear movement was impeded by a sufficiently narrow constriction (such as in the microfluidic device described in Chapter 2), nuclear repositioning may be inhibited in the absence of the LINC complex. In these microfluidic channels, translocation of the nucleus in the absence of LINC-mediated anchoring relieves pressure at the cell posterior, thereby reducing nuclear influx and subsequent bleb formation. However, if the nucleus becomes stuck behind a more narrow constriction, this pressure may not be relieved in the absence of the LINC complex, and may still play an important role in nuclear blebbing. Therefore, the LINC complex may increase nuclear blebbing both by deforming the nucleus and by promoting actomyosin-induced pressure buildup at the cell posterior. Further studies will be required to determine the relationship

between LINC complex anchoring to the cell rear and increased cytoplasmic pressure in the cell rear in different migration environments.

In view of a direct link between nuclear rupture and DNA damage (Denais et al., 2016; Raab et al., 2016), cell migration through constricted tissue microenvironments may have profound consequences on genomic integrity, cell fate, and cancer evolution (Irianto et al., 2016). Our findings may have broad implications in cancer metastasis. Our data reveal that deregulation of the homeostatic balance of nuclear influx and efflux (influx > efflux) is sufficient to support both nuclear bleb formation and nuclear volume expansion. Overall, our work provides additional insight into the processes of nuclear bleb formation and rupture, which could aid in the development of novel therapeutics to combat metastasizing cancer cells that experience this phenomenon.

Methods

Cell culture and pharmacological inhibitors

Human HT-1080 fibrosarcoma cells (kindly provided by D. Wirtz, Johns Hopkins University, Baltimore, MD) and HOS cells were cultured in DMEM containing 4.5 g/l glucose, L-glutamine, and sodium pyruvate (Gibco) and supplemented with 10% heat inactivated FBS (Gibco) and 1% penicillin/streptomycin (10,000 U/ml; Gibco). Cells were grown in an incubator maintained at 37°C and 5% CO₂, and passaged every 2–4 days.

In select experiments, cells were treated with the following pharmacological agents (obtained from Sigma-Aldrich unless otherwise noted) and corresponding VCs: Y27632 (10 μ M), blebbistatin (50 μ M), lysophosphatidic acid (50 μ M), CN03 Rho activator (Cytoskeleton, Inc., 1 μ g/ml), C3 Transferase Rho inhibitor (Cytoskeleton, Inc., 2 μ g/ml), and LMB (Cell Signaling, 5, 10, or 20 nM).

Cloning, lentivirus preparation, transduction, and transfection

To generate shRNA lentiviral vectors, we subcloned the target sequences into pLVTHM (Addgene; plasmid 12247) using MluI and ClaI as restriction sites. The target sequences are as follows: scramble control: sh1 (5'-GCACTACCAGAGCTA ACTCAGATAGTACT-3'), human MYH9 (5'-ACGGAGATGGAGGACCTTATG-3'), and human MYH10 (5'-GGATCGCTACTATTCAGGA-3').

Lentiviral shRNA targeting human SUN1 and SUN2 was generously given by the Burridge Lab (University of North Carolina at Chapel Hill, Chapel Hill, NC). GFP-lamin-A (pCDH-CMV-BlastiS-P2A-prelamin-A) was generously given by the Lammerding Lab (Cornell University, Ithaca, NY). The following plasmids were purchased from Addgene: pLenti.PGK.LifeAct-Ruby.W (plasmid 51009), pLenti.PGK.H2B-mCherry (plasmid 51007), MYH9-GFP (plasmid 11347), MYH10-mCherry (plasmid 55107), tetO-FUW-eGFP-RHOA-Q63L (plasmid 73081), tetO-FUW-eGFP (plasmid 73083), FUDeltaGW-rtTA (plasmid 19780), RhoA2G FRET biosensor (plasmid 40176, 40179), psPAX2 (plasmid 12260), pMD2.G (plasmid 12259), mCherry-NUP50-N-10 (plasmid 55111), and PA-GFP (plasmid 18697).

The lentiviral plasmid for the expression of the NLS-GFP-MBP-NES(Rev) nuclear transport reporter (pK542) was prepared by sequential cloning of synthetic oligonucleotides and PCR products into pLenti V5-D TOPO (Invitrogen). The reporter contains the N-terminal NLS sequence of SV40 Large T-antigen (PKKRKV) and the C-terminal NES of Rev (LPPLERLTL) that were added to GFP-tagged maltose binding protein (MBP) from *Escherichia coli*. The lentiviral plasmid for the expression of the NLS-GFP-MBP-NES(Survivin) nuclear transport reporter (pK561) was prepared as described above but containing C-terminal NES of Survivin (VKKQFEELTL). NES from Rev is stronger than NES from Survivin, pK542 to localize predominately in the cytoplasm while allowing pK561 to localize in both the cytoplasm and nucleus.

For lentivirus production, 293T/17 cells were cotransfected with psPAX2, pMD2.G, and the lentiviral plasmid. Lentivirus was harvested 48 h after transfection and was purified via centrifugation (50,000 g for 2 h at 4°C). Subsequently, cells were transduced for 24 h with media containing lentiviral particles.

For siRNA knockdown, scramble (sc-37007) and TPR (sc-45343) siRNA were purchased from Santa Cruz Biotechnology. Cells were transiently transfected with siRNA using the Lipofectamine RNAiMax Kit (Invitrogen) according to the manufacturer's protocol.

For transient transfections, 60–80% confluent HT-1080 cells were transfected using Lipofectamine 3000 reagent using the manufacturer's recommendations.

Photolithography and device fabrication

Polydimethylsiloxane-based microfluidic devices, which consist of an array of parallel channels with a fixed channel length of 200 μm , a fixed height of 3 μm , and widths of 10 μm or 50 μm , were fabricated as described previously (Balzer et al., 2012; Paul et al., 2017). Confinement was applied by inducing cells to migrate through a channel with a height of 3 μm and a width of 10 μm . The heights of all channels were verified using a profilometer. For cell migration experiments, channels were coated with 20 $\mu\text{g/ml}$ collagen I (Collagen I Rat Protein, Tail; Thermo Fisher Scientific).

Microfluidic device seeding and live cell imaging

Cells were detached from culture dishes using 0.05% trypsin-EDTA (Gibco), centrifuged at 300 g for 5 min, and resuspended in DMEM (1% penicillin/streptomycin, no FBS) to a concentration of 5×10^6 cells/ml. 10–20 μl of cell suspension was then added to the device inlet, generating a pressure driven flow of cells into the device. Cells were allowed to adhere and spread outside of the channel entrances for at least 5 min. The four inlet wells of the device were then filled with 100 μl media. The bottom three wells were filled with DMEM (no FBS and 1% penicillin/streptomycin), while the top well was filled with DMEM (10% FBS and 1% penicillin/streptomycin) to create a chemotactic gradient within the device. Devices were incubated at 37°C and 5% CO₂ before imaging.

Cells were imaged for every 30 s to 20 min for 4 to 12 h on an inverted Nikon Eclipse Ti microscope (Nikon) with automated controls (NIS-Elements; Nikon) and a $\times 10/0.45$ NA Ph1 objective using time-lapse microscopy. During the experiments, cells were maintained on a temperature and CO₂ controlled stage top incubator (Okolab or Tokai Hit). For select experiments, cells were imaged using FITC and TRITC filters.

Cell migration tracking and analysis

Live cell videos were exported to ImageJ (National Institutes of Health). The Manual Tracking (F. Cordelières, Institut Curie, Orsay, France) and MTrackJ were used for cell path tracking. Cell paths were recorded from the time of complete entry into the microchannel until contact was made with the end of the microchannel. A custom-made MATLAB (MathWorks) script was used to calculate cell speed from the cell path. Dividing or apoptotic cells were excluded from analysis. For each condition, ~ 30 cells were analyzed for each of three or more independent trials unless otherwise noted.

For nuclear blebbing classification, cells were observed with an inverted Nikon Eclipse Ti microscope (Nikon) using a $40\times$ air objective. Nuclear blebbing was tabulated manually.

Actin and nucleus staining

Cells were fixed with 4% paraformaldehyde (Affymetrix), permeabilized in 0.1% Triton X-100 (Sigma-Aldrich), and blocked in 1% bovine serum albumin. Cells were stained with rhodamine or Alexa Fluor 488 phalloidin (1:100; Invitrogen) and Hoechst (1:2,500; Invitrogen).

Confocal imaging

Cells were imaged using a Zeiss LSM 700 confocal microscope (Carl Zeiss MicroImaging) and a Nikon A1 confocal microscope (Nikon) using a 60/63 \times oil objective with a 1.4 NA and a resolution of 1,024 \times 1,024 pixels. During the experiments, cells were maintained on a temperature and CO₂ controlled stage top incubator (Okolab). A 567-, 488-, or 405-nm laser was used for imaging.

Super resolution imaging was performed with Zeiss LSM 800 Confocal with AiryScan super-resolution module with x,y resolution of 120 nm and z resolution of 350 nm.

PA-GFP imaging

HT-1080 cells were transfected with PA-GFP as described above. Cells were imaged using the FRAP capabilities of a Nikon A1 confocal microscope (Nikon) with a 60 \times oil objective. Cells were stimulated for 1 s using UV-violet light (405-nm) at 2% intensity, then imaged. For nuclear influx and efflux, images were taken for 4 min at 1-s intervals using a 488-nm laser with a resolution of 512 \times 512 pixels. For measurements of PA-GFP transport inside the nucleus, images were taken for 20 s at 0.25-s intervals using a 488-nm laser with a resolution of 256 \times 256 pixels. $t_{1/2}$ values

were calculated using curve fitting tools in GraphPad Prism 6 and 7 Software based on the equations:

Influx:

$$Y=Y_0+(Plateau-Y_0)\times[1-\exp(-K\times t)]$$

Efflux:

$$Y=(Y_0-Plateau)\times\exp(-K\times t)+Plateau$$

where Y is intensity in arbitrary units and t is time in seconds, Y₀ is the intensity when time is zero, Plateau is the intensity value at long times, K is the rate constant expressed in s⁻¹, and t_{1/2} is in seconds. The t_{1/2} is computed as ln(2)/K. Ruptured nuclei were excluded from the calculations of nuclear influx and efflux rates.

Osmotic shock experiments

Osmotic shocks were applied as described previously (Stroka et al., 2014). Briefly, hypotonic solutions were prepared by diluting DMEM twofold (165 mOsm) or fourfold (85.5 mOsm) with ultra-pure water. Hypertonic solutions (620 mOsm) were prepared by adding 4% xylose to DMEM. The osmolarity of each solution was measured using freezing point depression with an 3205 Single-Sample Osmometer (Advanced Instruments). After device seeding, cells were allowed to migrate through the confined channels for 2–4 h before application of osmotic shock. Prior to imaging, media in inlets of the microfluidic device was replaced with isotonic, hypotonic, or hypertonic media, as appropriate.

For nuclear influx experiments, cell imaging began 10 min after osmotic shock application and was stopped 50 min after osmotic shock application.

For nuclear blebbing experiments, cells were fixed 2 h after hypotonic shock application.

Actin cortex photoablation

For ablation experiments, cells were seeded into collagen-coated devices 4 h before ablation as described above. 10 mM HEPES (Gibco) was added to growth media.

During ablation experiments, cells were maintained at 37°C. Cells were imaged through a 40×/NA 1.1 water immersion objective (421867-9970-000; Carl Zeiss Imaging) using a 488-nm laser to image PA-GFP and a 561-nm laser to image Lifeact-Ruby at 1-s intervals for 4 min on a Zeiss LSM880 inverted confocal/multiphoton microscope (Carl Zeiss Imaging). Cells were ablated after 6 s at defined 2 × 2-μm regions at the posterior actin cortex using a 780 nm, two-photon laser produced by a Spectra Physics Insight multiphoton excitation source (MKS Instruments). Maximum laser power during experiments varied between 950 mW and 1,000 mW, and ablation was performed at 30% attenuation. Simultaneous to the laser ablation, cells were excited in the same region by a 405-nm laser at 5% attenuation in order to induce activation of PA-GFP. Laser power settings were optimized so that the ablation would disrupt the actin cortex at the cell rear, but leave the cell membrane intact so that the cell may recover after ablation. Ablations were considered successful if the targeted region formed a bleb in response to ablation, but the GFP signal remained contained

within the cell body. Cells that showed GFP escaping from the cell membrane and cells that did not bleb in response to ablation were excluded from the final analysis.

Nuclear size and volume measurements

Cells were imaged using a Zeiss LSM 800 or Nikon A1 confocal microscope equipped with a 63×/60× oil-immersion, 1.2/1.4 (NA) objective. A 567-nm laser was used to image cells whose nuclei were fluorescently labeled with H2B-mCherry. Images were acquired with a resolution of 1,024 × 1,024 pixels. Confocal image slices were spaced 0.5 or 1 μm apart, and the pinhole size was 1 Airy unit. The microscope was equipped with a CO2 Module S (Zeiss or Tokai) and TempModule S (Zeiss) stagetop incubator (Pecon or Tokai) that was set to 37°C with 5% CO2 for long-term imaging.

Nuclear volume was measured from Z-stacks using a custom MATLAB script. Out of focus z-planes were removed. Images from each analyzed focal plane were processed using the binary thresholding function in MATLAB to filter out noise. The nuclear boundary was detected in each image using the Canny Edge Detector operator. The edge was dilated and refilled as to obtain the cross-sectional area of each slice. The volume was calculated by multiplying the average area from two adjacent slices by the z-interval and integrating all values.

FRET-based RhoA activity measurements

Transiently transfected HT-1080 cells expressing the RhoA2G biosensor were chosen for imaging. For both confined and unconfined cells, images at CFP (excitation:

430/24, emission: 470/24), YFP (excitation: 500/20, emission: 535/30), and FRET (excitation: 430/24, emission: 535/30) settings were acquired. For quantification, the mean pixel ratio of FRET over CFP was considered after corresponding background subtraction and outlining the cell boundary by tracing the YFP image. For both the imaging and quantification purposes, Nikon Elements was used.

FLIM of RhoA FRET sensors

Confocal FLIM of live cells that were stably expressing the RhoA2G sensor (Fritz et al., 2013) was performed with the use of Zeiss LSM 780 microscope and a PicoQuant system consisting of the PicoHarp 300 time-correlated single photon counting module, two hybrid PMA-04 detectors, and Sepia II laser control module. During imaging, cells were maintained in a Tecon environmental chamber at 37°C and 5% CO₂. The FLIM data were collected with Apochromat 40×/1.1W Corr 27 lens (Zeiss), using the 440-nm diode laser pulsed at 32 MHz and passed through a 440/488/640-nm triple dichroic mirror (Zeiss) for excitation. A reflection plate diverted the emission to the 482 ± 35-nm filter and PicoQuant PMA-04 hybrid detector. The pinhole size was set to acquire data from 3-μm z-sections, or reduced (up to 1.5 μm z) to limit the emission photon count rate below 10% of the laser excitation rate. Cells migrating in the channels were imaged within a single scan of a 200 × 2,000-pixel window, using 51.67 μs pixel dwell time (48.4 s total scan time). Cells in 2D were imaged within a single scan of a 1,024 × 1,024-pixel window, using 25.21 μs pixel dwell time (61 s total scan time). The time-correlated single photon counting data were acquired within a 31.25-ns time window separated into 8 ps time bins.

FLIM reconvolution and image segmentation

The FLIM data were processed with SymPhoTime 64 (PicoQuant) software, using the customized script for the calculation of the internal response function from 100 data points with no smoothing. The data were binned to assure at least 500 photons per binned pixel, and a cell-specific threshold was applied to eliminate out-of-cell fluorescence. The three-exponential reconvolution was used to fit the fluorescence decays into every binned pixel. Since the RhoA FRET sensor was excluded from the nucleus, resulting in low and variable photon counts in the center of the cells, rectangular areas encompassing the nucleus and cytoplasm alongside the nucleus were excluded during FLIM segmentation.

Segmentation quantification

For FLIM segmentation quantification, the SymPhoTime 64 was used to calculate the intensity-weighted fluorescence lifetime averages (τ_{AI}) in different areas of the cells. Manually drawn regions of interest were drawn to select areas with locally increased RhoA sensor FRET in the front or back of the cells. In cells lacking detectable local RhoA activation, the areas corresponding to one third of the distance from the leading or trailing edge to the nucleus were selected to calculate the τ_{AI} in the front or back of cells, respectively. The remainder of the cytoplasmic areas was defined as cell center and the sum of all cytoplasmic areas as the whole cell signal.

Myosin-II quantification

Myosin-IIA and -IIB intensity profiles were obtained using a custom MATLAB script. For each cell, line scan intensity profiles were obtained and averaged from 20 lines across the cell. Intensity from all cells was compiled, and the curve was smoothed by calculating the moving average (200 points of window size per data sample of 2 million data points). SD was calculated using the Moving Standard Deviation function in MATLAB.

Primary antibodies

Primary antibodies were anti-SUN1 antibody (produced in rabbit; Abcam; ab124770; 1:1,000), anti-SUN2 antibody (rabbit; Abcam; ab124916; 1:1,000), anti-MIIA antibody (rabbit; Sigma-Aldrich; M8064; 1:1,000), and anti-MIIB antibody (N-17; goat; Santa Cruz Biotechnology; SC-47205; 1:7,500). β -Actin was used as a loading control (Purified Mouse Anti-Actin Ab-5; BD Biosciences; 612656; 1:10,000).

Secondary antibodies

Secondary antibodies were anti-mouse IgG, HRP-linked Antibody (Cell Signaling; 7076S; 1:2,000), anti-rabbit IgG, HRP-linked antibody (Cell Signaling; 7074S; 1:2,000), and donkey anti-goat IgG-HRP (Santa Cruz Biosciences; sc-2020; 1:2,000).

Statistical analysis

Data represent the mean \pm SEM or SD from three or more independent experiments for each condition unless stated otherwise. A Student's t test, a one-way or two-way ANOVA test followed by a Tukey's test for multiple comparisons, a two-way

ANOVA test followed by a Sidak's test for multiple comparisons, or a Wilcoxon matched-pairs signed rank test was used to determine statistical significance as appropriate. Statistical significance was identified as $P < 0.05$. Analysis was performed using GraphPad Prism 6 and 7 Software.

CHAPTER 5 – ENUCLEATED CELLS INVADE MORE RAPIDLY THROUGH CONSTRICTIONS⁴

Abstract

Targeting the delivery of therapeutics specifically to diseased tissue enhances their efficacy and decreases their side effects. In collaboration with the Klemke group at the University of California San Diego, we show that mesenchymal stromal cells with their nuclei removed by density-gradient centrifugation following the genetic modification of the cells for their display of chemoattractant receptors and endothelial-cell-binding molecules are effective vehicles for the targeted delivery of therapeutics. The Klemke group demonstrated that enucleated cells neither proliferate nor permanently engraft in the host, yet retain the organelles for energy and protein production, undergo integrin-regulated adhesion to inflamed endothelial cells, and actively home to chemokine gradients established by diseased tissues. Using microfluidic devices which mimic the confined migration observed during inflammation, I demonstrate that enucleated cells migrate more rapidly through 3D constrictions than unmodified stromal cells. These results were complimented by follow-up studies in the Klemke lab in mouse models of acute inflammation and of pancreatitis, where systemically administered enucleated cells expressing two types of

⁴ Portions of this work have been adapted from the following publication Wang W, Alarcon CN, Liu B, Watson F, Searles S, Lee CK, Keys JT, Pi W, Allen D, Lammerding J, Bui JD, Klemke RL (2022) Genetically engineered and enucleated human mesenchymal stromal cells for the targeted delivery of therapeutics to diseased tissue. *Nature Biomedical Engineering*.

Contributions: This work was primarily performed by members of the Klemke group; JT Keys performed microfluidic migration experiments, aided in their interpretation, and contributed to editing of the final manuscript.

chemokine receptor and an endothelial adhesion molecule enhanced the delivery of an anti-inflammatory cytokine to diseased tissue (with respect to unmodified stromal cells and to exosomes derived from bone-marrow-derived stromal cells), attenuating inflammation and ameliorating disease pathology. Our findings that enucleated cells successfully migrate through constrictions demonstrate that, contrary to prior findings, the nucleus is not required for 3D migration. This retained migratory function in 3D is essential for the ability of cargocytes to invade through basement membranes and home to sites of inflammation, and hence represent a versatile delivery vehicle and therapeutic system.

Introduction

The systemic administration of conventional therapeutics is often accompanied by unwanted side effects and toxicity owing to the accumulation of the drug in off-target sites, the lack of drug selectivity and the inability to completely access diseased tissues (Allen & Cullis, 2004; Yoo et al., 2011). For example, cytokines such as IL-10 and IL-12 have potent immunomodulatory functions and the potential to treat various diseases, including acute pancreatitis, inflammatory bowel diseases, and cancer (Fioranelli & Grazia, 2014; Lyerly et al., 2019). However, their short half-life in circulation, low bioavailability in target tissue and adverse effects related to systemic administration hinder clinical successes (Fioranelli & Grazia, 2014; Lyerly et al., 2019). Several targeted-delivery systems have been developed over the years to address these limitations and to improve efficacy, including nanotechnology-based drug delivery systems, antibody–drug conjugates and bioinspired delivery methods

(Yoo et al., 2011). Bioinspired delivery vehicles are especially attractive because they can closely mimic the innate chemical and biological characteristics of biological surfaces in chemical composition, membrane fluidity or 3D protein presentation and, in some cases, possess innate disease-targeting abilities (Fang et al., 2018; Han et al., 2018; Samanta et al., 2018; Yoo et al., 2011). Naturally derived drug delivery vehicles have been shown to display improved biodistribution, biodegradation, immune compatibility and reduced toxicity compared with synthetically derived nanotechnology-based drug delivery systems (Yoo et al., 2011). Mesenchymal stromal cells (MSCs) have gained appreciable attention as therapeutic delivery vehicles, largely because of their intrinsic disease-targeting and paracrine-secretion capacities (Labusca et al., 2018; Thanuja et al., 2018).

Eukaryotic cells have evolved elegant communication systems to guide migrating stem and immune cells to injured or diseased tissues on the basis of the unique expression profiles of chemoattractants, chemokines, selectins, integrins or other cell-surface adhesion molecules (Nitzsche et al., 2017; Sackstein, 2005; Ullah et al., 2019). The physiological process by which cells leave the circulation and home to diseased or injured tissues in response to chemical signals is referred to as chemotactic homing (Ullah et al., 2019). Following adhesion to the endothelium, sequestered cells undergo transendothelial migration, penetrate through the basement membrane and then move into the perivascular space (Ullah et al., 2019). Cells continue to move through the extravascular tissue to sites of disease or injury in response to chemoattractant gradients (Ullah et al., 2019). A number of studies have shown that

chemotactic migration uses complex gradient-sensing mechanisms, signal transduction cascades, substantial amounts of energy for actin-mediated cell shape changes and actin/myosin-mediated force production to actively drive cell propulsion through complex tissues to sites of disease (Labusca et al., 2018; Sackstein, 2005; Ullah et al., 2019).

During the steps of homing where cells undergo transendothelial migration and move through extravascular tissue, cells must squeeze through constrictions much narrower than the cell diameter. This confined migration is limited by the size and stiffness of the nucleus (Davidson et al., 2014; Rowat et al., 2013; Yadav et al., 2018). In order to ensure efficacy of a cell-based delivery system, it will therefore be necessary to ensure that this system can successfully squeeze through these constrictions. Existing cell-free delivery vehicles can neither actively chemotax through the vascular barrier nor can they physically propel themselves deeply into complex tissues in response to chemical signals (Thanuja et al., 2018). Enucleation may improve the ability of cell-based delivery systems to invade through tissues, as it has been shown that reduced nuclear stiffness enables the ability of cells to invade through tissues (Bell et al., 2021; Harada et al., 2014; Lin et al., 2019; Liu et al., 2017; Rowat et al., 2013). While enucleation of cell-based delivery vehicles has the benefit of ensuring that these systems do not replicate within the host, it is worth considering how complete removal of the nucleus would impact cells' migratory ability. Prior findings have demonstrated that enucleated cells retain many key biological functions, including their ability to migrate and respond to chemotactic gradients (Graham et al., 2018; Malawista et al.,

1989). There is some existing evidence that enucleated cells may display reduced migration in 3D environments (Graham et al., 2018; Petrie et al., 2014). However, these findings were reported in in vitro systems for modeling confined migration (3D cell-derived matrix and collagen matrices) and it is unknown how enucleated cells would behave in vivo.

Ideally, cell-based delivery vehicles could be engineered with enhanced chemotactic abilities for improved targeted drug delivery (Ullah et al., 2019), but such delivery systems face several limitations before their translation to the clinic (Thanuja M.Y. et al., 2018). For example, whereas cells such as MSCs have natural disease trophic properties, the inconsistent and insufficient homing of MSCs to target tissues following systemic infusion is considered a major contributor to the inadequate efficacy of MSC-based therapies (Ullah et al., 2019). Notably, MSCs are largely limited by their initial entrapment in pulmonary capillaries after intravenous (i.v.) injection, their inconsistent expression of chemokine homing receptors and their lack of expression of endothelial adhesion molecules (U. M. Fischer et al., 2008; Karp & Leng Teo, 2009; Ullah et al., 2019). This is further compounded by the inability to control cell fate in vivo, such as the secretion of undesired therapeutic factors, by unpredictable engraftment into the body and by their differentiation into unwanted cell types in vivo, all of which notably limit predictable and reproducible therapeutic delivery (Galipeau & Sensébé, 2018). Although cell-engineering and genetic-engineering approaches can overcome many of these hurdles, obtaining regulatory

approval for cells with multiple genomic modifications remains difficult (Marks et al., 2016).

Here we report the use of recent bioengineering techniques to endow MSCs with multiple chemoattractant receptors and endothelial cell-adhesion molecules that mediate homing to inflamed and diseased tissues. To render bioengineered MSCs safe and controllable, we use large-scale physical enucleation to generate a new type of disease homing CFDV, which we named ‘cargocytes’. Cargocytes retain important intrinsic cellular functions, such as protein translation and secretion, active chemotactic migration towards defined chemokine signals and regulated high-affinity integrin activation and endothelial cell adhesion in vitro. Using a microfluidic model of the in vivo migration environment, we demonstrate that cargocytes retain their ability to migrate through 3D constrictions following enucleation. In two animal models of disease, we demonstrate that bioengineered cargocytes robustly home and deliver therapeutic cytokine cargos to diseased tissues, ameliorating disease pathology. Bioengineered cargocytes use active chemotaxis and endothelial adhesion to deliver therapeutic cargos efficiently and specifically to targeted tissues.

Results

Cargocytes retain important organelles and cellular functions

The principle for physically enucleating mammalian cells using Cytochalasin B and Ficoll density-gradient ultracentrifugation was established over 40 years ago (Wigler

et al., 1976). However, research on the resulting enucleated cells has been primarily limited to in vitro studies (Graham et al., 2018; Shay, 1987; Vanessa et al., 2007). To our knowledge, the potential of these artificially enucleated cells to be bioengineered for in vivo therapeutic delivery has not yet been explored (**Figure 5.1a**). While various cell types can be enucleated (Graham et al., 2018; Shay, 1987; Vanessa et al., 2007), we selected hTERT-immortalized adipose-derived MSCs (hT-MSC) for generating prototype cargocytes because MSCs have proven therapeutic potential in clinical studies and the immortalized phenotype provides a homogenous cell population with consistent characteristics to facilitate further cell and genetic engineering (Galipeau & Sensébé, 2018; Wolbank et al., 2009). We optimized protocols to routinely achieve >95% enucleation efficiency of hT-MSCs, with an 80–90% recovery rate. The hT-MSC-derived cargocytes (hereafter, ‘cargocyte’) are substantially smaller than hT-MSCs in suspension (**Figure 5.1b,c**) and readily attach to tissue culture plates with well-organized cytoskeletal structure (**Figure 5.1d**). Cargocytes are viable for up to 72 h post enucleation, as shown by the trypan blue dye exclusion assay (**Figure 5.1e**). Together, these results indicate that cargocytes retain critical cell structures and functions, and therefore have potential for in vivo homing and delivery of genetically encoded therapeutics.

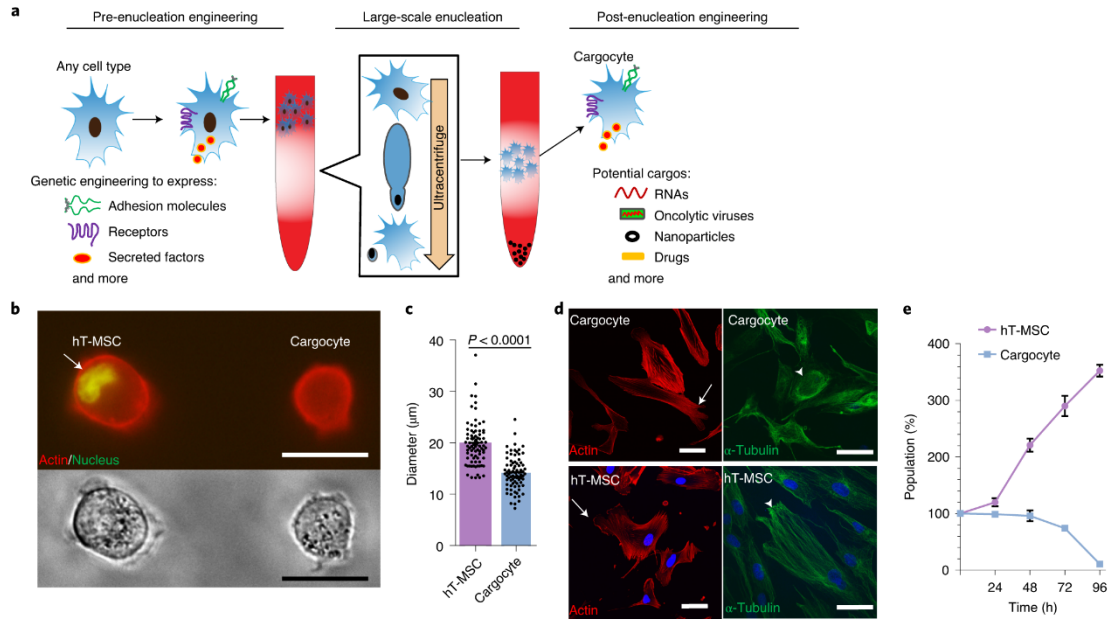


Figure 5.1: Enucleated Cells Retain Important Cell Functions. **a**, Schematic of workflow for therapeutic uses of bioengineered enucleated cells (cargocytes). **b**, Fluorescent image (top) and phase image (bottom) show hT-MSCs and cargocytes in suspension. Representative images out of 30 images obtained are shown. Cortical actin was labelled with LifeAct RFP. Arrow points to the cell nucleus stained with Vybrant Dycycle Green. Scale bar, 20 μm . **c**, Average diameter of hT-MSCs or cargocytes in suspension. Mean \pm s.e.m.; $n = 80$ individual cells/cargocytes. P value, two-tailed unpaired t -test. **d**, Fluorescent confocal images of hT-MSCs/cargocytes stained with rhodamine phalloidin for F-Actin cytoskeleton (left), or anti- α -Tubulin antibody for microtubule network (right), and Hoechst 33342 for nucleus. Representative images out of 30 images obtained are shown. Arrows point to the F-Actin cytoskeleton; arrowheads point to the microtubule network. Scale bar, 50 μm . **e**, Percentage of viable hT-MSCs/cargocytes versus initial population over time. Mean \pm s.e.m.; $n = 6$ biological replicates. All data are representative of at least 2 independent experiments.

Cargocytes Chemotax Towards Chemoattractant Gradients

Having demonstrated that hT-MSCs retain crucial subcellular organelles including Golgi, mitochondria, ER, lysosomes, and endosomes, maintain a well-organized cytoskeletal structure during adhesion, and remain viable for up to 72 hours post-enucleation, we wanted to assess their ability to chemotax and migrate through confined environments.

Chemotaxis is a critical step controlling active cell homing in vivo (Karp & Leng Teo, 2009), so we first investigated the chemotactic ability of cargocytes. Consistent with previous studies (Malawista et al., 1989), cargocytes sensed and migrated towards various chemoattractants in an in vitro Boyden chamber assay, and invaded through 3D Matrigel-coated membranes towards fetal bovine serum (FBS) gradients in a basement membrane invasion assay (H. Wang et al., 2021). Additionally, we used a microfluidic device in which LifeAct-RFP-labelled hT-MSCs and cargocytes migrate along an FBS gradient through confined 3D constrictions that mimic interstitial pores (Keys et al., 2018). Cell chemotaxis was imaged by time-lapse confocal microscopy to record the time required for cells to migrate through individual constrictions. Notably, cargocytes efficiently passed through small constrictions ($\leq 2 \times 5 \mu\text{m}$ in cross-section), whereas hT-MSCs were often trapped in confined constrictions (**Figure 5.a,b**). This result suggests that cargocytes may have better deformability compared with parental cells, which is consistent with previous studies showing that the nucleus is 2 to 10 times stiffer than the surrounding cytoplasm and physically decoupling the nucleus from the cytoskeleton is sufficient to increase cytoskeletal deformability (Caille et al., 2002; Guilak et al., 2000; Lammerding, 2011; Stewart-Hutchinson et al., 2008). These

findings are additionally significant as we confirm that cargocytes do not display any of the 3D migration defects which have previously been observed in other enucleated cell lines (Khatau et al., 2012; Petrie et al., 2014). Together, these findings demonstrate that cargocytes retain intrinsic chemotaxis activity, the ability to invade through basement membranes, and have better deformability than parental MSCs, which may better facilitate passing through small capillaries, endothelial cell layers or interstitial spaces *in vivo*.

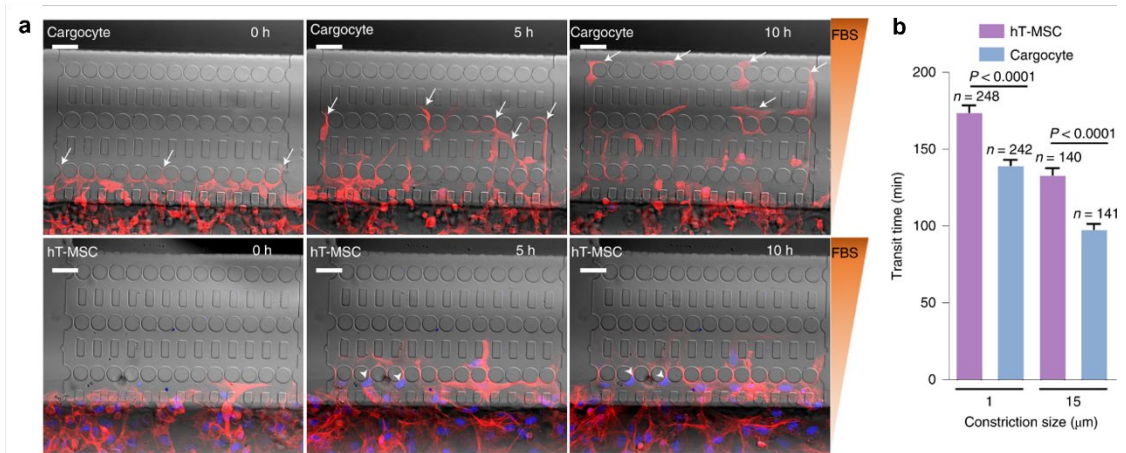


Figure 5.2: Cargocytes have chemotaxis activities and migrate better through confined spaces. a, Time-lapse image sequence of hT-MSCs and cargocytes moving through constrictions ($\leq 2 \times 5 \mu\text{m}$ in cross-section) along an FBS gradient in a microfluidic device. F-actin cytoskeleton (red) was labelled with LifeAct RFP and cell nucleus (blue) was stained with Hoechst 33342. Arrows point to migrating cargocytes and arrowheads point to hT-MSCs trapped in the confined constrictions. Scale bar, $50 \mu\text{m}$. **b**, MSCs and cargocytes were treated as in **a**. Bar graph shows the average time required for cells to migrate through an individual microfluidic constriction. Data for both confined ($\leq 2 \times 5 \mu\text{m}$) and unconfined ($15 \times 5 \mu\text{m}$) constrictions are shown. Mean \pm s.e.m. Data were pooled from 3 independent experiments. Exact number in each group shown above the bar. *P* values, one-way ANOVA with Bonferroni's multiple comparisons test.

Cargocytes bioengineered with homing molecules specifically home to inflamed tissue in vivo

Cell homing to disease foci involves a multi-step process requiring precise coordination of integrins, adhesion molecules and chemokine receptors (Karp & Leng Teo, 2009; Ullah et al., 2019). This prompted us to determine whether cargocytes can

be engineered to simultaneously express multiple functional chemokine receptors and adhesion molecules important for cell homing. In proof-of-principle studies, we bioengineered hT-MSCs to express CCR2, CXCR4 and PSGL-1/FUT-7, and cells with high expression of all three cell surface markers (named MSC^{Tri-E}) were enriched using fluorescence-activated cell sorting (FACS). These homing receptors commonly mediate leukocyte cell homing to most inflammatory tissues (Sackstein, 2005; Ullah et al., 2019). We established 19 single cell clones from MSC^{Tri-E} with high expression of all three markers, and selected Clone 19 (MSC^{Tri-E} C19, that is, **Triple-engineered Clone 19**) for subsequent experiments on the basis of surface expression, growth rate and cell size, and derived cargocytes from this clonal cell line (cargocyte^{Tri-E} C19).

We next wanted to determine whether bioengineered cargocytes administered i.v. can home to sites of inflammation in vivo. However, one major obstacle for therapeutic cells administered i.v. is the initial trapping in the lung capillaries, which not only reduces homing efficiency (Fischer et al., 2008), but may also induce severe complications such as pulmonary embolism (Boltze et al., 2015; Jung et al., 2013). Since cargocytes are smaller, more deformable and can transit through small constrictions more effectively than nucleated parental hT-MSCs (**Figure 5.2a,b**), we hypothesized that cargocytes may also pass through microvasculature (that is, pulmonary capillaries) more efficiently than parental cells, which may facilitate better in vivo homing to the target tissue. To investigate this possibility, hT-MSCs or cargocytes were double-labelled with LifeAct RFP and vital dye Vybrant-DiD prior to

i.v. injection in mice. Twenty-four hours post injection, flow cytometry analysis of lung tissue detected substantially fewer cargocytes compared with parental cells (>2-fold decrease, **Figure 5.3a**). To further decrease lung entrapment, we cultured MSCs in hanging drops to generate 3D-cultured MSCs that were smaller than traditional 2D-cultured MSCs and showed decreased lung trapping (**Figure 5.3a**) as previously reported (Thomas et al., 2010). When 3D-cultured MSCs were enucleated, the resulting 3D-cargocytes were the smallest and had the least lung trapping (**Figure 5.3a**). Subsequent in vivo homing assays used 3D-hT-MSCs and 3D-cargocytes unless noted otherwise.

We first tested the in vivo homing ability of bioengineered MSCs and cargocytes in an established mouse model of acute ear inflammation. Bacterial-derived lipopolysaccharide (LPS) was intradermally (i.d.) injected into the pinna to induce acute local inflammation, while saline was i.d. injected into the contralateral ear as a control (Levy et al., 2013). This model allows examination of therapeutic cell homing quantitatively between an inflamed and non-inflamed contralateral tissue within the same animal (Levy et al., 2013). Three dimensional-MSCs and three dimensional-cargocytes^{Tri-E C19} were labelled with Vybrant-DiD and i.v. injected into mice 6 h after LPS injection. Mouse tissues were collected 24 h later and analysed by flow cytometry for DiD⁺F4/80⁻ cells. The pan-macrophage marker F4/80⁻ was used to exclude the possibility of non-specific Vybrant-DiD incorporation into mouse macrophages (Gordon et al., 1992).

Three dimensional-cargocyte^{Tri-E C19} robustly homed to the inflamed ear, but not to the uninflamed control ear from the same mouse, suggesting the homing is specific (**Figure 5.3b**). While non-engineered 3D-cargocytes and 3D-cargocyte^{Tri-E C19} had similar low levels of lung trapping, 3D-cargocyte^{Tri-E C19} had a >6-fold increased homing to the inflamed ear (**Figure 5.3b**), suggesting that bioengineering with CCR2, CXCR4 and PSGL-1 enabled cargocytes to specifically and efficiently home to the target tissue in vivo. Three dimensional-cargocyte^{Tri-E C19} also showed substantially better homing compared with mouse D1 MSCs or D1 cargocytes (**Figure 5.3b**), while D1 MSC is a syngeneic MSC line from BALB/c mice that possesses endogenous homing abilities (Devine et al., 2002). Importantly, 3D-cargocyte^{Tri-E C19} had an approximately 2-fold increase in homing to inflamed tissue compared with parental 3D-MSC^{Tri-E C19}, which is probably due to reduced lung trapping by cargocytes.

The homing result was independently confirmed using a bioluminescence assay with firefly luciferase (Fluc). It is notable that firefly luciferase is an intracellular enzyme that requires ATP for functional bioactivity (Ignowski & Schaffer, 2004). Therefore, the bioluminescence assay only detects viable cells/cargocytes expressing Fluc in different tissues at the time of imaging. MSC^{Tri-E C19} and cargocyte^{Tri-E C19} transfected with Fluc mRNA showed comparable bioluminescence in vitro. Consistent with our results using Vybrant-DiD labelling, the bioluminescence assay showed 3D-cargocyte^{Tri-E C19} had decreased lung trapping but dramatically increased homing to the inflamed ear compared with 3D-MSC^{Tri-E C19} as early as 2 h post i.v. injection (**Figure 5.3c**).

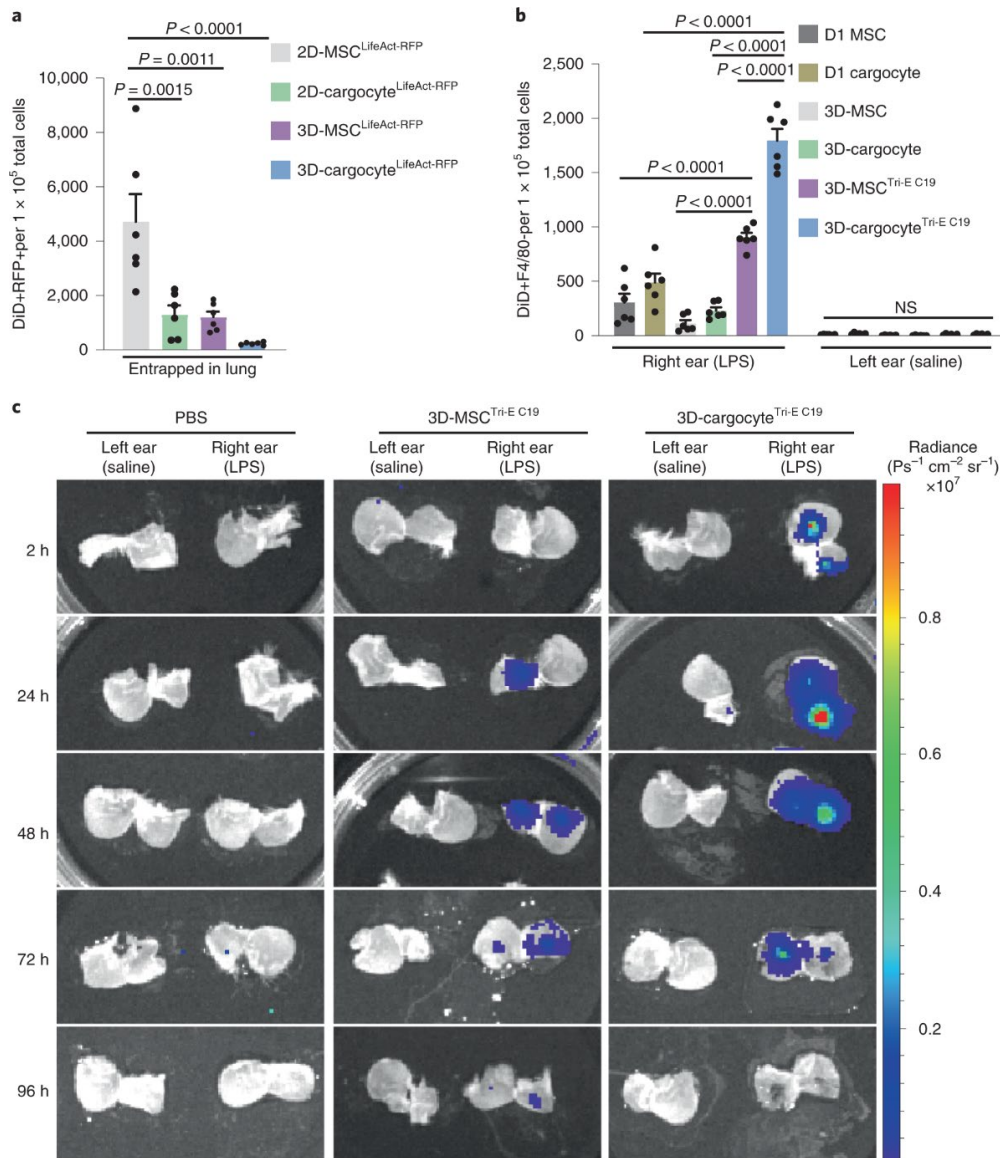


Figure 5.3: Bioengineered cargocytes actively and specifically home to the inflamed ear.

a, Number of DiD⁺RFP⁺ double-positive cells out of 1×10^5 total cells collected from mouse lung 24 h post i.v. injection and detected by flow cytometry. Mean \pm s.e.m., $n = 6$ mice. **b**, Mice were intradermally (i.d.) injected with LPS in the right ear and saline in the left, followed by i.v. injection of DiD-labelled MSCs or cargocytes 6 h later. Bar graphs show the number of DiD⁺F4/80⁻ cells out of 1×10^5 total cells collected from mouse ears 24 h post injection and detected by flow cytometry. Mean \pm s.e.m., $n = 6$ mice. **c**, Mice were treated as

in **b** and then i.v. injected with 1×10^6 3D-MSCTri-E C19 or 3D-cargocyteTri-E C19 transfected with firefly luciferase mRNA. Mice were euthanized at indicated time points after i.v. injection. The dorsal skin of the mouse ears was peeled from the underlying cartilage and the subcutaneous surfaces of the tissue were directly soaked in VivoGlo-luciferin substrate and immediately subjected to bioluminescence imaging with IVIS Lumina Series III. For **a** and **b**, adjusted *P* values shown above the bars, one-way ANOVA with Tukey's multiple comparisons test. All data are representative of at least 2 independent experiments.

Discussion

Therapeutic agents administered systemically often result in unwanted side effects and in toxicity owing to their accumulation in off-target sites, the lack of drug selectivity and the inability to completely access diseased foci (Allen & Cullis, 2004; Yoo et al., 2011). Therefore, there is a substantial need for new systems that can deliver therapeutics precisely to diseased tissues to decrease unwanted side effects and improve efficacy. The primary goal of this study was to develop a bioinspired delivery vehicle that specifically targets diseased tissues while maintaining a safe and controllable profile important for clinical applications. Our unique approach facilitates the introduction of multiple genetic elements into a cell without introducing major safety concerns, since the modified chromatin is removed during enucleation. Enucleated cells are distinct from other CFDVs in that they retain crucial organelles for energy and protein production, do not proliferate or permanently engraft in the host, undergo regulated integrin-mediated adhesion to inflamed endothelial cells and actively home to specific chemokine gradients released by diseased tissues. Cargocytes are also distinct from CFDVs in that they actively extravasate out of the

vasculature, and synthesize and secrete therapeutics at the site of disease. In proof-of-principle experiments, cargocytes showed substantially improved homing and delivery of anti-inflammatory cytokine IL-10 to target tissue compared with normal MSCs. These findings indicate that the cell-like functions of cargocytes can be further enhanced through cell engineering and genetic engineering to improve therapeutic delivery.

One of the greatest challenges of current CFDVs is the inability to actively migrate across the endothelium into target tissue interstitium to disease foci following systemic administration (Thanuja et al., 2018). Cargocytes overcome these limitations as they are able to migrate through constrictions in both in vitro models of 3D migration and in in vivo models of inflammation in mice. These findings are significant in that they demonstrate the viability of cargocytes as drug delivery vehicles to target sites of inflammation. These findings also contradict earlier reports that enucleation results in slower migration through 3D environments (Graham et al., 2018; Petrie et al., 2014). These studies observed the migration of cells randomly seeded into 3D protein matrices (either collagen or cell-derived matrix), whereas we report migration in microfluidic channels, Boyden Chambers, and in vivo. One explanation for the difference in these findings could be a difference in cell type. The earlier reports looked at rat embryonic fibroblasts, human umbilical vein endothelial cells, and primary human foreskin fibroblasts, while the cells studied here were mesenchymal stromal cells, which, unlike the other cells noted, demonstrate considerable ability to home to sites of inflammation in vivo. The prior reports

additionally observed random migration within a 3D environment, whereas our results describe migration through 3D constrictions in response to a chemoattractant. It is possible that our use of a chemoattractant gradient enabled directed chemotaxis which may not have been a key driver of migration in the earlier studies. Additionally, cells migrating *in vivo* display the ability to switch between migration modes depending on variations in environmental conditions, such as adhesiveness, stiffness, and crosslinking of the surrounding matrix. Our use of multiple models of 3D migration demonstrate that cargocytes are able to migrate through varying types of confined environments, in the absence of the nucleus.

Cargocytes also possess several distinct features over intact cell delivery vehicles. First, it remains difficult to obtain regulatory approval for the clinical use of extensively engineered cells (especially stem cells such as MSCs) owing to safety concerns (Marks et al., 2016). Second, primary cells collected from donors are usually heterogeneous and not amenable to creating proliferative clonal cell lines owing to senescence after *in vitro* passaging, which limits bioengineering and therapeutic capacities (Nowakowski et al., 2013). Third, cargocytes have a more defined and predictable cell fate *in vivo* because they cannot perform new gene transcription and therefore can neither be induced to differentiate or to produce unpredictable paracrine factors, nor can they engraft and proliferate uncontrollably. This ensures that crucial therapeutic features established through bioengineering *ex vivo* are correctly conveyed *in vivo*, making the therapeutic delivery of cargocytes more precise and reliable for clinical applications, with reduced off-target effects. Fourth, compared with intact

cells, cargocytes are smaller and lack rigid nuclei (**Figure 5.1**), which translates to decreased lung entrapment and improved biodistribution, as well as to enhanced homing to target tissues (Wang et al., 2021). These unique attributes notably improved therapeutic delivery to diseased tissues (Wang et al., 2021) compared with their larger nucleated parental MSCs. Importantly, because cargocytes are more deformable and migrate through small vessel-like constrictions better than cells (**Figure 5.1**), patients may have a lower risk of severe adverse events, such as pulmonary or cerebral emboli associated with the systemic administration of cells with nuclei (Boltze et al., 2015; Cui et al., 2015; Jung et al., 2013). Therefore, cargocytes are uniquely positioned in between cells and other CFDV systems (such as exosomes, erythrocytes or nanoghosts) that are currently under development for clinical applications.

Methods

Animals

All animals were housed and treated according to the University of California San Diego animal welfare guidelines as described and approved by the UCSD Institutional Animal Care and Use Committee (protocol [S12005](#)) in a specific pathogen-free vivarium. The light cycle was 6 am to 6 pm, temperature was between 69 to 71 °F and humidity was between 40–60%. BALB/cJ and C57BL/6 J mice were purchased from Jackson Laboratory. C.N.A., who is a board-certified veterinary pathologist (Diplomate, American College of Veterinary Pathologists, Veterinary Medical Board license no. VET19413), designed and supervised all experimental animal procedures, including animal colony management, injections, tissue collection, tissue processing,

organ histopathology and daily animal health examinations. Mouse serum chemistry analyses and whole blood counts were performed in the ACP Diagnostic Services Laboratory at UCSD.

Cell culture

Human telomerase reverse transcriptase (hTERT)-immortalized, adipose-derived mesenchymal stromal cells (hereafter referred to as 'hT-MSCs') were purchased from ATCC (SCRC-4000). Primary human bone marrow-derived MSCs were obtained through Texas A&M College of Medicine's Institute for Regenerative Medicine. Primary human umbilical cord-derived MSCs were a generous gift from Dr Mana Parast (UCSD). MSCs were cultured in complete culture medium (CCM), including alpha MEM (Gibco, 12561) supplemented with 16.5% premium FBS (Atlanta Biologicals, S1150), 1% HEPES (Gibco, 15630), 1% Glutamax 100X (Gibco, 35050) and 1% anti-anti 100X (Gibco, 15240). hT-MSCs were authenticated by IDEXX Laboratories, while other cells were authenticated by ATCC. All cell stocks tested mycoplasma negative by PCR.

Cell enucleation

Cell enucleation was modified from the previously published protocol (Wigler et al., 1976). Ficoll PM400 (GE Healthcare, 17-0300-500) was dissolved into a 50% (wt/wt) solution with ultrapure water (Invitrogen, 10977-015) by continual magnetic stirring for 24 h at room temperature, followed by autoclaving. Refractive index was measured to ensure consistency (range 1.4230–1.4290) on a refractometer (Reichert, 13940000).

The Ficoll stock was aliquoted and stored at $-20\text{ }^{\circ}\text{C}$. To make discontinuous gradients, 50% stock Ficoll solution was diluted to 25% with 2X MEM (diluted from Gibco, 11430) and then further diluted with 1X MEM (diluted from 2X MEM) for the 17, 16, 15 and 12.5% Ficoll solutions. Cytochalasin B (Sigma Aldrich, C6762) was added to all Ficoll solutions at a final concentration of $10\text{ }\mu\text{g ml}^{-1}$. Ficoll solutions (2 ml 25%, 2 ml 17%, 0.5 ml 16%, 0.5 ml 15% and 2 ml 12.5%) were carefully layered into a 13.2 ml ultra-clear tube (Beckman Coulter, 344059) and equilibrated in a $37\text{ }^{\circ}\text{C}$ tissue culture incubator overnight. Subconfluent cells were collected with Accutase (Innovative Cell Technologies, AT104-500), resuspended in 3.2 ml 12.5% Ficoll solution and then carefully loaded onto the prepared discontinuous gradients and topped off with 1X MEM. Tubes were balanced in swing buckets of the SW41 rotor, run in a pre-warmed ($31\text{ }^{\circ}\text{C}$) Beckman Coulter L8-60M ultracentrifuge for 60 min at 26,000 r.p.m. with minimal braking. Fractions were collected with low-binding pipette tips into low-binding tubes and washed with serum-free media 3 times. Cargocyte efficiency (purity, % enucleated out of input number of cells) was examined using an epifluorescence microscope (Nikon Eclipse Ti) after staining with Vybrant Dycycle Green (Invitrogen, V35004) for 10 min, and the yield of viable cargocytes was measured in Cell Countess (ThermoFisher). Diameters of cargocytes and parental MSCs were determined by the NIS-Elements AR 3.0 software (Nikon).

Transfection of in vitro synthesized mRNA

Green fluorescent protein (GFP) mRNA, Gaussia luciferase mRNA, firefly luciferase mRNA and human IL-10 were synthesized by TriLink Biotechnologies. The protein

coding sequence was flanked by 5'- and 3'-untranslated regions from mouse α -globin. Full substitution of pseudouridine was used to synthesize transcripts. After adding the 5' cap structure (CleanCap AG) and 3' poly(A) tail (120 A), the synthesized mRNAs were purified with silica membrane. The pre-made mRNAs from TriLink were directly used for mRNA transfection. Briefly, 1 μ g synthesized mRNA was added to 49 μ l warm opti-MEM and 4 μ l Lipofectamine 3000 (ThermoFisher, L3000008) was separately added to 46 μ l Opti-MEM. The Lipofectamine and mRNA solutions were incubated for 5 min, then were mixed and incubated for another 15 min at room temperature. MSCs or cargocytes were resuspended in CCM without antibiotics at 1e6 cells per ml. Mixed mRNA + lipofectamine-3000 solution (100 μ l) was added to 1 ml MSC or cargocyte suspension, mixed thoroughly and incubated at 37 °C for 30 min. After transfection, MSCs or cargocytes were washed twice with CCM, then either used immediately for in vivo experiments or plated on tissue culture plates. For GFP mRNA, transfected MSCs or cargocytes were plated in 6-well plates (1e5 per well), and GFP expression was analysed with the epifluorescence microscope (Nikon Eclipse Ti) or by flow cytometry. For Gaussia luciferase mRNA, transfected MSCs or cargocytes were plated in 24-well plates (25,000 per well, 1 ml CCM media). Conditioned medium was taken 48 h after transfection and luciferase activity was determined as relative luminescence units (RLU) using BioLux Gaussia luciferase Assay Kit (NEB, E3300) on GloMax 96 microplate luminometer (Promega). For human IL-10 mRNAs, transfected MSCs or cargocytes were either plated in a 24-well plate (25,000 per well, 1 ml CCM media) for collecting conditioned media at indicated time points to analyse cytokine expression by ELISA, or plated in a 6-well plate

(1e5 per well, 2 ml CCM media) for collecting conditioned media at 24 h to treat RAW macrophage cells. The phosphorylation of Stat3 was then analysed by western blot. Exosome transfection with in vitro synthesized mRNA was performed using the kit (System Biosciences, EXFT10A-1) according to the manufacturer's instructions. Briefly, 20 billion exosomes (Erivan Bio, B-MSC exosomes) from human bone marrow-derived MSC were transfected with 1 µg synthesized mRNA in the presence of Exo-fect solution and incubated at 37 °C in a shaker for 10 min. Transfection was stopped by ExoQuick-TC and exosomes were precipitated by centrifugation at 14,000 r.p.m. for 3 min. The exosome pellets were resuspended in 300 µl Dulbecco's phosphate-buffered saline (PBS). To test the transfection efficiency, 100 µl of transfected exosomes was added to 293 cells (1e5 cells per well, 24-well plate), conditioned media was collected 24 h later and IL-10 level was determined by ELISA.

3D cell culture by hanging drops

Generation of 3D MSC spheroids in hanging drops was modified from previously published protocols (Bartosh & Ylostalo, 2014; J. B. Thomas et al., 2010). Briefly, MSCs were plated as drops on an inverted plastic dish lid (Olympus Plastics, 32-106) in 35 µl CCM at 30,000 cells per drop. The lid was then replaced to cover the plate bottom containing 15 ml PBS (ThermoFisher, 14190250) to prevent evaporation. Hanging drop cultures were grown at 37 °C for approximately 40 h with 5% CO₂. To obtain a single-cell suspension, spheroids were collected into tubes and incubated with Accutase (Innovative Cell Technologies, AT104-500) at room temperature for 20 min with gentle pipetting every 5 min. The cell–Accutase suspension was diluted with

CCM and dissociated spheroids were further treated with 100 $\mu\text{g ml}^{-1}$ DNase I (Sigma Aldrich, 10104159001) for 10 min at 37 °C. Cells were passed through a 70 μm cell strainer (BioPioneer, DGN258368) to obtain a single-cell suspension.

3D cell culture by spinner flasks

Generation of MSC spheroids via spinner flask was modified on the basis of previously published protocols for less compaction and easier dissociation (Frith et al., 2009). Briefly, MSCs were plated at 0.8 million cells per plate (Olympus Plastics, 25-203) in 15 ml culture medium around 4 d before input into the spinner flask. To prepare the spinner flask (Corning, 4500-500), the flask was coated with 2 ml Sigmacote (Sigma, SL2-100ML) to prevent cells from sticking to the glass, then autoclaved for 30 min. On the day of collection, 50 million cells were collected using Accutase and incubated on ice for 1 h before adding into the spinner flask. Cells were cultured at 37 °C for approximately 45 h with 5% CO₂ and the rotation speed was set to 60 r.p.m. To obtain a single-cell suspension, cells were collected from the spinner flask after 45 h and incubated with Accutase for 25 min in a 37 °C water bath. Cells were pipetted every 5 min to promote dissociation, then passed through a 70 μm cell strainer to obtain a single-cell suspension.

LDV-FITC binding assay

Leu-1 N-2-(4-(((2methylphenyl)amino)carbonyl)amino)phenyl)acetyl-, Lys-6 N-FITC conjugate (LDV-FITC) was purchased from R&D systems (4577/1). The LDV-FITC binding assay was performed as previously described (Hyduk et al., 2011).

Briefly, MSCs or cargoocytes (1×10^6 per 100 μ l) suspended in HEPES buffer (140 mM NaCl, 2.5 mM KCL, 1.8 mM CaCl₂, 1 mM MgCl₂, 20 mM HEPES, 0.5% FBS, pH 7.4) were incubated with 4 nM LDV-FITC for 15 min at 37°C, then stimulated with or without SDF-1 α (500 ng ml⁻¹) for 2 min and immediately fixed for 5 min with 1 ml pre-warmed 1% paraformaldehyde at 22°C to fix bound LDV-FITC. Unconjugated LDV (1 μ M) was used as a competitive control to show the binding specificity. Cells were washed with HEPES buffer 2 times and then analysed using the flow cytometry machine FACS Canto II (BD). The change in LDV-FITC binding was calculated as MFI ratio == (MFI_{LDV-FITC+ SDF-1 α} – MFI_{unstained control})/(MFI_{LDV-FITC} – MFI_{unstained control}).

Confined migration assay in a microfluidic device

Confined migration assays were performed using a microfluidic device as previously described (Davidson et al., 2014). The device consists of alternating parallel migration channels of either 5 μ m height and constrictions of 1–2 μ m width (confined migration) or 5 μ m height and 15 μ m width (unconfined migration). Devices were assembled as previously described and coated with a solution of 10 μ g ml⁻¹ fibronectin 24 h before experiments (Keys et al., 2018). Four hours before imaging, 3×10^4 MSCs or cargoocytes were stained with Hoechst 33342 (1:4,000 v/v), then seeded into microfluidic devices and allowed to migrate along an FBS gradient (2–16.5%). Imaging was performed on a Zeiss LSM700 laser scanning confocal microscope with a $\times 20$ air objective. Cells and devices were imaged for 14 h at 10 min intervals in a temperature-controlled stage (37 C°). The time required for cells to migrate through an

individual constriction was quantified manually from images and was defined as starting at the first frame where the anterior portion of a cell entered a constriction and ending with the first frame after the cell posterior passed through the constriction.

Mouse model of acute inflammation in the ear

The LPS-induced model of dermal inflammation in the mouse pinna was established as previously described (Corradetti et al., 2017; O. Levy et al., 2013). Briefly, female BALB/cJ mice (8–12 weeks old) were anaesthetized with isoflurane (VetOne, MWI 502017) and injected with 30 µg LPS (Sigma Aldrich, L3024, in 30 µl saline) in the posterior/dorsal dermis of the right ear and 0.9% saline (Hospira NDC 0409-4888) in the control contralateral ear. After 6 h, mice were anaesthetized for i.v. injection (tail-vein or retro-orbital) of 1×10^6 MSCs or cargocytes, or PBS (vehicle control) in 100 µl solution.

For flow cytometry analyses, MSCs or cargocytes were stained with 10 µM Vybrant DiD (Invitrogen, [V22887](#)) following the manufacturer's instructions, before injection. Animals were euthanized 24 h after MSC or cargocyte injection. Ears were removed at the level of the base and the dorsal and ventral skin was peeled from the cartilage, then placed in 2 ml digestion buffer containing 0.1 mg ml⁻¹ DNase I and 0.2 mg ml⁻¹ Liberase TL (Sigma Aldrich, 5401020001) diluted in 1% FBS in RPMI media. After incubation at 37 °C for 1 h, ear skin was ground with a pestle in a 70 µm cell strainer (Biopioneer, DGN258368). When no large tissue pieces remained intact,

strainers were washed with 2 ml 1% FBS and 2 mM EDTA in PBS. Cells were then treated with 1X RBC lysis buffer (Biolegend, 420301) for 2 min, washed with PBS and stained with PE anti-mouse F4/80 Antibody and 7-AAD. Cells were analysed using the flow cytometry machine FACS Canto II (BD).

To monitor the biodistribution of i.v. injected cells, MSCs or cargoocytes were first transfected with firefly luciferase mRNA (Fluc mRNA) as described above.

Transfected MSCs or cargoocytes were plated in 96-well plates (10,000 per well, 100 μ l CCM media) and directly incubated with excess VivoGlo-luciferin (1.5 mg ml⁻¹, Promega, P1042) in CCM media for 10 min at 37 °C. Luciferase activity was then determined as RLU using SpectraMax M2e plate reader (Molecular Devices). In the biodistribution assay, mice were first treated with LPS as described above. For the 24 and 48 h time points, MSCs/cargoocytes were i.v. injected immediately after mRNA transfection; for the 2 h time point, MSCs/cargoocytes were cultured in 3D spinner flasks for 24 h after mRNA transfection and then i.v. injected. Mice were i.p. injected with VivoGlo-luciferin (1.5 mg per mouse, Promega, P1042) at indicated time points after i.v. injection. Mouse organs were subjected to bioluminescence imaging 15 min after i.p. injection using IVIS Lumina Series III (PerkinElmer). Because the perfusion of luciferin to the inflamed ears was not very efficient by this method, the dorsal skin of the ears was then peeled from the underlying cartilage and the subcutaneous surfaces of the tissue were directly soaked in VivoGlo-luciferin substrate (60 μ l at 15 mg ml⁻¹, Promega, P1042) and immediately subjected to bioluminescence imaging with IVIS Lumina Series III. For all IVIS imaging, exposure time was 5 min, binning

was medium, F/stop was 1.2, excitation filter was blocked and the emission filter was open.

CHAPTER 6 - EFFECTS OF NUCLEAR SIZE RECTIFYING COMPOUNDS ON CONFINED MIGRATION⁵

Abstract

Lower survival rates for many cancer types correlate with changes in nuclear size/scaling in a tumor-type/tissue-specific manner. Hypothesizing that such changes might confer a metastatic advantage to tumor cells, the Schirmer group at the University of Edinburgh aimed at the identification of commercially available compounds to guide further mechanistic studies. The Schirmer group screened for Food and Drug Administration (FDA)/European Medicines Agency (EMA)- approved compounds that reverse the direction of characteristic tumor nuclear size changes in PC3, HCT116, and H1299 cell lines reflecting, respectively, prostate adenocarcinoma, colonic adenocarcinoma, and small-cell squamous lung cancer. Upon finding distinct, largely nonoverlapping sets of compounds that rectify nuclear size changes in each tumor cell line, a subset of these compounds were identified as potential candidates for reducing the metastatic spread of cancers in a cell-type specific manner. Among these compounds were piperlongumine, an alkaloid which decreased the size of PC3 nuclei, and digitoxigenin, a Na⁺/K⁺ ATPase inhibitor, which specifically restored nuclear size in H1299 cells. Using a combination of microfluidic devices which mimic the confined migration environment, transwell assays, and wound-healing assays, we

⁵ Portions of this work have been adapted from the following publication
Tollis S, Rizzotto A, Pham NT, Koivukoski S, Sivakumar A, Shave S, Wildenhain J, Zuleger N, Keys JT, Culley J, Zheng Y, Lammerding J, Carragher NO, Brunton VG, Latonen L, Auer M, Tyers M, Schirmer EC. (2022) Chemical Interrogation of Nuclear Size Identifies Compounds with Cancer Cell Line-Specific Effects on Migration and Invasion. *ACS Chemical Biology* 18;17(3):680-700

Contributions: These results were primarily obtained through experiments performed by the Schirmer group. JT Keys performed and interpreted results from the microfluidic migration assay, and edited text prior to publication.

demonstrate that seven nuclear size-rectifying compounds inhibited cell migration and/or invasion. Our study provides (a) proof of concept that nuclear size might be a valuable target to reduce cell migration/invasion in cancer treatment and (b) the most thorough collection of tool compounds to date reversing nuclear size changes specific to individual cancer-type cell lines. Although these compounds still need to be tested in primary cancer cells, the cell line-specific nuclear size and migration/invasion responses to particular drug classes suggest that cancer type-specific nuclear size rectifiers may help reduce metastatic spread.

Introduction

Nuclear size has been recognized as a predictive marker for metastasis in multiple types of cancer (de las Heras et al., 2013). However, the relationship between nuclear size and metastatic risk varies between different cancers; in some cancer subtypes, larger nuclei correspond with increased metastatic risk, while in other cancers, smaller nuclei represent increased metastatic risk (de las Heras et al., 2013). While absolute nuclear size changes are used in current diagnostics, in some tumor types, the size change is associated with the disruption of cell scaling (Chen, 2010). In normal cells and tissues, the nuclear-to-cytoplasm (N/C) ratio is maintained during the cell cycle (Cavalier-Smith, 2005; Edens et al., 2013), throughout which the nucleus doubles in volume (Fidorra et al., 1981; Jorgensen et al., 2007; Neumann & Nurse, 2007). In contrast, the N/C ratio is altered in cancer cells by noncorrelated changes in nuclear size and/or cell size. Nuclear size is influenced by nuclear envelope proteins, such as the lamins that form the nucleoskeleton (Jevtić et al., 2015) and the outer nuclear membrane nesprins that connect to the cytoskeleton through the LINC complex (Lu et al., 2012).

As nuclear size or scaling is disrupted in cancer cells with increased metastatic potential, we reasoned that such changes might facilitate cell migration/invasion. As the nuclear envelope connects to both the genome and the cytoskeleton, nuclear size dysregulation could achieve this by altering gene regulation, signaling, and/or nucleocytoplasmic transport or by mechanical effects enabling faster migration and/or easier invasion of cancer cells through epithelial barriers. As the deformability of the

nucleus limits the ability of cells to migrate through narrow constriction (Davidson et al., 2014), it is possible that a reduction in nuclear size enables metastasis by improving the invasive ability of cancer cells (Lautscham et al., 2015). Indeed, disruption of lamin A, known to be limiting for nuclear size changes (Jevtić et al., 2015), reduces cell migration (Lee et al., 2007). Although there is also evidence to suggest that reduced lamin A expression also correlates with increased metastatic risk in breast cancer (Bell et al., 2021), indicating that factors beyond nuclear size, such as nuclear deformability, may also contribute to changes in the metastatic potential of cancer cells. Moreover, mechanical forces expected to be altered by nuclear size changes are important for the progress of metastasis (Wirtz et al., 2011) and cellular traction stresses are linked to metastatic potential (Kraning-Rush et al., 2012). Thus, we speculated that restoring nuclear size to a more normal range might reduce migration/invasion and thus metastatic potential, irrespective of the biological mechanism(s) that altered nuclear size control during carcinogenesis. We designed a proof-of-concept study to test this hypothesis and probe the chemical space in search of tool compounds that rectify cancer-associated nuclear size changes.

Here, we screened a Food and Drug Administration (FDA)/ European Medicines Agency (EMA)-approved drug library for compounds that rectify nuclear size in three distinct cancer cell lines derived from different tissues: two in which nuclear size increases correlate with worse-grade tumors (prostate, colon adenocarcinoma) and one in which nuclear size decrease correlates with worse-grade tumors (lung). Most compounds identified had cell line-specific effects on nuclear size or scaling, possibly

via indirect and pleiotropic mechanisms. Clustering compounds according to their therapeutic classes/mechanism of action identified many compound classes with characteristic nuclear size phenotypic signatures across cell lines and conditions. Detailed investigation of seven compounds revealed cell line-specific effects on cell migration and invasion that mirrored to a large extent nuclear size-rectifying effects, suggesting that their addition to treatment regimens might aid in combating metastatic cancer once animal testing has been completed.

Results

Chemical Compound Screening for Nuclear Size Rectifiers

We screened for compounds that alter nuclear size and/or N/C ratio in cancer cell lines representing three tumor types (**Figure 6.1**). PC3 and HCT116 cells, respectively, represented late-stage prostate cancer and colonic adenocarcinoma where nuclear size increases compared to the healthy tissues/early-stage tumors reflect worse cancer grades. H1299 cells represented small-cell squamous lung carcinoma, where decreased nuclear size correlates with a worse grade. The cells were treated with the Prestwick library of 1120 previously approved drugs (PADs) at 10 μ M for 6 h to reveal compounds that did not require postmitotic nuclear envelope reassembly to elicit size changes and for 36 h to identify compounds with low toxicity. To align with standard cancer diagnostic procedures, we used nuclear/cell area from imaging (focal) cross sections as our core size metric. The nuclear area was monitored with stably expressed H2B-mRFP, and cell area from CellMask DeepRed cytosol staining. A total of

350–1000 cells/conditions were imaged for each screen using a PerkinElmer OPERA confocal instrument.

For each cell line/compound/treatment duration condition, we calculated both absolute nuclear size and N/C ratio metrics for individual cells from high-content OPERA microscopy images (**Figure 6.1**, Methods section). The former is traditionally used by cytologists to grade tumors (Veltri & Christudass, 2014), while the latter identifies disruption of nuclear size scaling relative to cell size, a hallmark in certain cancer types (Chen, 2010). We next averaged these individual cell values, and also estimated the nuclear size variability (average- and outlier-based analysis strategies, respectively) across the cell population in each condition. We finally analyzed those datasets statistically to identify hit compounds that perturb absolute nuclear size and/or N/C ratio metrics beyond the typical metric variability across the library (Methods section), thereby reducing nonspecific compound effects on nuclear size. Hit compounds were confirmed using Wilcoxon rank tests versus in-plate DMSO controls. Comparing absolute and relative nuclear size (N/C ratio) metrics allowed us to identify compounds that affect the nuclear size in different ways, while the two analysis strategies enabled us to distinguish compounds with large effects on a fraction of the cell population (outlier-based) from those that uniformly affect most cells in the population (average-based).

Compounds that induced changes in average absolute nuclear size or N/C ratio in the direction opposite to that associated with increased metastasis in the corresponding

tumor type are referred to as nuclear size rectifiers (NSRs) throughout the manuscript. After 6 and 36 h of treatment, respectively, 88 and 124 compounds were NSR for the absolute nuclear size (**Figure 6.1A, left**), while 151 and 178 compounds were NSRs for the N/C ratio (**Figure 6.1A, right**). NSR compound sets for the absolute and relative nuclear size only partially overlapped, likely owing to compound-associated cell size renormalization. Likewise, compound sets aggravating cancer-associated nuclear size changes showed little overlap across cell lines and compound sets with effects after 6 and 36 h of treatment were also distinct (Tollis et al., 2022). Most NSRs were cell line-specific and only a few affected nuclear size in all lines (Tollis et al., 2022). Strikingly, a handful of compounds were NSRs for both PC3 and H1299 cell lines, or HCT116 and H1299 cell lines, despite rectifying nuclear size in both lines meant shifting the nuclear size in opposite directions. Notably, most NSRs had homogeneous effects on the cell population as opposed to large effects in a fraction of the population.

Several compound classes were NSRs in only one or two of the three cancer cell lines. Na⁺/K⁺ ATPase inhibitors, such as digitoxigenin, selectively increased absolute nuclear size only in H1299 cells and thus may exhibit selectivity toward lung cancer. Whereas piperlongumine, an alkaloid, decreased nuclear size in PC3 cells yet increased the N/C ratio (Tollis et al., 2022). Thus, just as nuclear size changes are characteristic for each tumor type, many compounds that rectify these defects are often specific to each cell line representing these tumor types and exert distinctive effects on relative and absolute nuclear size metrics.

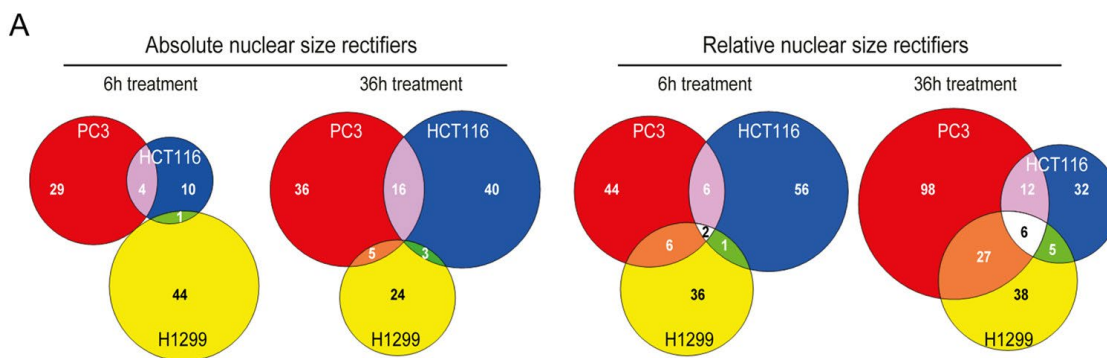


Figure 6.1. Tumor/tissue-type-specific effect of NSR compounds. Colored regions on Venn diagrams show the number of hit compounds for PC3 (red), HCT116 (blue), and H1299 (yellow) tumor cell types. (A) Overlap in absolute nuclear size rectifiers (left) and N/C ratio rectifiers (right).

Reversal of Nuclear Size Defects Reduces Cancer Cell Migration

To investigate potential cell line-specific effects of NSRs on migration, we next tested the seven selected compounds at concentrations from 1 nM to 10 μ M in a scratch-wound healing assay (**Figure 6.2A,B**). PC3 and H1299 cells were analyzed as several compounds were unique NSRs for each.

Analysis of PC3 wound closure after 24 h incubation revealed that the PC3 NSR piperlongumine (**Figure 6.2A**) reduced migration in a dose-dependent manner at concentrations starting at 100 nM or 1 μ M, concentrations at which piperlongumine was a NSR for this cell line. Strikingly, digitoxigenin (an H1299-specific NSR that does not affect nuclear size in PC3), did not affect migration at any concentration (**Figure 6.2A**), in full agreement with our working hypothesis.

Effects in the wound healing assays could reflect reduced mobility or loss of directionality or both. After a scratch wound, normal cells orient with the centriole facing the wound to direct inward migration and wound closure. To test for loss of cytoskeletal polarization, the cells were stained for γ tubulin to determine centriole orientation. Piperlongumine, digitoxigenin, and oxyphenbutazone, a nonsteroidal anti-inflammatory drug which also reduces nuclear size in PC3 cells, were tested in PC3 cells and each yielded defective centriole orientation in 65–85% of cells scored (**Figure 6.2B**). Hence, the 3 compounds tested altered the directionality of cell motion, making this parameter unlikely to explain why piperlongumine and oxyphenbutazone slow down wound closure while digitoxigenin did not.

We next considered the possibility that compound effects on nuclear size might reverse an advantage of the tumor cells to migrate through tight junctions, as a means of modeling the initial invasion step of cancer metastasis. We tested PC3 migration through 5×15 (“unconfined”) and $5 \times 2 \mu\text{m}^2$ (“confined”) constrictions, the latter requiring substantial nuclear deformation, while the former exceeding the size of the nucleus and thus partly serving as controls for migratory ability in a three-dimensional (3D) environment (**Figure 6.2D**). The mean migration speed through the $5 \times 15 \mu\text{m}^2$ constrictions was slightly slower for piperlongumine-treated cells (79 min) versus DMSO solvent control (91 min). Similarly, digitoxigenin-treated cells exhibited a slightly slower mean migration through the smaller $5 \times 2 \mu\text{m}^2$ constrictions (73 versus 82 min for controls). However, in both cases, the differences were not statistically significant (two-tailed t-test $p > 0.05$). In regard to compound-induced centriole

orientation defects but minimal 3D migration defects, the compound-induced slower wound closure suggests that tested NSRs affect specifically two-dimensional (2D) cell polarization/mobility rather than mechanical stiffness as cells preferentially use these two distinct mechanisms, respectively, for 2D vs 3D migration (Brunner et al., 2006; Davidson et al., 2014; Lautscham et al., 2015). A transwell migration assay was also performed (**Figure 6.2C**) to investigate compound effects on PC3. Cells treated with piperlongumine and parabendazole, which increased nuclear size in all cell lines tested, had ~50% fewer cells migrate through the Boyden chamber membrane compared to DMSO-treated controls, where oxyphenbutazone and digitoxigenin reduced the invasion capability by 15 and 30% respectively (**Figure 6.2C**). Thus, NSR compounds reduced both cell migration and invasion in tissue culture assays, although the cell line specificity of migration phenotypes mirrored the cell line specificity of NSR phenotypes to a larger extent in wound healing assays.

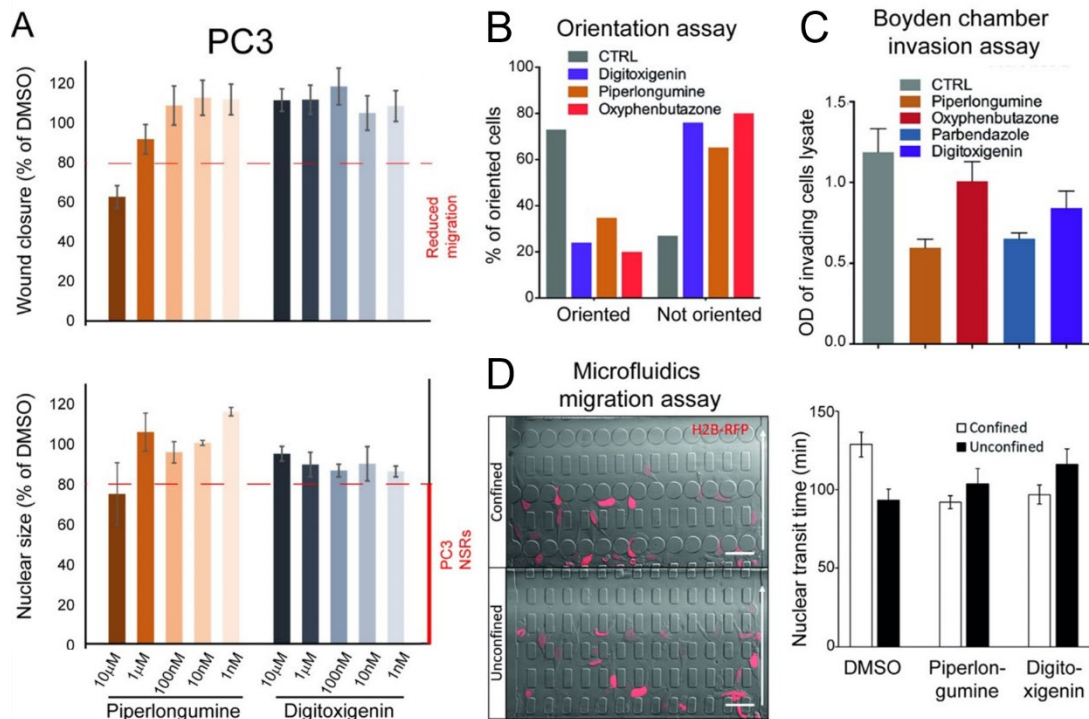


Figure 6.2. NSR compounds affecting nuclear size also affect cell migration and invasion. (A) Wound healing assay. Wound confluence (top row) and average nuclear size (bottom row) for PC3 cells treated with varying concentrations of piperlongumine or digitoxigenin (from left to right) as indicated, in % of DMSO-treated control cells. Red dashed lines represent cutoff values for strong reduction of migration (top row) and strong NSR phenotype (bottom row) (B) Orientation assay. Percentage of PC3 cells from panel (A) showing correctly oriented (left bars) or mis-oriented (right bars) centrioles, after 12 h of wound closure in the presence of 10 μ M of indicated compounds, as assessed using γ tubulin staining. (C) Invasion assay. Optical density (OD, arbitrary unit) characterizing the fraction of PC3 cells that successfully invaded a Boyden chamber within 24 h, in the presence of 10 μ M of the indicated compounds. (D) Microfluidics migration assay. (Top) Representative images of cells migrating in the microfluidics chamber through confined ($\leq 2 \mu\text{m} \times 5 \mu\text{m}$, top) and unconfined ($15 \mu\text{m} \times 5 \mu\text{m}$, bottom) constrictions. Arrow shows migration direction. Scale bar, 50 μm . (Bottom) Mean

nuclear transit time (time required to move through an individual constriction) for DMSO-, piperlongumine-, and digitoxigenin-treated PC3 cells. Error bars show SEM.

Discussion

Our findings demonstrate the viability of NSR compounds as prospective therapeutic agents which may reduce the metastatic ability of cancer cells. As nuclear size defects are recognized as predictive measures of metastatic potential (de las Heras et al., 2013), it is therefore reasonable that reversing these defects may reduce the incidence of cancer metastasis.

The relationship between nuclear size and metastatic potential is not uni-directional, and varies between different cancer cell lines. This is because nuclear size is impacted by many intrinsic biological factors within an individual cell, some of which have related impacts on cell's migration ability. Reductions in nucleo-cytoskeletal tension or actomyosin contractility may reduce the ability of cells to translocate their nuclei through constrictions (Davidson et al., 2020), regardless of their associated reduction in nuclear size. Meanwhile, reduced lamin A expression corresponds with increased nuclear size, and also leads to increased metastatic risk as a reduction in nuclear deformability (Bell et al., 2021). Therefore, nuclear size does not independently provide a thorough mechanistic explanation for how individual cells have become more metastatic. However, as correlations between nuclear size and metastatic risk are commonly observed, changes in nuclear size may be indicative of related defects which may more directly impact metastatic risk (**Figure 6.3**).

By screening an FDA/EMA-approved drug library for compounds that rectify cancer-associated nuclear size defects in three different cancer cell lines where nuclear size increase or decrease correlates with worse-grade tumors, we anticipate that the mechanistic understanding of approved drugs and their easy commercial accessibility will facilitate rapid follow-up research based on our discoveries.

While we have not yet proven a causal relationship between the nuclear size change and altered migration, we identified 50– 100 NSRs for each cancer cell line, many of which showed cell line-specific NSR activity and have not been previously tested for cancer therapies for the tumor types represented in our screens. We selected seven of these NSRs for detailed investigation, all of which reduced cell migration under most conditions (cell line, concentration), where they also rectified nuclear size. Hence, the simple nuclear size readout appears to be a reasonable predictor of the effect of drugs on cell migration, irrespective of whether these drugs have pleiotropic effects or impinge on nuclear size and/or migration via many indirect mechanistic routes.

Notably, the microfluidic cell invasion assay did not correlate as strongly with nuclear size correction as the cell migration assays. While this discrepancy could be attributable to technical aspects (differences in treatment duration, effective compound doses on cells in the two very different assay systems, etc.), it could also stem from different compounds targeting different aspects of cell migratory behavior. For example, it is possible that cells migrating through microfluidic constrictions utilized

migration mechanisms, such as an amoeboid migration mode, which are less conducive to movement through Boyden chambers or in wound healing assays. Such mechanisms may not be effectively targeted by these NSR compounds. It will be important to test NSR compounds in a variety of assays, in primary tumor cells, and in xenograft models, mouse models, or 3D collagen matrices in order to better understand if they effectively reduce cell migration in more biologically accurate environments. These further studies, which may help to pinpoint the precise mechanism by which these compounds inhibit migration, are required before considering these compounds further for clinical use on cancer patients.

This study provides evidence that therapeutic agents which reverse nuclear size defects may help to reduce the risk of cancer metastasis. By providing a broad screen of prospective compounds, these findings provide an avenue of further investigation for compounds which rectify nuclear size and reduce cell migration in a cell-type specific manner. The cell type specificity is significant as it suggests limited off-target toxicity when using these compounds as a part of a combination therapy. Though these findings do not provide a mechanistic explanation of how these treatments reduce cell migration, we believe that these results provide a proof-of-principle for identifying potential metastasis-targeting compounds based on their effect on nuclear size.

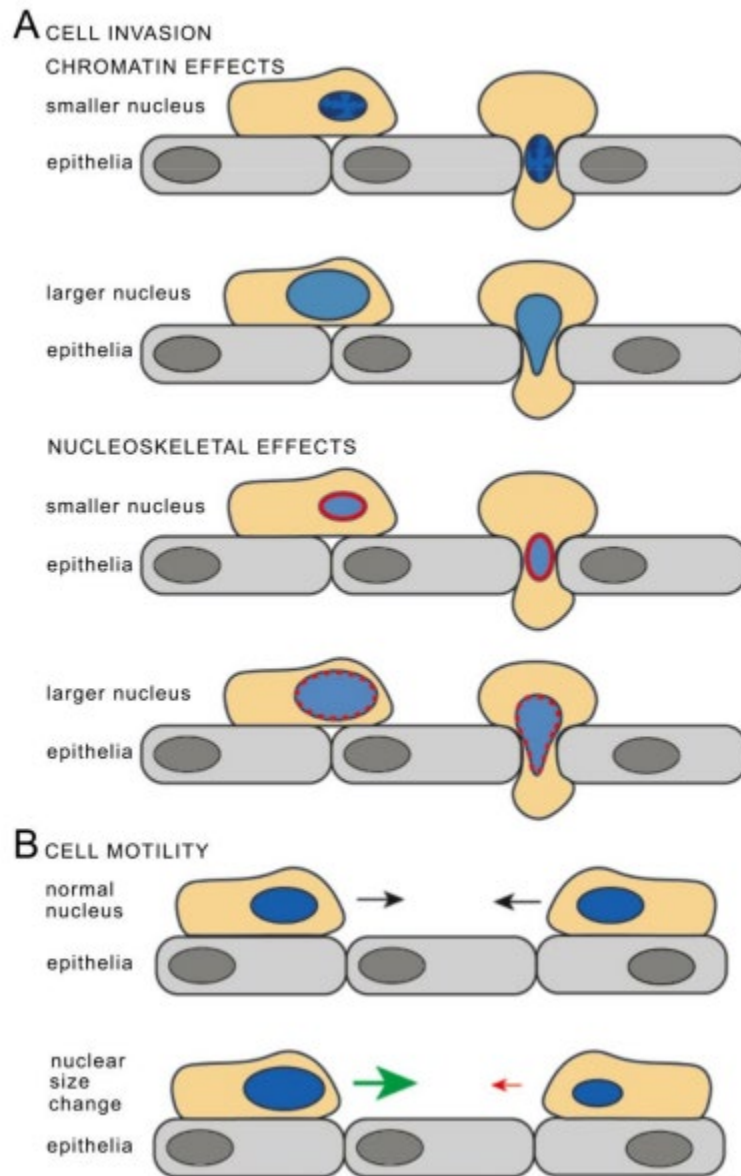


Figure 6.3. Model for how nuclear size changes may affect cancer cell invasiveness. **A** Chromatin effects on nuclear size and stiffness (top). For cell invasion through an epithelial layer, condensation of chromatin in a smaller nucleus could allow facile transit through a tight junction while looser chromatin in a larger nucleus could make the nucleus more malleable and also facilitate transit through a tight junction. Nucleoskeletal effects on nuclear size and stiffness (bottom). Reduced lamin A production might result in a softer nucleus that could

squeeze through tight junctions. Conversely scaling defects that cause a larger nucleus with lower lamin density would be more malleable to facilitate tight junction transit. **B** Cell motility may also be affected by nuclear size. Altered connections between the nucleoskeleton and cytoplasmic filaments in cells with larger or smaller nuclear size may influence cell mobility.

Methods

Cell Lines

PC3, HCT116, and H1299 cells were stably transfected to express H2B-mRFP in the pEGFP-N2 clontech vector and maintained under G418 selection (500 µg/mL) for general culture. Selection was removed for one passage prior to plating for experiments to avoid drug interference effects

Cell Culture and Manipulation

The Prestwick compound library (PAD, 2015 version) was contained in fourteen 96-wells plates, each of which consists of 80 drugs mostly approved by the FDA and EMA agencies (1 mM stock concentration in DMSO) and 16 in-plate DMSO controls, for a total of 1120 compounds. For each screen, ~5000 H2B-mRFP tagged cells were plated on each well of 14 Greiner Screenstar 96-wells glass-bottom imaging plates and left overnight in 99 µL of Roswell Park Memorial Institute (RPMI) medium for adhesion and growth prior to compound treatment (addition of 1 µL of stock to a final well concentration of 10 µM). The cells were incubated for 6 or 36 h before

preparation for imaging. Cell densities prior to compound treatment were adjusted to account for cell doubling during the 36 h long-term treatment to minimize differences in cell densities at the time of imaging. The cells were fixed in 3.7% EMD FX0410-5 formaldehyde solution for 15 min at room temperature, washed with phosphate-buffered saline (PBS), and then incubated for 30 min in 50 μ L of HCS CellMask DeepRed 0.5X (Molecular Probes) for cytosol staining. Stained fixed cells were washed again and stored in PBS at 4 °C. Plates were wrapped in parafilm and aluminum foil and imaged within 1 week.

Wound Healing Assay

Approximately 25 000 cells per well were seeded on Sartorius 96-well LockView or ImageLock microplates (Sartorius AG) the night prior to wound formation. The cell monolayer was scratched with the IncuCyte WoundMaker that simultaneously makes equivalently sized scratch wounds in the monolayer in all wells, and the medium was replaced with a compound-containing medium supplemented with 1% fetal bovine serum (FBS) to induce cell migration and reduce cell proliferation. Serial dilutions (1 μ L) of the compounds in DMSO were added to obtain the 1 nM to 10 μ M final concentrations, and the plate was mixed gently. The plates were placed in the IncuCyte incubator and imaged in a bright field with a 10 \times objective every 3 h for 48 h. Analysis of the wound confluence and width was performed with an automated script in IncuCyte 2021C software provided by Sartorius.

Microfluidic Migration Assay

PC3 cells were seeded into microfluidic chambers consisting of migration channels with a fixed height of 5 μm and constrictions of 1–2 or 15 μm in width, coated with a solution of 5 $\mu\text{g}/\text{mL}$ of fibronectin 24 h prior to experiments as described previously. (Davidson et al., 2014; Keys et al., 2018) A total of 30 000 cells were seeded into each device 6 h prior to imaging and were treated with 10 μM piperlonguine, digitoxigenin, or equivalent DMSO. Imaging was performed on a Zeiss LSM700 laser scanning confocal microscope with a 20 \times air objective. The cells were imaged at 10 min intervals in a temperature-controlled stage (37 $^{\circ}\text{C}$) for 14 h. The time required for cells to migrate through an individual constriction was quantified using a previously described MATLAB script for measuring nuclear transit through these microfluidic devices (Elacqua et al., 2018).

Invasion Assay

The QEM endothelial cell invasion assay was carried out in accordance with manufacturer's recommendations (ECM210, Millipore). The cells were seeded at a concentration of 10^5 on the inside Boyden chamber in the absence of FBS on a 3 μm pore membrane coated with ECM proteins and submerged on the outside Boyden chamber in the presence of conditioned media and 10% FBS as chemoattractant. The cells were allowed to migrate through the membrane for 24 h in the presence of compounds at the 10 μM concentration used in the size screen, prior to fixation and staining of the lower part of the membrane. Noninvading cells were removed with a cotton stab from the top of the membrane, and the cells were lysed. Absorbance values

of the cell lysate were analyzed on a microplate reader (JASCO V-550) with a 540 nm wavelength, to quantify the relative number of migrating cells by colorimetry.

Imaging Data Acquisition

H2B-mRFP tagged cells were imaged using an Opera High-Content Screening instrument (PerkinElmer), equipped with a 20× air objective (LUCPLFLN, NA = 0.45) and Peltier-cooled charge-coupled device (CCD) cameras, or with the latest Opera Phenix for the 6 h time point in H1299, for technical reasons. H2B-mRFP (nucleus) and CellMask DeepRed (cytosol) fluorochromes were exposed sequentially at 561 and 640 nm for 320 and 200 ms, respectively, and fluorescence was measured on distinct channels with 600/40 and 690/70 bandpass detection filters. Bleed-through of the cytosolic channel into the nuclear channel was negligible. For each well, 20 fields of view (FOVs) were acquired, avoiding the edge of the well where cells accumulate due to capillary action. The drug incubation time was set to 24 h. Only six cells were scored with 10 μ M astemizole treatment in this replicate experiment, making an accurate estimation of average nuclear size impossible under this condition. For this compound, these missing data have been replaced by the data from the original screen, averaging the data from 6 and 36 h to interpolate treatment duration (although the nuclear size was reduced very similarly after 6 and 36 h astemizole treatment).

Data Processing and Quantitative Analysis

An adapted Acapella (PerkinElmer) software script was used to automatically mask the cytoplasm and nucleus of individual cells within each FOV. Cell and nuclear sizes were, respectively, defined as the areas (in pixels) of the masked regions in the focal plane, based on, respectively, the CellMask DeepRed and H2B-mRFP signals. Intensity threshold filters, size filters, and morphological filters (which threshold on cell/nuclei size, nuclear roundness, width-to-length ratio, distance between nuclei) were used to filter out detection artifacts, multiple detections of single cell/nuclei, or unique detection of cell clusters. Identical processing parameters were used in Acapella for all conditions to prevent postacquisition processing biases. Single-cell data were exported to a .txt file for subsequent analysis in MATLAB (The Mathworks)

Data Filtering and Computation of Nuclear Size Metrics

For conditions that yielded higher cell densities at the time of imaging, the above filtering step was sometimes insufficient to remove clusters of cells so cell size outliers were eliminated from all datasets. For each condition separately, the entire cell size distribution was analyzed, and we extracted the 25, 50, and 75 size quartiles (Q1, Q2, and Q3, respectively). Next, we filtered out detection areas with a size larger than the standard outlier threshold $Q2 + 6 \times (Q3 - Q2)$ (i.e., likely cell clusters), and the detections smaller than $Q2 - 6 \times (Q2 - Q1)$ (i.e., imaging artifacts or cell debris). All DMSO control wells for each plate were processed together in this step. For each cell that passed filtering, we computed two metrics: the absolute nuclear size N , and

the relative nuclear size, or N/C ratio, defined as the ratio of the absolute nuclear size to the absolute cell size.

Hit Confirmation

Hits were confirmed by computing direct compound-vs-DMSO Wilcoxon rank tests, where the multiple well-averaged values of the metric across all DMSO and compound replicates were used to perform the tests. Reported p-values account for variability between plates in well-averaged metric values from both DMSO and compound treatments.

Statistical Analysis of Compound Class Enrichment for Phenotypes of

Interest—Class Enrichment Scores

The analysis above revealed clustering of particular compound classes with consistent absolute nuclear size and/or N/C ratio phenotypes across the set of cell line/treatment duration/replicate conditions. To estimate the statistical significance of compound class enrichment for any given phenotype, we performed individual compound-vs-entire library Wilcoxon rank tests using data from all replicates. The Wilcoxon p-values obtained from these tests indicate whether a given compound produces the phenotype significantly above the typical level in the library. Compounds showing p-values lower than 0.05 were counted for the entire library (1120 compounds in total) and for each of the particular drug classes identified by the heat maps, i.e., β adrenergic receptor agonists (15 compounds), DNA intercalants (5), replication inhibitors (5), glucocorticoids (26), MAP kinase inhibitors (2), microtubule poisons

(9), Na⁺/K⁺ ATPase inhibitors (5), 5-HT (serotonin) uptake inhibitors (8), cyclo-oxygenase inhibitors (48), detergents-surfactants (11), antineoplastic agents (25), β adrenergic antagonists (14), and GABA receptor ligand and stimulants (8 compounds). For each class of compounds (encompassing n compounds), the probability that the number k of compounds scored with $p < 0.05$ is not related to their therapeutic class equals the probability to randomly pick k active compound within a group of n and is given by the hypergeometric law $H(N,m,n,k)$ with parameters $N = 1120$ and $m =$ total number of active ($p < 0.05$) compounds for this particular phenotype. Thus, the probability that the compound class is statistically relevant to the observed pattern is $1 - H(N,m,n,k)$ and defines the class enrichment scores (given in %). All compound classes showing characteristic patterns on the heatmap were statistically significant, with class enrichment scores larger than 95%, and often 99%. For antineoplastic agents, class enrichment scores were computed the same way, with the exception that active compounds for all phenotypes were gathered. Using a similar approach for Cox inhibitors yielded a class enrichment score of 93–94% for both the average absolute nuclear size and N/C ratio.

CHAPTER 7 – CONCLUSIONS AND PERSPECTIVES

Collectively, this work has expanded the understanding of how intracellular forces interact with the nucleus during confined migration. We developed a platform which enables the study of nuclear mechanics during confined migration, and demonstrated its utility in several studies which model the implications of nuclear mechanics in health and disease (Chapter 2, 3, 5, 6). Using a variety of approaches to probe intracellular mechanics, we revealed a novel mechanism by which cells push their nucleus forwards through contraction of the rear cortex (Chapter 3). Using the same laser ablation assay which I developed to study nuclear transit mechanisms, I helped to demonstrate the impact of intracellular pressure in the rear compartment of migrating cells on nuclear blebbing (Chapter 4). My work on the migration of enucleated cells demonstrated that cells have the capacity to migrate through 3D environments in the absence of a nucleus (Chapter 5). By investigating the effect of reversing nuclear size defects on confined migration, I helped to demonstrate that reversing nuclear size defects may impair the ability of cells to squeeze their nucleus through constrictions (Chapter 6).

In demonstrating the utility of the cortex-driven nuclear transit mechanism in confined migration, my work has opened an avenue for developing novel therapeutic targets for preventing cancer metastasis. Future works should investigate the precise biological signaling pathways which drive the selection of a cortex-driven nuclear transit mechanism. While we were able to determine that this mechanism required ROCK

activity for cortical localization of actin and myosin II (Chapter 3), ROCK is also required for alternative mechanisms of nuclear transit, such as previously identified “pulling” mechanisms (Davidson et al., 2020). The overlap of these mechanisms does support the potential utility of targeting ROCK as an avenue for preventing cancer metastasis (Vennin et al., 2020). Intriguingly, however, we also found that ROCK-mediated contraction of the rear cortex led to nuclear blebbing (Chapter 4). Recent work has shown that nuclear blebbing and rupture may have downstream consequences on genomic stability and cell viability (Denais et al., 2016; Shah et al., 2021; Xia et al., 2018). It is therefore unclear whether or not ROCK-inhibition of cancer cells would also provide a protective effect to these cells if it also consequently reduces the incidence of nuclear blebbing and rupture. Further studies will be necessary which observe the long term effects of ROCK-inhibition on cancer cells following prolonged periods of confined migration.

Though we found that ROCK was required for the novel cortex-driven pushing mechanism, uncovering the specific biological drivers of each of these independent nuclear transit modes will be beneficial as it may present additional unrecognized targets for therapy. For example, as “pulling” mechanisms are understood to require physical connections between the nucleus and cytoskeleton through LINC-complex proteins (Davidson et al., 2020), developing agents which target the LINC complex could reduce the migration of these cells. However, if LINC complex inhibition switches cells to a cortex-driven nuclear transit mode, then these cells may still be able to metastasize. Identifying pathways which enable the cortex-driven nuclear transit

mode, perhaps through knockdown of proteins which enable association between actin filaments and the cell cortex (such as Ezrin), may provide options for combinatorial cancer therapies; a dual targeting strategy which inhibits “pulling” via LINC complex interference and inhibits “pulling” through disruption of the rear cortex.

Additional work is necessary to further clarify the role of the LINC-complex in nuclear transit during confined migration. Our findings in collaboration with the Konstantopoulos group on HT1080 cells migrating through channels showed that nuclear positioning towards the cell rear and formation of nuclear blebs required LINC complex connections, indicating that the nucleus was anchored towards the rear of the cell (Chapter 4). These findings suggested that the anchoring of the nucleus to the rear enabled the increase of pressure in the rear compartment of the cell. This hypothesis would however be contradicted by our laser ablation studies in MDA-MB-231 cells, where ablation of the cell rear led to rearward movement of the nucleus (Chapter 3). If the nucleus were tethered to the cell rear, it would be expected that ablation of the cell rear would eliminate these tethers, enabling forward movement of the nucleus. It is likely that part of what leads to the difference in these findings could be environmental. In the studies using HT1080 cells, cells migrated along long narrow channels, while the MDA-MB-231 cells were migrating through shorter, more narrow constrictions which trapped the nucleus at a point. It is possible that in longer channels, the nucleus becomes anchored to the cell rear via the LINC complex, while the round, singular constrictions may be sufficient to cause rearward anchoring of the nucleus in the absence of the LINC complex. Future studies which replicate these

studies using other cell lines with or without LINC complex depletion will be necessary to clarify the mechanism which drives cortex-driven pushing of the nucleus.

Our work with the Klemke group showed the potential viability of cargocytes as a platform for highly-targeted drug delivery to diseased tissue (Chapter 5). We demonstrated that enucleated cells can migrate in the absence of the nucleus in multiple different 3D migration assays, overturning an earlier understanding that the nucleus is required for 3D migration (Khatau et al., 2012; Petrie et al., 2014). These findings are important in the context of this study, as it demonstrates how these cargocytes will be able to undergo transendothelial migration and enter diseased tissue in order to deliver therapeutic cargo. The removal of the nucleus is essential here, as it ensures that these engineered cells do not retain their capacity to divide following injection, and will therefore die-off after homing to sites of inflammation. This work demonstrates that engineered cargocytes overcome many limitations that prevented the translation of other bioinspired drug delivery systems into clinical applications.

Our work in collaboration with Eric Schirmer's group led to the finding that treatment with compounds which reverse nuclear size defects in cancer cells leads to defects in migration (Chapter 6). The principal limitation of this study was in its inability to pinpoint a specific mechanism by which these compounds led to these observed migration defects. The role of nuclear deformability in limiting confined migration is well established, and in some cases, increased nuclear size may also reduce deformability (Davidson et al., 2014; Lautscham et al., 2015). However, changes to

adhesion, contractility, nesprins expression, and lamin A expression can all lead to changes in nuclear size which also have unrelated impacts on cell migration machinery (Bell et al., 2021; Edens et al., 2013; Jevtić et al., 2015; Lu et al., 2012; Neumann & Nurse, 2007). This could explain the incongruity between our findings on cell migration in different assays. Though migration was reduced following treatment with nuclear size rectifiers in wound healing assays or Boyden chambers, we did not observe the same migration defects in cell migrating through microfluidic constrictions (Chapter 6). The proof in principle, however, that these compounds led to reduced migration of cancer cells in a cell-type-specific manner has significant implications in their potential for use as metastasis-targeting therapy. Further works will be necessary for each of the identified compounds in order to demonstrate that they can inhibit metastasis *in vivo*, that they display the same cell-type specificity which can reduce side effects, and to identify the precise mechanism which enables its action.

In summary, my graduate work has contributed to considerable advances in the understanding of the interplay between intracellular forces and nuclear mechanobiology during migration through 3D environments. Through the application of microfluidic devices which model the *in vivo* confined migration environment, we demonstrated a novel mechanism for nuclear transit through constrictions, identified prospective compounds for future metastasis-preventing therapies, and showed that cells could migrate through 3D constrictions in the absence of a nucleus. Our collective works studying cancer cells will inform future studies which will identify

new treatments for the prevention of cancer metastasis. Our findings on enucleated cell migration will both inform the understanding of how cells are able to migrate through 3D constrictions, independent of a nucleus, and provides evidence that cargocytes may represent a novel vehicle for drug delivery.

APPENDIX A: NUCLEAR POSITIONING IN HL-60S DURING CONFINED MIGRATION

Abstract

Cell polarization is an essential step in the migration process. During polarization, cells position intracellular components, including the nucleus and microtubule organizing center, in order to facilitate actin polymerization at the leading edge and retraction of the cell rear. In HL-60 human leukemia cells, it has been observed that cells may alter how the nucleus is positioned within the cell during migration, depending on the degree of extracellular confinement. Here, we report evidence that rearward positioning of the nucleus in HL-60s is a result of increased nuclear stiffness and decreased ROCK-mediated contractility.

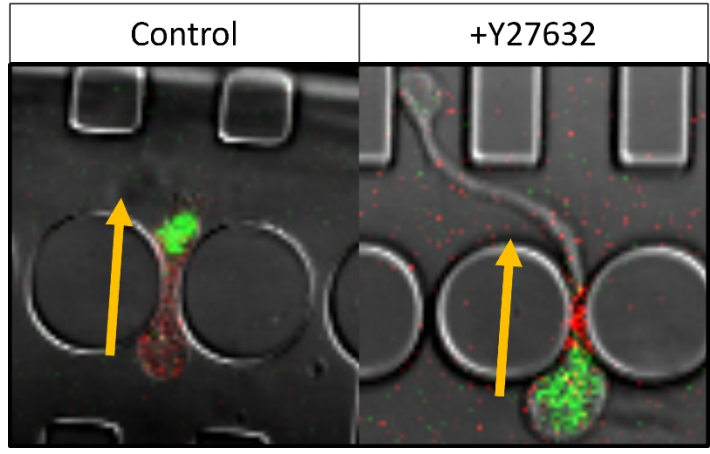
Introduction

During typical cell migration, cells become polarized with a front to rear axis. In many cells, this axis requires rearward positioning of the nucleus with the microtubule-organizing center positioning in front of it. However, in some amoeboid cell lines, cells are able to migrate with their nucleus at either the leading or trailing edge, depending on the environmental context. Recent results have indicated that HL-60 cells position their nucleus at the leading edge during 3D migration, but this positioning is altered during migration through constrictions narrower than the cell nucleus (Renkawitz et al., 2019; Yadav et al., 2018). These findings also indicated that rearward nuclear positioning was more common as a result of increased nuclear stiffness (Yadav et al., 2018). We hypothesized that this was a result of insufficient

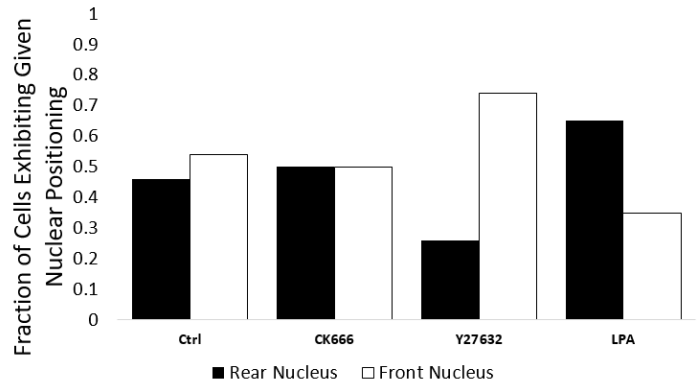
intracellular force generation; causing the nucleus to get “stuck” behind constrictions. To determine whether this was the case, we utilized HL-60 cells and modified them to express mCherry-Actin and mNeonGreen-H2B Histone. This allowed for the visualization of both the cell body and nuclear positioning during migration through microfluidic constrictions. Through treatment with the ROCK inhibitor, Y27632, we found that reduced actomyosin contractility led to rearward positioning of the nucleus and significantly increased nuclear transit times (**Figure A.1**). To contrast these results, we used LPA to increase actomyosin contractility, and found that these cells completed nuclear transit with the nucleus first more often, though we did not detect a change in nuclear transit times through constrictions (**Figure A.1**, middle and bottom). CK666 treatment was used to detect whether actin polymerization played a significant role in nuclear transit or positioning, though no effect was detected (**Figure A.1**, middle and bottom).

We sought to follow these results up with experiments that detected if there was a significant interplay between nuclear stiffness and actomyosin contractility in dictating nuclear positioning during nuclear transit. To do this, we transfected HL-60 cells with GFP-Lamin A, to overexpress the Lamin A protein and increase nuclear stiffness. Previous results with this construct indicated that increased Lamin A expression led to rearward nuclear positioning during transit through constrictions (Yadav et al., 2018). By treating these cells with LPA, we hypothesized that the increased contractility would reverse this effect, “rescuing” the normal nucleus-first migration phenotype.

However, these experiments were stalled during prolonged periods of failed troubleshooting while working with HL-60 cells. Cells often did not survive differentiation with the standard 4 day retinoic acid protocol. When they did survive, they failed to migrate within microfluidic devices in response to chemotactic gradients, as they had in the initial pilot experiments, outlined above. It is unclear what caused these changes in the behavior of cells. Retinoic acid, fMLP chemoattractant, and fibronectin stocks were all replaced to ensure that reagents were sufficiently fresh. Multiple re-thawings of HL-60 cells were performed to detect whether individual cell lines were problematic. None of these troubleshooting approaches resulted in successful experiments, and thus, findings along this subject were not followed up.



HL60 Nuclear Positioning During Confined Migration



HL60 Nuclear Transit Times

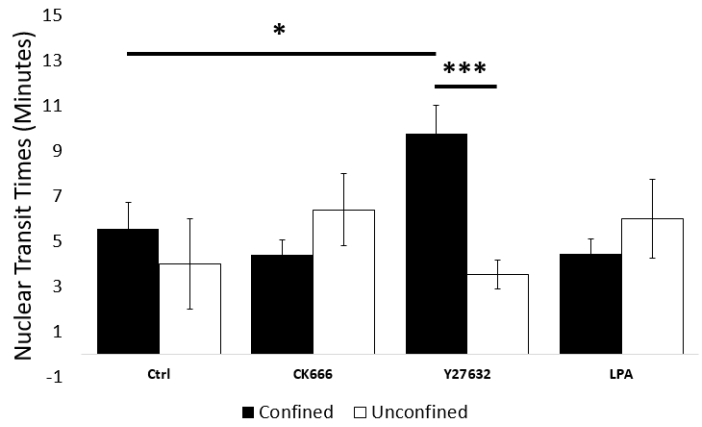


Figure A.1: HL-60 nuclear positioning is altered through reduced actomyosin contractility. (Top) HL-60 cells migrating through microfluidic constrictions following treatment with vehicle control (DMSO) or Y27632 (Red:Actin, Green: H2B Histone).

(Middle) Proportion of cells migrating with nucleus at the cell rear or cell front during nuclear transit. (Bottom) Nuclear transit times of cells in confined microfluidic constrictions or unconfined channels. Error bars represent SEM. *: $p < 0.05$, ***: $p < 0.001$ from two-tailed t-test

APPENDIX B: TEACHING AND OUTREACH

Abstract

As a supplement to my research, my involvement with teaching and outreach programs at Cornell was a major component of graduate school experience. Working with Cornell Adult Online University's (CAU) Teen and Youth Program, the CURIE Academy, Girl Scout Engineering Day, and the Engineering Learning Initiatives group, I developed a teaching philosophy centered around ensuring classroom equity and inclusion for all students. This philosophy emphasizes structured group work and enabling regular intervals of direct engagement with learning materials. Working with CAU's Teen and Youth Program, I was able to test some of these concepts in an online, flipped classroom environment. Here, I detail the basis of my teaching philosophy in prior pedagogical research, and report my findings from teaching CAU classes, and how I believe my methods could be improved while teaching future courses.

Introduction

The decision to pursue a career in STEM is one made quite early in a person's life. The factors which go into that decision are multivariate, and can be traced to many sources, including one's aptitude for math and science during early education, following in the footsteps of role models (often their parents), and how well they are exposed to science at a young age (Archer et al., 2012; Dewitt & Archer, 2017; Sadler et al., 2012). Of the latter of these factors, access to quality science education varies considerably between students of different geographical location and socio-economic

backgrounds (Ahmed, 2018; Archer et al., 2012; Godec et al., 2022). This access is of particular importance in considering students of lower socio-economic status, as careers in STEM are among the most economically lucrative, and therefore can provide a vehicle for vertical social mobility (Habig et al., 2020). Alas, due to the differences in access to STEM education at a young age, STEM professions are often populated by those coming from middle to upper middle-class backgrounds. This not only represents an issue of economic class, but also perpetuates racial disparities in STEM professions, which contributes to ongoing racial inequalities in terms of both income and social mobility (Chen, 2013). To address these inequalities, it is incumbent upon leaders in STEM education to reach out and encourage students to pursue opportunities in STEM.

Promoting diversity in STEM has been an important focus of mine throughout my academic career. While I cannot claim to have experienced exclusion or a lack of representation for my own identity in my field of study, it is undeniable that a legacy of discrimination still lives on in STEM education at the university level which remains overwhelmingly white, straight, cis-gendered, able-bodied, and male (Chen, 2013). This legacy is grounded in and driven by multivariate factors, including class immobility, racial discrimination, and conservative societal attitudes about what scientists “should look like”. Accordingly, progress towards a wholly inclusive culture in STEM can seem sluggish. To ameliorate these issues, it is imperative that we, as academics, make conscious efforts to create a more welcoming community for groups who are historically underrepresented in STEM.

Using Active Learning to Foster Inclusivity in the Classroom

Promoting diversity in STEM is not only important through acts of inclusion and outreach, it also must play a role in how we approach our teaching. One simple way to accomplish this is to actively incorporate elements of antiracist pedagogy, and to ensure best practices are followed by closely following educational literature on the subject. For example, research suggests that adopting a highly structured course design and active learning approaches can help to reduce the achievement gap faced by underrepresented minority students in STEM education (Haak et al. 2011; Theobald et al. 2020). I believe these types of approaches can easily be applied into any STEM curriculum, as emphasizing active learning in the classroom is both an excellent way to facilitate inclusion of all students in the class, and better reflects the practice of engineering in industry than more didactic, teacher-centric, lecture-based approaches.

As a Graduate Teaching Assistant (TA) Development Consultant, I worked with Cornell's Engineering Learning Initiatives (ELI) group to produce workshops to instruct the department's TAs on how to incorporate evidence-based practices for promoting inclusive, active learning into their teaching. These workshops engaged students through exercises which helped to familiarize students with (1) active learning techniques, (2) the basis for active learning's efficacy in pedagogical literature, (3) the importance of inclusion in ensuring classroom equity, and (4) how to develop and run a lesson plan which guarantees an inclusive, active learning environment.

Outreach Work at Cornell

During my graduate work, I made educational outreach a central goal of my work. By developing workshops and participating in outreach events, I supported efforts to expand my impact as a graduate researcher beyond lab work, in order to further efforts of diversifying the future of STEM researchers. Working through the outreach wing of Cornell's Biomedical Engineering Society chapter, I worked on outreach programs including Girl Scout Engineering Day and demonstrations at elementary and middle schools throughout Tompkins County, including Caroline Elementary School, Horseheads Middle School, and Dewitt Middle School. Through my work in the Lammerding Lab, I also lead outreach efforts with the CURIE Academy, which encourages young women in high school to pursue careers in STEM, and an Art History Class at Cornell called "BioArt" (ARTH 6151) which highlights the overlap between art and biology, to encourage engagement of artists with biological research. In working as a TA Development Consultant for Cornell's Engineering Learning Initiatives group, I developed workshops which instructed future teaching assistants on methods for ensuring inclusive teaching practices in engineering classrooms, in order to ensure that diversity efforts are supported in higher education as well.

The most substantial of my outreach efforts involved my work with Cornell's Adult University, where I developed and taught two courses for their online Teen and Youth Program: Introduction to Engineering (for 10-12 year old students) and Introduction to Biomedical Engineering (for 13-14 year old students). In this program, adolescent

students from over 10 countries around the world joined these courses online, and participated in a flipped classroom model. A flipped classroom model is a teaching approach which describes an approach where the majority of basic knowledge is acquired prior to class through pre-prepared activities (usually readings and videos) and then students gain practice in applying that knowledge during class time (typically through group activities, or problem-solving exercises) (Bishop & Verleger, 2013). This approach is beneficial to learning as the instructor is able to allocate more class time towards clarifying misconceptions and enabling student participation, than in a traditional classroom, where the majority of class time is dedicated to passive, didactic instruction.

In these courses, students received introductory information about various fields in either engineering or biomedical engineering (during the online “asynchronous” lecture component), and then had the opportunity to apply engineering design techniques during class activities (during synchronous online class-time). Courses were developed using the principles of reverse teaching design. First, learning outcomes are defined based upon what students should be able to do after each learning segment. Next, methods for evaluation are determined which will assess whether or not the learning outcomes have been accomplished. Finally, the course material and activities are selected in order to target those specific outcomes.

Class activities were central to the success of each of these courses. In addition to their importance to students’ metacognition around engineering problem solving,

encouraging activity helped to ensure that all students felt included in class activities. In order to guarantee inclusion during class activities, students were placed into groups with assigned roles. Each group had a leader, a designer, a researcher, and a presenter. This made sure that each student had a responsibility to the group and had the opportunity to participate in class.

“Introduction to Engineering” was structured by the division of the major engineering disciplines, taught separately during each class section (Table A.1). These sections were Civil Engineering, Mechanical Engineering, Electrical and Computer Engineering, Chemical Engineering, and Biomedical Engineering. Speaking generally, the outcomes for each of these lessons were tailored to a young audience with no prior, assumed knowledge of engineering disciplines, as students in this class were all 10-12 years old. Each lesson sought to familiarize students with a new discipline of engineering, and key roles played by these disciplines demonstrated through familiar concepts and products that these engineers are associated with. At least one principle of engineering design was also presented in each section, which students were able to applied through simplified, model design problems which aimed to teach them how basic mathematical or physical principles inform engineering design. These concepts were solidified following design activities, as students were given the opportunity to explain their design process to the class, while I provided feedback which helped them think through how they could continue to improve the design through iteration.

“Introduction to Biomedical Engineering” was structured very similarly to the earlier course (Table A.2). The sections taught in this course were an overview and history of the biomedical engineering field, Orthopedic Biomechanics, Tissue Engineering, Pharmaceutical Engineering, and Medical Robotics. These lessons were targeted at students who may have some familiarity with biology and physics principles, as these students were 13-14 years old. This course sought to expose students to more specific applications of biomedical engineering, based on active research projects (many based on recent publications from Cornell University, and my own work) and biomedical problems which were popularized in recent news events. During synchronous class time, students worked through design problems through the framework of the engineering design process, and were also encouraged to consider the ethical and human factors dimensions of biomedical engineering problems, including design safety, usability, and cost.

Each of these courses were immensely successful, as students reported back with very high reviews of both my teaching and the course content. My overall score based on student feedback for Intro to Engineering and Intro to Biomedical Engineering on a scale of 5 were 4.85 and 4.79, respectively. Overwhelmingly, students particularly noted their enjoyment of the active learning style, and the opportunity to regularly apply lesson content towards design problems.

In terms of critical feedback, the most notable recurring themes were that course content was too complex for the target audience, and that a small group of students did

not find the active learning sections helpful. Though these critical comments contradict the insights from the positive reviews, it is very important to consider how to address these issues in future classes.

Regarding the issue of complexity, I think it would have been beneficial to gather more data from incoming students on their familiarity with engineering subjects before developing the class. This would have enabled me to better target students' skill level based upon what topics I incorporated, and the depth of description I utilized for each topic.

It is a well-documented phenomena that not all students respond equally to specific teaching styles, and this can also apply to active learning. The flipped classroom model aims to ameliorate the issue of differences in learning style by using both the benefits of the didactic lecturing approach and the benefits of in-class activity. It is possible that the negative feedback was suggesting that some students found that the active learning approaches did not enable engagement with the class content, but rather served as a means of "busy work." To better integrate learning concepts into the active components, I could develop worksheets that show both the learning outcomes of each class with a variety of discussion concepts, which encourage students to consider how each step in the in-class activity represents an application of knowledge gained from the lecture.

Table A.1: Outline of Course Contents for CAU Teen and Youth Class “Introduction to Engineering”

| Intro to Engineering Syllabus (10-12 year old students) | | | |
|--|---|--|--|
| Section Topic | Learning Outcomes | Video component | In Class Activity |
| Introduction + Civil Engineering | Describe the importance of engineering in everyday life Explain what Civil Engineering is, and three key functions of Civil Engineers Apply Newton's Laws to the design of a Bridge | Definitions of engineering and introduction to various engineering fields Discussion of Civil Engineering field and key roles of Civil Engineers Description of Newton's Laws, and how they are used to describe forces acting on structures | Personal Introductions Review of Newton's Laws Popsicle stick bridge activity |
| Mechanical Engineering | Describe key roles of Mechanical Engineers Use Newton's Laws to describe how airplanes generate lift Apply understanding of airplane lift into model airplane design | Discussion of Mechanical Engineering roles in design, manufacturing, and aerospace Application of the engineering design process to the product development pipeline Demonstration of how Newton's Laws apply to the generation of airplane lift | Review of aerodynamic forces Discussion of key elements impacting airplane design Model airplane design Activity |
| Electrical + Computer Engineering | Describe how circuits work using Ohm's Law Explain how computers convert electrical signals into "information" | Overview of Ohm's Law and function of circuits Description of how computer chips use circuit principles to generate binary data Demonstration of how binary data is converted to "information" through image processing | Review of concepts from video lecture Barcoding design activity, using principles of binary data and image processing to uniquely identify products |
| Chemical and Environmental Engineering | Describe key roles of C&E Engineers Explain differences in "recyclability" of various materials Identify key factors which influence environmental impact of materials | Discussion of roles of C&E Engineers in pharmaceuticals, food science, and materials science Description of material processing life cycle, and environmental impact | Review of material recycling process Group design activity: Reducing environmental impact of water bottles through materials selection |
| Biomedical Engineering | Describe key roles of Biomedical Engineers List three areas of BME research Apply engineering design principles to a biomedical engineering problem | Discussion of various fields of active BME research Discussion of prosthetic design and biomimesis Case study of current BME research (presenting my own research) | Review of video lecture concepts Robotic finger design activity |

Table A.2: Outline of Course Contents for CAU Teen and Youth Course “Introduction to Biomedical Engineering”

| Intro to Biomedical Engineering Syllabus (13-14 year old students) | | | |
|--|--|--|--|
| Section Topic | Learning Outcomes | Video Component | In Class Activity |
| What is Biomedical Engineering? | Describe what biomedical engineering is List three current areas of biomedical engineering research Explain the purpose of the engineering design process | History of the field, and key roles of Biomedical Engineers Introduction to the engineering design process Case study in engineering design process on hemodialysis machine | Personal introductions Discussion of engineering design process Design activity on assistive mobility devices |
| Orthopedic Biomechanics | Explain what orthopedic biomechanics is, and active problems in this field Define "kinesiology," and describe its application to BME design Identify key components of experimental design, and how they help interpret scientific results | Orthopedic biomechanics applications in arthritis research and sports science Discussion of a current orthopedics research paper, and how researchers designed an experiment to demonstrate efficacy of an arthritis treatment | Review of video lecture Design activity for approaches to treat osteoarthritis Discussion of total hip replacement surgery (tooling and related design issues) |
| Tissue Engineering | Describe how tissues develop through the activity of cells Explain three key biological factors that engineers can manipulate to create tissues from scratch | Description of factors that influence cell behavior (materials, cell type, biological signals) Step-by-step Guide to how to differentiate a tissue (incorporating mechanical and chemical signals) Case study on current tissue engineering research to demonstrate step-by-step guide | Review of components covered in lecture "Design your own tissue/organ" activity using step-by-step guide |
| Pharmaceutical Engineering | Describe the importance of targeted therapies in the future of medicine Identify routes of pharmaceutical administration and key design parameters Apply knowledge of routes of administration towards prescribing treatment to patients | The influence of targeted therapeutics on the efficacy of "futuristic" treatments (e.g. CRISPR) Discussion of routes of administration and pharmaceutical design parameters Application of design principles in development of the COVID-19 vaccine | Review of video lecture Case study: "Uncle Ted's Ever-Evolving Treatment Problem" |
| Medical Robotics | Identify three key challenges of every robotic design problem List three applications of robotics to the medical field Explain human factors that would influence selection of robotic designs | Overview of field of medical robotics and varying applications List key parameters guiding robotic design (Extraction of Intent, Control, Electromechanical Design) Discussion of human factors in prosthetic selection (i.e. safety, cost factors, weight) | Review of key robotic design parameters Design a Robotic Limb Activity |

Nuclear Tracking MATLAB Script

The following MATLAB script was used to track nuclear positioning following laser ablation in the experiments described in Chapter 3.

```
%% Nucleus Tracking Code for Laser Ablation Analysis
% Load czi files
clear all, close all
warning('off', 'all')
addpath('bfmatlab')

%select file/s
[filename, pathname]=uigetfile({'*.czi;*.lsm;*.tif',...
    'Zeiss Files (*.czi,*.lsm,*.tif)'}, 'Select any file in the
folder', 'MultiSelect', 'on');

[pathstr, fname, ext] = fileparts([pathname filename]);
reader = bfGetReader([pathname filename]);
omeMeta = reader.getMetadataStore();
stackSizeX = omeMeta.getPixelsSizeX(0).getValue(); % image width,
pixels
stackSizeY = omeMeta.getPixelsSizeY(0).getValue(); % image height,
pixels
stackSizeZ = omeMeta.getPixelsSizeZ(0).getValue(); % number of Z
slices
stackSizeT = omeMeta.getPixelsSizeT(0).getValue(); % number of time
points
stackSizeC = omeMeta.getPixelsSizeC(0).getValue(); % number of
channels
positionSize = omeMeta.getImageCount(); % number of positions

%LSM/CZI vs TIF
if strcmp(ext, '.lsm') || strcmp(ext, '.czi')
    cameramodel = omeMeta.getDetectorModel(0,0); % Camera Model
    cameramodel = char(cameramodel);
    bit_depth_file = omeMeta.getPixelsSignificantBits(0).getValue();
% bit bepth of file

    %select bit depth based on camera model
    switch cameramodel
        case 'PvCamCoolSNAP_KINO'
            bit_depth_camera = 14;
        case 'PvCamCoolSNAP_HQ'
            bit_depth_camera = 12;
        otherwise
            bit_depth_camera = 16;
    end

    %calculate correction factor for lower bit file in 16bit czi
    if bit_depth_file > bit_depth_camera
        intensity_factor = 2 ^ (bit_depth_file - bit_depth_camera);
    else
        intensity_factor = 1;
    end
end
```

```

        end
    else
        intensity_factor = 1;
    end

    %initiate image matrices
    img_channels = zeros(stackSizeY, stackSizeX, stackSizeT, stackSizeC,
        positionSize, 'double');
    %DNA_im=zeros(stackSizeY, stackSizeX, stackSizeT, 'double');

    % write images to matrix

    for ii = 1:stackSizeT % Cycle through time points
        for j = 1:stackSizeC %Cycle through colors
            count = j + ((ii - 1) * stackSizeC);
            frame = bfGetPlane(reader, count); %read frame
            img_channels(:, :, ii, j) = frame; %write to stack
        end
    end

    for ii = 1:stackSizeT
        g=0;
        Left(ii) = find(any(img_channels(:, :, ii)), 1, 'first');
        Right(ii) = find(any(img_channels(:, :, ii)), 1, 'last');
        A = sum(img_channels(:, :, ii));
        sumA=0;
        sumxA=0;
        for i=1:stackSizeX
            sumxA = sumxA+i*A(i);
            sumA = sumA+A(i);
        end
        Centroid(ii)= sumxA/sumA;
    end
    Left=Left-Left(1);
    Right=Right-Right(1);
    Centroid=Centroid-Centroid(1);
    Left = Left';
    Right = Right';
    Centroid = Centroid';

```


REFERENCES

- Ahmed, W. (2018). Developmental trajectories of math anxiety during adolescence: Associations with STEM career choice. *Journal of Adolescence*, *67*, 158–166. <https://doi.org/10.1016/j.adolescence.2018.06.010>
- Alam, S. G., Lovett, D., Kim, D. I., Roux, K. J., Dickinson, R. B., & Lele, T. P. (2015). The nucleus is an intracellular propagator of tensile forces in NIH 3T3 fibroblasts. *Journal of Cell Science*, *128*(10), 1901–1911. <https://doi.org/10.1242/jcs.161703>
- Allen, T., & Cullis, P. (2004). Drug Delivery Systems: Entering the Mainstream. *Science*, *303*(5665), 1818–1822. <https://doi.org/10.1126/science.1095833>
- Amano, M., Ito, M., Kimura, K., Fukata, Y., Chihara, K., Nakano, T., Matsuura, Y., & Kaibuchi, K. (1996). Phosphorylation and Activation of Myosin by Rho-associated Kinase (Rho-kinase)*. *The Journal of Biological Chemistry*, *271*(34).
- Andreu, I., Granero-Moya, I., Chahare, N. R., Clein, K., Molina-Jordán, M., Beedle, A. E. M., Elosegui-Artola, A., Abenza, J. F., Rossetti, L., Trepát, X., Raveh, B., & Roca-Cusachs, P. (2022). Mechanical force application to the nucleus regulates nucleocytoplasmic transport. *Nature Cell Biology*. <https://doi.org/10.1038/s41556-022-00927-7>
- Archer, L., DeWitt, J., Osborne, J., Dillon, J., Willis, B., & Wong, B. (2012). Science Aspirations, Capital, and Family Habitus: How Families Shape Children’s Engagement and Identification With Science. *American Educational Research Journal*, *49*(5), 881–908. <https://doi.org/10.3102/0002831211433290>
- Arsenovic, P. T., Ramachandran, I., Bathula, K., Zhu, R., Narang, J. D., Noll, N. A., Lemmon, C. A., Gundersen, G. G., & Conway, D. E. (2016). Nesprin-2G, a Component of the Nuclear LINC Complex, Is Subject to Myosin-Dependent Tension. *Biophysical Journal*, *110*(1), 34–43. <https://doi.org/10.1016/j.bpj.2015.11.014>
- Balzer, E. M., Tong, Z., Paul, C. D., Hung, W. C., Stroka, K. M., Boggs, A. E., Martin, S. S., & Konstantopoulos, K. (2012). Physical confinement alters tumor cell adhesion and migration phenotypes. *FASEB Journal*, *26*(10), 4045–4056. <https://doi.org/10.1096/fj.12-211441>
- Bartosh, T. J., & Ylostalo, J. H. (2014). Preparation of Anti-Inflammatory Mesenchymal Stem/Precursor Cells (MSCs) Through Sphere Formation Using Hanging-Drop Culture Technique. *Current Protocols in Stem Cell Biology*, *28*(1), 2B.6.1-2B.6.23. <https://doi.org/https://doi.org/10.1002/9780470151808.sc02b06s28>
- Bell, E. S., Shah, P., Zuela-Sopilniak, N., Kim, D., McGregor, A. L., Isermann, P., Davidson, P. M., Elacqua, J. J., Lakins, J. N., Vahdat, L., Weaver, V. M., Smolka, M. B., Span, P. N., & Lammerding, J. (2021). Low lamin A levels enhance confined cell migration and metastatic capacity in breast cancer. *BioRxiv*. <https://doi.org/10.1101/2021.07.12.451842>
- Bergert, M., Erzberger, A., Desai, R. A., Aspalter, I. M., Oates, A. C., Charras, G., Salbreux, G., & Paluch, E. K. (2015). Force transmission during adhesion-

- independent migration. *Nat Cell Biol*, 17(4), 524–529.
<https://doi.org/10.1038/ncb3134>
- Bishop, J. L., & Verleger, M. A. (2013). The Flipped Classroom: A Survey of the Research. *ASEE*.
- Boltze, J., Arnold, A., Walczak, P., Jolkkonen, J., Cui, L., & Wagner, D.-C. (2015). The Dark Side of the Force – Constraints and Complications of Cell Therapies for Stroke. *Frontiers in Neurology*, 6.
<https://www.frontiersin.org/article/10.3389/fneur.2015.00155>
- Bone, C. R., Chang, Y. T., Cain, N. E., Murphy, S. P., & Starr, D. A. (2016). Nuclei migrate through constricted spaces using microtubule motors and actin networks in *C. elegans* hypodermal cells. *Development*, 143(22), 4193–4202.
- Brunner, C. A., Ehrlicher, A., Kohlstrunk, B., Knebel, D., Käs, J. A., & Goegler, M. (2006). Cell migration through small gaps. *European Biophysics Journal*, 35(8), 713–719. <https://doi.org/10.1007/s00249-006-0079-1>
- Buxboim, A., Swift, J., Irianto, J., Spinler, K. R., Dingal, P. C. D. P., Athirasala, A., Kao, Y. R. C., Cho, S., Harada, T., Shin, J. W., & Discher, D. E. (2014). Matrix elasticity regulates lamin-A,C phosphorylation and turnover with feedback to actomyosin. *Current Biology*, 24(16), 1909–1917.
<https://doi.org/10.1016/j.cub.2014.07.001>
- Caille, N., Thoumine, O., Tardy, Y., & Meister, J. J. (2002). Contribution of the nucleus to the mechanical properties of endothelial cells. *J Biomech*, 35(2), 177–187.
- Cavalier-Smith, T. (2005). Economy, Speed and Size Matter: Evolutionary Forces Driving Nuclear Genome Miniaturization and Expansion. *Annals of Botany*, 95(1), 147–175. <https://doi.org/10.1093/aob/mci010>
- Charras, G., & Paluch, E. (2008). Blebs lead the way: how to migrate without lamellipodia. *Nature Reviews Molecular Cell Biology*.
www.nature.com/reviews/molcellbio
- Charras, G. T., Yarrow, J. C., Horton, M. A., Mahadevan, L., & Mitchison, T. J. (2005). Non-equilibration of hydrostatic pressure in blebbing cells. *Nature*, 435(7040), 365–369. <https://doi.org/10.1038/nature03550>
- Chaw, K. C., Manimaran, M., Tay, F. E. H., & Swaminathan, S. (2006). A quantitative observation and imaging of single tumor cell migration and deformation using a multi-gap microfluidic device representing the blood vessel. *Microvascular Research*, 72(3), 153–160.
<https://doi.org/10.1016/j.mvr.2006.06.003>
- Chen, H.-C. (2005). Boyden Chamber Assay. *Methods in Molecular Biology*, 294.
- Chen, L. (2010). Cytology: Diagnostic Principles and Clinical Correlates. *The American Journal of Surgical Pathology*, 34(2).
https://journals.lww.com/ajsp/Fulltext/2010/02000/Cytology__Diagnostic_Principles_and_Clinical.18.aspx
- Chen, X. (2013). STEM Attrition: College Students' Paths Into and Out of STEM Fields Statistical Analysis Report. In *National Center for Education Statistics*.
- Cheung, B. C. H., Hodgson, L., Segall, J. E., & Wu, M. (2022). Spatial and temporal dynamics of RhoA activities of single breast tumor cells in a 3D environment

- revealed by a machine learning-assisted FRET technique. *Experimental Cell Research*, 410(2), 112939.
<https://doi.org/https://doi.org/10.1016/j.yexcr.2021.112939>
- Chi, Q., Yin, T., Gregersen, H., Deng, X., Fan, Y., Zhao, J., Liao, D., & Wang, G. (2014). Rear actomyosin contractility-driven directional cell migration in three-dimensional matrices: A mechanochemical coupling mechanism. In *Journal of the Royal Society Interface* (Vol. 11, Issue 95). Royal Society.
<https://doi.org/10.1098/rsif.2013.1072>
- Corradetti, B., Taraballi, F., Martinez, J. O., Minardi, S., Basu, N., Bauza, G., Evangelopoulos, M., Powell, S., Corbo, C., & Tasciotti, E. (2017). Hyaluronic acid coatings as a simple and efficient approach to improve MSC homing toward the site of inflammation. *Scientific Reports*, 7(1), 7991.
<https://doi.org/10.1038/s41598-017-08687-3>
- Crisp, M., Liu, Q., Roux, K., Rattner, J. B., Shanahan, C., Burke, B., Stahl, P. D., & Hodzic, D. (2005). Coupling of the nucleus and cytoplasm: Role of the LINC complex. *Journal of Cell Biology*, 172(1), 41–53.
<https://doi.org/10.1083/jcb.200509124>
- Cross, V. L., Zheng, Y., Won Choi, N., Verbridge, S. S., Sutermeister, B. A., Bonassar, L. J., Fischbach, C., & Stroock, A. D. (2010). Dense type I collagen matrices that support cellular remodeling and microfabrication for studies of tumor angiogenesis and vasculogenesis in vitro. *Biomaterials*, 31(33), 8596–8607.
<https://doi.org/10.1016/j.biomaterials.2010.07.072>
- Cui, L., Kerkelä, E., Bakreen, A., Nitzsche, F., Andrzejewska, A., Nowakowski, A., Janowski, M., Walczak, P., Boltze, J., Lukomska, B., & Jolkkonen, J. (2015). The cerebral embolism evoked by intra-arterial delivery of allogeneic bone marrow mesenchymal stem cells in rats is related to cell dose and infusion velocity. *Stem Cell Research & Therapy*, 6(1), 11. <https://doi.org/10.1186/scrt544>
- Damodaran, K., Venkatachalapathy, S., Alisafaei, F., Radhakrishnan, A. v, Sharma Jokhun, D., Shenoy, V. B., & Shivashankar, G. v. (2018). Compressive force induces reversible chromatin condensation and cell geometry-dependent transcriptional response. *Molecular Biology of the Cell*, 29(25), 3039–3051.
<https://doi.org/10.1091/mbc.E18-04-0256>
- Davidson, P. M., Battistella, A., Déjardin, T., Betz, T., Plastino, J., Borghi, N., Cadot, B., & Sykes, C. (2020). Nesprin-2 accumulates at the front of the nucleus during confined cell migration. *EMBO Rep*, 21(7), e49910.
<https://doi.org/10.15252/embr.201949910>
- Davidson, P. M., Denais, C., Bakshi, M. C., & Lammerding, J. (2014). Nuclear deformability constitutes a rate-limiting step during cell migration in 3-D environments. *Cellular and Molecular Bioengineering*, 7(3), 293–306.
<https://doi.org/10.1007/s12195-014-0342-y>
- Davidson, P. M., & Lammerding, J. (2014). Broken nuclei- lamins, nuclear mechanics, and disease. *Trends Cell Bio*, 24(4), 247–256.
- Davidson, P. M., Sliz, J., Isermann, P., Denais, C. M., & Lammerding, J. (2015). Design of a microfluidic device to quantify dynamic intranuclear deformation

- during cell migration through confining environments. *Integr Biol*, 7, 1534–1546.
- de las Heras, J. I., Batrakou, D. G., & Schirmer, E. C. (2013). Cancer biology and the nuclear envelope: A convoluted relationship. In *Seminars in Cancer Biology* (Vol. 23, Issue 2, pp. 125–137). <https://doi.org/10.1016/j.semcancer.2012.01.008>
- Déjardin, T., Carollo, P. S., Sipieter, F., Davidson, P. M., Seiler, C., Cuvelier, D., Cadot, B., Sykes, C., Gomes, E. R., & Borghi, N. (2020). Nesprins are mechanotransducers that discriminate epithelial-mesenchymal transition programs. *Journal of Cell Biology*, 219(10). <https://doi.org/10.1083/JCB.201908036>
- Denais, C. M., Gilbert, R. M., Isermann, P., McGregor, A. L., te Lindert, M., Weigelin, B., Davidson, P. M., Friedl, P., Wolf, K., & Lammerding, J. (2016). Nuclear envelope rupture and repair during cancer cell migration. *Science*, 352(6283), 353–358.
- Desai, S. P., Freeman, D. M., & Voldman, J. (2009). Plastic masters- Rigid Templates for Soft Lithography. *Lab on a Chip*, 9, 1631–1637.
- Devine, M. J., Mierisch, C. M., Jang, E., Anderson, P. C., & Balian, G. (2002). Transplanted bone marrow cells localize to fracture callus in a mouse model. *Journal of Orthopaedic Research*, 20(6), 1232–1239. [https://doi.org/https://doi.org/10.1016/S0736-0266\(02\)00051-7](https://doi.org/https://doi.org/10.1016/S0736-0266(02)00051-7)
- Dewitt, J., & Archer, L. (2017). Communication and Public Engagement Participation in informal science learning experiences: the rich get richer? *International Journal of Science Education, Part B*. <https://doi.org/10.1080/21548455.2017.1360531>
- Doerschuk, C. M., Beyers, N., Coxson, H. O., Wiggs, B., & Hogg, J. C. (1993). Comparison of neutrophil and capillary diameters and their relation to neutrophil sequestration in the lung. *J Appl Physiol*, 74, 3040–3045.
- Doyle, A. D., Petrie, R. J., Kutys, M. L., & Yamada, K. M. (2013). Dimensions in Cell Migration. *Curr Op Cell Bio*, 25(5), 642–649.
- Edens, L. J., White, K. H., Jevtic, P., Li, X., & Levy, D. L. (2013). Nuclear size regulation: from single cells to development and disease. *Trends in Cell Biology*, 23(4), 151–159. <https://doi.org/10.1016/J.TCB.2012.11.004>
- Elacqua, J. J., McGregor, A. L., & Lammerding, J. (2018). Automated analysis of cell migration and nuclear envelope rupture in confined environments. *PLoS ONE*, 13(4). <https://doi.org/10.1371/journal.pone.0195664>
- Elosegui-Artola, A., Andreu, I., Beedle, A. E. M., Lezamiz, A., Uroz, M., Kosmalska, A. J., Oriá, R., Kechagia, J. Z., Rico-Lastres, P., le Roux, A. L., Shanahan, C. M., Trepát, X., Navajas, D., Garcia-Manyes, S., & Roca-Cusachs, P. (2017). Force Triggers YAP Nuclear Entry by Regulating Transport across Nuclear Pores. *Cell*, 171(6), 1397-1410.e14. <https://doi.org/10.1016/j.cell.2017.10.008>
- Fang, R. H., Kroll, A. v, Gao, W., & Zhang, L. (2018). Cell Membrane Coating Nanotechnology. *Advanced Materials*, 30(23), 1706759. <https://doi.org/https://doi.org/10.1002/adma.201706759>

- Fidorra, J., Mielke, Th., Booz, J., & Feinendegen, L. E. (1981). Cellular and nuclear volume of human cells during the cell cycle. *Radiation and Environmental Biophysics*, 19(3), 205–214. <https://doi.org/10.1007/BF01324188>
- Fioranelli, M., & Grazia, R. M. (2014). Twenty-five years of studies and trials for the therapeutic application of IL-10 immunomodulating properties. From high doses administration to low dose medicine new paradigm. *Journal of Integrative Cardiology*. <https://doi.org/10.15761/JIC.1000102>
- Fischer, T., Hayn, A., & Mierke, C. T. (2020). Effect of Nuclear Stiffness on Cell Mechanics and Migration of Human Breast Cancer Cells. *Frontiers in Cell and Developmental Biology*, 8. <https://www.frontiersin.org/article/10.3389/fcell.2020.00393>
- Fischer, U. M., Harting, M. T., Jimenez, F., Monzon-Posadas, W. O., Xue, H., Savitz, S. I., Laine, G. A., & Cox, C. S. (2008). Pulmonary Passage is a Major Obstacle for Intravenous Stem Cell Delivery: The Pulmonary First-Pass Effect. *Stem Cells and Development*, 18(5), 683–692. <https://doi.org/10.1089/scd.2008.0253>
- Friedl, P., Noble, P. B., & Zanker, K. S. (1993). Lymphocyte locomotion in three-dimensional collagen gels Comparison of three quantitative methods for analysing cell trajectories. In *Journal of Immunological Methods* (Vol. 165).
- Frith, J. E., Thomson, B., & Genever, P. G. (2009). Dynamic Three-Dimensional Culture Methods Enhance Mesenchymal Stem Cell Properties and Increase Therapeutic Potential. *Tissue Engineering Part C: Methods*, 16(4), 735–749. <https://doi.org/10.1089/ten.tec.2009.0432>
- Fritz, R. D., Letzelter, M., Reimann, A., Martin, K., Fusco, L., Ritsma, L., Ponsioen, B., EFluri, E., Schulte-Merker, S., van Rheenen, J., & Pertz, O. (2013). A Versatile Toolkit to Produce Sensitive FRET Biosensors to Visualize Signaling in Time and Space. *Science Signaling*, 6(285), rs12–rs12. <https://doi.org/10.1126/scisignal.2004135>
- Gadea, G., de Toledo, M., Anguille, C., & Roux, P. (2007). Loss of p53 promotes RhoA-ROCK-dependent cell migration and invasion in 3D matrices. *Journal of Cell Biology*, 178(1), 23–30. <https://doi.org/10.1083/jcb.200701120>
- Galipeau, J., & Sensébé, L. (2018). Mesenchymal Stromal Cells: Clinical Challenges and Therapeutic Opportunities. *Cell Stem Cell*, 22(6), 824–833. <https://doi.org/10.1016/J.STEM.2018.05.004>
- Geiger, F., Rüdiger, D., Zahler, S., & Engelke, H. (2019). Fiber stiffness, pore size and adhesion control migratory phenotype of MDA-MB-231 cells in collagen gels. *PLoS ONE*, 14(11). <https://doi.org/10.1371/journal.pone.0225215>
- Godec, S., Archer, L., & Dawson, E. (2022). Interested but not being served: mapping young people’s participation in informal STEM education through an equity lens. *Research Papers in Education*, 37(2), 221–248. <https://doi.org/10.1080/02671522.2020.1849365>
- Gollosi, R., Playter, C., Freeman, T. F., Das, P., Raines, T. I., Garretson, J. H., Thurston, D., & McCord, R. P. (2022). Constricted migration is associated with stable 3D genome structure differences in cancer cell. *BioRxiv*, 856583. <https://doi.org/10.1101/856583>

- Gordon, S., Lawson, L., Rabinowitz, S., Crocker, P. R., Morris, L., & Perry, V. H. (1992). Antigen Markers of Macrophage Differentiation in Murine Tissues. In S. W. Russell & S. Gordon (Eds.), *Macrophage Biology and Activation* (pp. 1–37). Springer Berlin Heidelberg. https://doi.org/10.1007/978-3-642-77377-8_1
- Graham, D. M., Andersen, T., Sharek, L., Uzer, G., Rothenberg, K., Hoffman, B. D., Rubin, J., Balland, M., Bear, J. E., & Burrige, K. (2018). Enucleated cells reveal differential roles of the nucleus in cell migration, polarity, and mechanotransduction. *Journal of Cell Biology*, *217*(3), 895–914. <https://doi.org/10.1083/jcb.201706097>
- Guilak, F., Tedrow, J. R., & Burgkart, R. (2000). Viscoelastic properties of the cell nucleus. *Biochemical and Biophysical Research Communications*, *269*(3), 781–786. <https://doi.org/10.1006/bbrc.2000.2360>
- Habig, B., Gupta, P., Levine, B., & Adams, J. (2020). An Informal Science Education Program’s Impact on STEM Major and STEM Career Outcomes. *Research in Science Education*, *50*(3), 1051–1074. <https://doi.org/10.1007/s11165-018-9722-y>
- Han, S., Yan, J. J., Shin, Y., Jeon, J. J., Won, J., Jeong, H. E., Kamm, R. D., Kim, Y. J., & Chung, S. (2012). A versatile assay for monitoring in vivo-like transendothelial migration of neutrophils. *Lab on a Chip*, *12*(20), 3861–3865. <https://doi.org/10.1039/c2lc40445a>
- Han, X., Wang, C., & Liu, Z. (2018). Red Blood Cells as Smart Delivery Systems. *Bioconjugate Chemistry*, *29*(4), 852–860. <https://doi.org/10.1021/acs.bioconjchem.7b00758>
- Harada, T., Swift, J., Irianto, J., Shin, J.-W., Spinler, K. R., Athirasala, A., Diegmiller, R., Dingal, P. C. D. P., Ivanovska, I. L., & Discher, D. E. (2014). Nuclear lamin stiffness is a barrier to 3D migration, but softness can limit survival. *Journal of Cell Biology*, *204*(5), 669–682. <https://doi.org/10.1083/jcb.201308029>
- Hatch, E. M., & Hetzer, M. W. (2016). Nuclear envelope rupture is induced by actin-based nucleus confinement. *Journal of Cell Biology*, *215*(1). <https://doi.org/10.1083/jcb.201603053>
- Hetmanski, J. H. R., de Belly, H., Busnelli, I., Waring, T., Nair, R. v, Sokleva, V., Dobre, O., Cameron, A., Gauthier, N., Lamaze, C., Swift, J., del Campo, A., Starborg, T., Zech, T., Goetz, J. G., Paluch, E. K., Schwartz, J.-M., & Caswell, P. T. (2019). Membrane Tension Orchestrates Rear Retraction in Matrix-Directed Cell Migration. *Developmental Cell*, *51*(4), 460-475.e10. <https://doi.org/https://doi.org/10.1016/j.devcel.2019.09.006>
- Houk, A. R., Jilkine, A., Mejean, C. O., Boltyanskiy, R., Dufresne, E. R., Angenent, S. B., Altschuler, S. J., Wu, L. F., & Weiner, O. D. (2012). Membrane tension maintains cell polarity by confining signals to the leading edge during neutrophil migration. *Cell*, *148*(1–2), 175–188. <https://doi.org/10.1016/j.cell.2011.10.050>
- Hsia, C.-R., McAllister, J., Hasan, O., Judd, J., Lee, S., Agrawal, R., Chang, C.-Y., Soloway, P., & Lammerding, J. (2022). Confined Migration Induces Heterochromatin Formation and Alters Chromatin Accessibility. *BioRxiv*, 2021.09.22.461293. <https://doi.org/10.1101/2021.09.22.461293>

- Huang, Y. L., Tung, C. K., Zheng, A., Kim, B. J., & Wu, M. (2015). Interstitial flows promote amoeboid over mesenchymal motility of breast cancer cells revealed by a three dimensional microfluidic model. *Integrative Biology*, 7(11), 1402–1411. <https://doi.org/10.1039/c5ib00115c>
- Hyduk, S. J., Rullo, J., Cano, A. P., Xiao, H., Chen, M., Moser, M., & Cybulsky, M. I. (2011). Talin-1 and Kindlin-3 Regulate alpha4beta1 Integrin-Mediated Adhesion Stabilization, but Not G Protein-Coupled Receptor-Induced Affinity Upregulation. *The Journal of Immunology*, 187(8), 4360. <https://doi.org/10.4049/jimmunol.1003725>
- Ignowski, J. M., & Schaffer, D. v. (2004). Kinetic analysis and modeling of firefly luciferase as a quantitative reporter gene in live mammalian cells. *Biotechnology and Bioengineering*, 86(7), 827–834. <https://doi.org/https://doi.org/10.1002/bit.20059>
- Infante, E., Castagnino, A., Ferrari, R., Monteiro, P., Agüera-González, S., Paul-Gilloteaux, P., Domingues, M. J., Maiuri, P., Raab, M., Shanahan, C. M., Baffet, A., Piel, M., Gomes, E. R., & Chavrier, P. (2018). LINC complex-Lis1 interplay controls MT1-MMP matrix digest-on-demand response for confined tumor cell migration. *Nat Commun*, 9(1), 2443. <https://doi.org/10.1038/s41467-018-04865-7>
- Irianto, J., Pfeifer, C. R., Bennett, R. R., Xia, Y., Ivanovska, I. L., Liu, A. J., Greenberg, R. A., & Discher, D. E. (2016). Nuclear constriction segregates mobile nuclear proteins away from chromatin. *Molecular Biology of the Cell*, 27(25), 4011–4020. <https://doi.org/10.1091/mbc.E16-06-0428>
- Jacobelli, J., Friedman, R. S., Conti, M. A., Lennon-Dumenil, A. M., Piel, M., Sorensen, C. M., Adelstein, R. S., & Krummel, M. F. (2010). Confinement-optimized three-dimensional T cell amoeboid motility is modulated via myosin IIA-regulated adhesions. *Nature Immunology*, 11(10), 953–961. <https://doi.org/10.1038/ni.1936>
- Jayo, A., Malboubi, M., Antoku, S., Chang, W., Ortiz-Zapater, E., Groen, C., Pfisterer, K., Tootle, T., Charras, G., Gundersen, G. G., & Parsons, M. (2016). Fascin Regulates Nuclear Movement and Deformation in Migrating Cells. *Dev Cell*, 38(4), 371–383.
- Jevtić, P., Edens, L. J., Li, X., Nguyen, T., Chen, P., & Levy, D. L. (2015). Concentration-dependent Effects of Nuclear Lamins on Nuclear Size in Xenopus and Mammalian Cells. *Journal of Biological Chemistry*, 290(46), 27557–27571. <https://doi.org/10.1074/JBC.M115.673798>
- Jorgensen, P., Edgington, N. P., Schneider, B. L., Rupeš, I., Tyers, M., & Futcher, B. (2007). The Size of the Nucleus Increases as Yeast Cells Grow. *Molecular Biology of the Cell*, 18(9), 3523–3532. <https://doi.org/10.1091/mbc.e06-10-0973>
- Jung, J. W., Kwon, M., Choi, J. C., Shin, J. W., Park, I. W., Choi, B. W., & Kim, J. Y. (2013). Familial Occurrence of Pulmonary Embolism after Intravenous, Adipose Tissue-Derived Stem Cell Therapy. *Ymj*, 54(5), 1293–1296. <https://doi.org/10.3349/ymj.2013.54.5.1293>
- Kanellos, G., Zhou, J., Patel, H., Ridgway, R. A., Huels, D., Gurniak, C. B., Sandilands, E., Carragher, N. O., Sansom, O. J., Witke, W., Brunton, V. G., & Frame, M. C. (2015). ADF and Cofilin1 Control Actin Stress Fibers, Nuclear

- Integrity, and Cell Survival. *Cell Reports*, 13(9), 1949–1964.
<https://doi.org/10.1016/J.CELREP.2015.10.056>
- Karp, J. M., & Leng Teo, G. S. (2009). Mesenchymal Stem Cell Homing: The Devil Is in the Details. In *Cell Stem Cell* (Vol. 4, Issue 3, pp. 206–216).
<https://doi.org/10.1016/j.stem.2009.02.001>
- Ketema, M., Kreft, M., Secades, P., Janssen, H., & Sonnenberg, A. (2013). Nesprin-3 connects plectin and vimentin to the nuclear envelope of Sertoli cells but is not required for Sertoli cell function in spermatogenesis. *Molecular Biology of the Cell*, 24(15), 2454–2466. <https://doi.org/10.1091/mbc.E13-02-0100>
- Keys, J., Windsor, A., & Lammerding, J. (2018). Assembly and Use of a Microfluidic Device to Study Cell Migration in Confined Environments. In G. G. Gundersen & H. J. Worman (Eds.), *The LINC Complex: Methods and Protocols* (pp. 101–118). Springer New York. https://doi.org/10.1007/978-1-4939-8691-0_10
- Khatau, S. B., Bloom, R. J., Bajpai, S., Razafsky, D., Zang, S., Giri, A., Wu, P.-H., Marchand, J., Celedon, A., Hale, C. M., Sun, S. X., Hodzic, D., & Wirtz, D. (2012). The distinct roles of the nucleus and nucleus-cytoskeleton connections in three-dimensional cell migration. *Scientific Reports*, 2(1), 488.
<https://doi.org/10.1038/srep00488>
- Kramer, N., Walzl, A., Unger, C., Rosner, M., Krupitza, G., Hengstschlager, M., & Dolznig, H. (2013). In vitro cell migration and invasion assays. *Mutat Res*, 752(1), 10–24.
- Kraning-Rush, C. M., Califano, J. P., & Reinhart-King, C. A. (2012). Cellular Traction Stresses Increase with Increasing Metastatic Potential. *PLOS ONE*, 7(2), e32572-. <https://doi.org/10.1371/journal.pone.0032572>
- Labusca, L., Herea, D. D., & Mashayekhi, K. (2018). Stem cells as delivery vehicles for regenerative medicine-challenges and perspectives. *World Journal of Stem Cells*, 10(5), 43–56. <https://doi.org/10.4252/wjsc.v10.i5.43>
- Lammerding, J. (2011). Mechanics of the nucleus. *Comprehensive Physiology*, 1(2), 783–807. <https://doi.org/10.1002/cphy.c100038>
- Lämmermann, T., Bader, B. L., Monkley, S. J., Worbs, T., Wedlich-Söldner, R., Hirsch, K., Keller, M., Förster, R., Critchley, D. R., Fässler, R., & Sixt, M. (2008). Rapid leukocyte migration by integrin-independent flowing and squeezing. *Nature*, 453(7191), 51–55. <https://doi.org/10.1038/nature06887>
- Lautenschlager, F., & Piel, M. (2012). Microfabricated devices for cell biology: all for one and one for all. *Curr Op Cell Bio*, 25(1), 116–124.
- Lautscham, L. A., Kämmerer, C., Lange, J. R., Kolb, T., Mark, C., Schilling, A., Strissel, P. L., Strick, R., Gluth, C., Rowat, A. C., Metzner, C., & Fabry, B. (2015). Migration in Confined 3D Environments Is Determined by a Combination of Adhesiveness, Nuclear Volume, Contractility, and Cell Stiffness. *Biophysical Journal*, 109(5), 900–913. <https://doi.org/10.1016/j.bpj.2015.07.025>
- Lee, H., Alisafaei, F., Adebawale, K., Chang, J., Shenoy, V. B., & Chaudhuri, O. (2021). The nuclear piston activates mechanosensitive ion channels to generate cell migration paths in confining microenvironments. *Science Advances*, 7(2), eabd4058. <https://doi.org/doi:10.1126/sciadv.abd4058>

- Lee, J., Hale, C. M., Panorchan, P., Khatau, S. B., George, J. P., Tseng, Y., Stewart, C. L., Hodzic, D., & Wirtz, D. (2007). Nuclear Lamin A/C Deficiency Induces Defects in Cell Mechanics, Polarization, and Migration. *Biophysical Journal*, *93*(7), 2542–2552. <https://doi.org/10.1529/BIOPHYSJ.106.102426>
- Legant, W. R., Miller, J. S., Blakely, B. L., Cohen, D. M., Genin, G. M., & Chen, C. S. (2010). Measurement of mechanical tractions exerted by cells in three-dimensional matrices. *Nature Methods*, *7*(12), 969–971. <https://doi.org/10.1038/nmeth.1531>
- Levy, J. R., & Holzbaur, E. L. F. (2008). Dynein drives nuclear rotation during forward progression of motile fibroblasts. *Journal of Cell Science*, *121*(19), 3187–3195. <https://doi.org/10.1242/jcs.033878>
- Levy, O., Zhao, W., Mortensen, L. J., LeBlanc, S., Tsang, K., Fu, M., Phillips, J. A., Sagar, V., Anandakumaran, P., Ngai, J., Cui, C. H., Eimon, P., Angel, M., Lin, C. P., Yanik, M. F., & Karp, J. M. (2013). mRNA-engineered mesenchymal stem cells for targeted delivery of interleukin-10 to sites of inflammation. *Blood*, *122*(14), e23–e32. <https://doi.org/10.1182/blood-2013-04-495119>
- Lin, C., Tao, B., Deng, Y., He, Y., Shen, X., Wang, R., Lu, L., Peng, Z., Xia, Z., & Cai, K. (2019). Matrix promote mesenchymal stromal cell migration with improved deformation via nuclear stiffness decrease. *Biomaterials*, *217*, 119300. <https://doi.org/10.1016/J.BIOMATERIALS.2019.119300>
- Liu, L., Luo, Q., Sun, J., Wang, A., Shi, Y., Ju, Y., Morita, Y., & Song, G. (2017). Decreased nuclear stiffness via FAK-ERK1/2 signaling is necessary for osteopontin-promoted migration of bone marrow-derived mesenchymal stem cells. *Experimental Cell Research*, *355*(2), 172–181. <https://doi.org/10.1016/j.yexcr.2017.04.004>
- Liu, Y.-J., Le Berre, M., Lautenschlaeger, F., Maiuri, P., Callan-Jones, A., Heuzé, M., Takaki, T., Voituriez, R., & Piel, M. (2015). Confinement and Low Adhesion Induce Fast Amoeboid Migration of Slow Mesenchymal Cells. *Cell*, *160*(4), 659–672. <https://doi.org/https://doi.org/10.1016/j.cell.2015.01.007>
- Lomakin, A. J., Cattin, C. J., Cuvelier, D., Alraies, Z., Molina, M., Nader, G. P. F., Srivastava, N., Saez, P. J., Garcia-Arcos, J. M., Zhitnyak, I. Y., Bhargava, A., Driscoll, M. K., Welf, E. S., Fiolka, R., Petrie, R. J., de Silva, N. S., González-Granado, J. M., Manel, N., Lennon-Duménil, A. M., ... Piel, M. (2020). The nucleus acts as a ruler tailoring cell responses to spatial constraints. *Science*, *370*(6514). <https://doi.org/10.1126/science.aba2894>
- Lombardi, M. L., Jaalouk, D. E., Shanahan, C. M., Burke, B., Roux, K. J., & Lammerding, J. (2011). The interaction between nesprins and sun proteins at the nuclear envelope is critical for force transmission between the nucleus and cytoskeleton. *Journal of Biological Chemistry*, *286*(30), 26743–26753. <https://doi.org/10.1074/jbc.M111.233700>
- Lorentzen, A., Bamber, J., Sadok, A., Elson-Schwab, I., & Marshall, C. J. (2011). An ezrin-rich, rigid uropod-like structure directs movement of amoeboid blebbing cells. *Journal of Cell Science*, *124*(8), 1256–1267. <https://doi.org/10.1242/jcs.074849>

- Lu, W., Schneider, M., Neumann, S., Jaeger, V.-M., Taranum, S., Munck, M., Cartwright, S., Richardson, C., Carthew, J., Noh, K., Goldberg, M., Noegel, A. A., & Karakesisoglou, I. (2012). Nesprin interchain associations control nuclear size. *Cellular and Molecular Life Sciences*, *69*(20), 3493–3509. <https://doi.org/10.1007/s00018-012-1034-1>
- Lu, X. bin, Liu, L., Cheng, C., Yu, B., Xiong, L., Hu, K., Tang, J., Zeng, L., & Sang, Y. (2015). SUN2 exerts tumor suppressor functions by suppressing the Warburg effect in lung cancer. *Scientific Reports*, *5*. <https://doi.org/10.1038/srep17940>
- Lyerly, H. K., Osada, T., & Hartman, Z. C. (2019). Right Time and Place for IL12: Targeted Delivery Stimulates Immune Therapy. *Clinical Cancer Research*, *25*(1), 9–11. <https://doi.org/10.1158/1078-0432.CCR-18-2819>
- Maeda, Y. T., Inose, J., Matsuo, M. Y., Iwaya, S., & Sano, M. (2008). Ordered patterns of cell shape and orientational correlation during spontaneous cell migration. *PLoS ONE*, *3*(11). <https://doi.org/10.1371/journal.pone.0003734>
- Malawista, S. E., van Blaricom, G., & Breitenstein, M. G. (1989). Cryopreservable neutrophil surrogates. Stored cytoplasts from human polymorphonuclear leukocytes retain chemotactic, phagocytic, and microbicidal function. *Journal of Clinical Investigation*, *83*(2), 728–732. <https://doi.org/10.1172/JCI113939>
- Marks, P. C., & Petrie, R. J. (2022). Push or pull: how cytoskeletal crosstalk facilitates nuclear movement through 3D environments. *Phys Biol*, *19*(2). <https://doi.org/10.1088/1478-3975/ac45e3>
- Marks, P. W., Witten, C. M., & Califf, R. M. (2016). Clarifying Stem-Cell Therapy's Benefits and Risks. *New England Journal of Medicine*, *376*(11), 1007–1009. <https://doi.org/10.1056/NEJMp1613723>
- Martini, F. J., & Valdeolmillos, M. (2010). Actomyosin contraction at the cell rear drives nuclear translocation in migrating cortical interneurons. *Journal of Neuroscience*, *30*(25), 8660–8670. <https://doi.org/10.1523/JNEUROSCI.1962-10.2010>
- McGregor, A. L., Hsia, C., & Lammerding, J. (2016). Squish and squeeze- the nucleus as a physical barrier during migration in confined environments. *Curr Op Cell Bio*, *40*, 32–40.
- Mistriotis, P., Wisniewski, E. O., Bera, K., Keys, J., Li, Y., Tuntithavornwat, S., Law, R. A., Perez-Gonzalez, N. A., Erdogmus, E., Zhang, Y., Zhao, R., Sun, S. X., Kalab, P., Lammerding, J., & Konstantopoulos, K. (2019). Confinement hinders motility by inducing RhoA-mediated nuclear influx, volume expansion, and blebbing. *J Cell Biol*, *218*(12), 4093–4111. <https://doi.org/10.1083/jcb.201902057>
- Mosalaganti, S., Obarska-Kosinska, A., Siggel, M., Taniguchi, R., Turoňová, B., Zimmerli, C. E., Buczak, K., Schmidt, F. H., Margiotta, E., Mackmull, M.-T., Hagen, W. J. H., Hummer, G., Kosinski, J., & Beck, M. (2022). AI-based structure prediction empowers integrative structural analysis of human nuclear pores. *Science*, *376*(6598), eabm9506. <https://doi.org/10.1126/science.abm9506>
- Mulligan, J. A., Feng, X., & Adie, S. G. (2019). Quantitative reconstruction of time-varying 3D cell forces with traction force optical coherence microscopy. *Scientific Reports*, *9*(1). <https://doi.org/10.1038/s41598-019-40608-4>

- Nader, G. P. de F., Agüera-Gonzalez, S., Routet, F., Gratia, M., Maurin, M., Cancila, V., Cadart, C., Palamidessi, A., Ramos, R. N., San Roman, M., Gentili, M., Yamada, A., Williard, A., Lodillinsky, C., Lagoutte, E., Villard, C., Viovy, J. L., Tripodo, C., Galon, J., ... Piel, M. (2021). Compromised nuclear envelope integrity drives TREX1-dependent DNA damage and tumor cell invasion. *Cell*, *184*(20), 5230-5246.e22. <https://doi.org/10.1016/j.cell.2021.08.035>
- Neumann, F. R., & Nurse, P. (2007). Nuclear size control in fission yeast. *Journal of Cell Biology*, *179*(4), 593–600. <https://doi.org/10.1083/jcb.200708054>
- Nitzsche, F., Müller, C., Lukomska, B., Jolkkonen, J., Deten, A., & Boltze, J. (2017). MSC Adhesion Cascade—Insights into Homing and Transendothelial Migration. *Stem Cells*, *35*(6), 1446–1460. <https://doi.org/10.1002/stem.2614>
- Norden, C., Young, S., Link, B. A., & Harris, W. A. (2009). Actomyosin Is the Main Driver of Interkinetic Nuclear Migration in the Retina. *Cell*, *138*(6), 1195–1208. <https://doi.org/10.1016/j.cell.2009.06.032>
- Nowakowski, A., Andrzejewska, A., Janowski, M., Walczak, P., & Lukomska, B. (2013). Genetic engineering of stem cells for enhanced therapy. *Acta Neurobiologiae Experimentalis*, *73*(1), 1–18.
- Paul, C. D., Mistriotis, P., & Konstantopoulos, K. (2017). Cancer cell motility: lessons from migration in confined spaces. *Nature Reviews Cancer*, *17*(2), 131–140. <https://doi.org/10.1038/nrc.2016.123>
- Pertz, O., Hodgson, L., Klemke, R. L., & Hahn, K. M. (2006). Spatiotemporal dynamics of RhoA activity in migrating cells. *Nature*, *440*(7087), 1069–1072. <https://doi.org/10.1038/nature04665>
- Petrie, R. J., Harlin, H. M., Korsak, L. I. T., & Yamada, K. M. (2016). Activating the nuclear piston mechanism of 3D migration in tumor cells. *Journal of Cell Biology*, *216*(1), 93–100. <https://doi.org/10.1083/jcb.201605097>
- Petrie, R. J., Koo, H., & Yamada, K. M. (2014). Generation of compartmentalized pressure by a nuclear piston governs cell motility in a 3D matrix. *Science*, *342*(6200), 1062–1065.
- Poincloux, R., Collin, O., Lizárraga, F., Romao, M., Debray, M., Piel, M., & Chavrier, P. (2011). Contractility of the cell rear drives invasion of breast tumor cells in 3D Matrigel. *Proceedings of the National Academy of Sciences*, *108*(5), 1943–1948. <https://doi.org/doi:10.1073/pnas.1010396108>
- Provenzano, P. P., Inman, D. R., Eliceiri, K. W., Trier, S. M., & Keely, P. J. (2008). Contact guidance mediated three-dimensional cell migration is regulated by Rho/ROCK-dependent matrix reorganization. *Biophysical Journal*, *95*(11), 5374–5384. <https://doi.org/10.1529/biophysj.108.133116>
- Qin, D., Xia, Y., & Whitesides, G. M. (2010). Soft lithography for micro- and nanoscale patterning. *Nature Protocols*, *5*(3), 491–503.
- Raab, M., & Discher, D. E. (2017). Matrix rigidity regulates microtubule network polarization in migration. *Cytoskeleton*, *74*(3), 114–124. <https://doi.org/10.1002/cm.21349>
- Raab, M., Gentili, M., de Belly, H., Thiam, H.-R., Vargas, P., Jimenez Ana, J., Lautenschlaeger, F., Voituriez, R., Lennon-Duménil, A.-M., Manel, N., & Piel, M. (2016). ESCRT III repairs nuclear envelope ruptures during cell migration to

- limit DNA damage and cell death. *Science*, 352(6283), 359–362.
<https://doi.org/10.1126/science.aad7611>
- Renkawitz, J., Kopf, A., Stopp, J., de Vries, I., Driscoll, M. K., Merrin, J., Hauschild, R., Welf, E. S., Danuser, G., Fiolka, R., & Sixt, M. (2019). Nuclear positioning facilitates amoeboid migration along the path of least resistance. *Nature*, 568(7753), 546–550. <https://doi.org/10.1038/s41586-019-1087-5>
- Ridley, A. J., Schwartz, M. A., Burridge, K., Firtel, R. A., Ginsberg, M. H., Borisy, G., Thomas Parsons, J., & Rick Horwitz, A. (2003). Cell Migration: Integrating Signals from Front to Back. In *Annu. Rev. Plant Physiol. Plant Mol. Biol* (Vol. 143). H. Hashimoto. <https://doi.org/10.1126/science.1092053>
- Rowat, A. C., Jaalouk, D. E., Zwerger, M., Ung, W. L., Eydelnant, I. A., Olins, D. E., Olins, A. L., Herrmann, H., Weitz, D. A., & Lammerding, J. (2013). Nuclear Envelope Composition Determines the Ability of Neutrophil-type Cells to Passage through Micron-scale Constrictions*. *Journal of Biological Chemistry*, 288(12), 8610–8618. <https://doi.org/https://doi.org/10.1074/jbc.M112.441535>
- Ruprecht, V., Wieser, S., Callan-Jones, A., Smutny, M., Morita, H., Sako, K., Barone, V., Ritsch-Marte, M., Sixt, M., Voituriez, R., & Heisenberg, C.-P. (2015). Cortical Contractility Triggers a Stochastic Switch to Fast Amoeboid Cell Motility. *Cell*, 160(4), 673–685.
<https://doi.org/https://doi.org/10.1016/j.cell.2015.01.008>
- Sackstein, R. (2005). The lymphocyte homing receptors: gatekeepers of the multistep paradigm. *Current Opinion in Hematology*, 12(6). https://journals.lww.com/co-hematology/Fulltext/2005/11000/The_lymphocyte_homing_receptors_gatekeepers_of.3.aspx
- Sadler, P. M., Sonnert, G., Hazari, Z., & Tai, R. (2012). Stability and volatility of STEM career interest in high school: A gender study. *Science Education*, 96(3), 411–427. <https://doi.org/10.1002/sce.21007>
- Sahai, E., & Marshall, C. J. (2003). Differing modes of tumour cell invasion have distinct requirements for Rho/ROCK signalling and extracellular proteolysis. *Nat Cell Biol*, 5(8), 711–719. <https://doi.org/10.1038/ncb1019>
- Samanta, S., Rajasingh, S., Drosos, N., Zhou, Z., Dawn, B., & Rajasingh, J. (2018). Exosomes: new molecular targets of diseases. *Acta Pharmacologica Sinica*, 39(4), 501–513. <https://doi.org/10.1038/aps.2017.162>
- Sao, K., Jones, T. M., Doyle, A. D., Maity, D., Schevzov, G., Chen, Y., Gunning, P. W., & Petrie, R. J. (2019). Myosin II governs intracellular pressure and traction by distinct tropomyosin-dependent mechanisms. *Molecular Biology of the Cell*, 30(10), 1170–1181. <https://doi.org/10.1091/mbc.E18-06-0355>
- Schaar, B. T., & McConnell, S. K. (2005). Cytoskeletal coordination during neuronal migration. *PNAS*, 102. www.pnas.org/cgi/doi/10.1073/pnas.0506008102
- Shah, P., Hobson, C. M., Cheng, S., Colville, M. J., Paszek, M. J., Superfine, R., & Lammerding, J. (2021). Nuclear Deformation Causes DNA Damage by Increasing Replication Stress. *Current Biology*, 31(4), 753-765.e6.
<https://doi.org/10.1016/j.cub.2020.11.037>
- Sharma, V. P., Williams, J., Leung, E., Sanders, J., Eddy, R., Castracane, J., Oktay, M. H., Entenberg, D., & Condeelis, J. S. (2021). Sun-mk11 crosstalk regulates

- nuclear deformation and fast motility of breast carcinoma cells in fibrillar ecm microenvironment. *Cells*, 10(6). <https://doi.org/10.3390/cells10061549>
- Shay, J. W. (1987). Cell enucleation, cybrids, reconstituted cells, and nuclear hybrids. *Methods in Enzymology*, 151(C), 221–237. [https://doi.org/10.1016/S0076-6879\(87\)51020-5](https://doi.org/10.1016/S0076-6879(87)51020-5)
- Stewart, M. (2007). Molecular mechanism of the nuclear protein import cycle. *Nature Reviews Molecular Cell Biology*, 8(3), 195–208. <https://doi.org/10.1038/nrm2114>
- Stewart-Hutchinson, P. J., Hale, C. M., Wirtz, D., & Hodzic, D. (2008). Structural requirements for the assembly of LINC complexes and their function in cellular mechanical stiffness. *Experimental Cell Research*, 314(8), 1892–1905. <https://doi.org/10.1016/j.yexcr.2008.02.022>
- Stossel, T. P. (1993). On the crawling of animal cells. *Science (New York, N.Y.)*, 260(5111), 1086–1094. <https://doi.org/10.1126/science.8493552>
- Stroka, K. M., Jiang, H., Chen, S. H., Tong, Z., Wirtz, D., Sun, S. X., & Konstantopoulos, K. (2014). Water permeation drives tumor cell migration in confined microenvironments. *Cell*, 157(3), 611–623. <https://doi.org/10.1016/j.cell.2014.02.052>
- Takaki, T., Montagner, M., Serres, M. P., le Berre, M., Russell, M., Collinson, L., Szuhai, K., Howell, M., Boulton, S. J., Sahai, E., & Petronczki, M. (2017). Actomyosin drives cancer cell nuclear dysmorphia and threatens genome stability. *Nature Communications*, 8. <https://doi.org/10.1038/ncomms16013>
- te Boekhorst, V., & Friedl, P. (2016). Plasticity of Cancer Cell Invasion—Mechanisms and Implications for Therapy. In *Advances in Cancer Research* (Vol. 132, pp. 209–264). Academic Press Inc. <https://doi.org/10.1016/bs.acr.2016.07.005>
- Thanuja M.Y., Anupama C., & Ranganath, S. H. (2018). Bioengineered cellular and cell membrane-derived vehicles for actively targeted drug delivery: So near and yet so far. *Advanced Drug Delivery Reviews*, 132, 57–80. <https://doi.org/https://doi.org/10.1016/j.addr.2018.06.012>
- Thiam, H. R., Vargas, P., Carpi, N., Crespo, C. L., Raab, M., Terriac, E., King, M. C., Jacobelli, J., Alberts, A. S., Stradal, T., Lennon-Dumenil, A. M., & Piel, M. (2016). Perinuclear Arp2/3-driven actin polymerization enables nuclear deformation to facilitate cell migration through complex environments. *Nature Communications*, 7. <https://doi.org/10.1038/ncomms10997>
- Thomas, D. G., Yenepalli, A., Denais, C. M., Rape, A., Beach, J. R., Wang, Y.-L., Schiemann, W. P., Baskaran, H., Lammerding, J., & Egelhoff, T. T. (2015). Non-muscle myosin IIB is critical for nuclear translocation during 3D invasion. *J Cell Biol*, 210, 583–594.
- Thomas, J. B., Joni, H. Y., Mohammadipoor, A., Bazhanov, N., Coble, K., Claypool, K., Lee Ryang, H., Choi, H., & Darwin, J. P. (2010). Aggregation of human mesenchymal stromal cells (MSCs) into 3D spheroids enhances their antiinflammatory properties. *Proceedings of the National Academy of Sciences*, 107(31), 13724–13729. <https://doi.org/10.1073/pnas.1008117107>
- Tinevez, J.-Y., Schulze, U., Salbreux, G., Roensch, J., Joanny, J.-F., & Paluch, E. (2009). Role of cortical tension in bleb growth. *Proceedings of the National*

- Academy of Sciences*, 106(44), 18581–18586.
<https://doi.org/doi:10.1073/pnas.0903353106>
- Tollis, S., Rizzotto, A., Pham, N. T., Koivukoski, S., Sivakumar, A., Shave, S., Wildenhain, J., Zuleger, N., Keys, J. T., Culley, J., Zheng, Y., Lammerding, J., Carragher, N. O., Brunton, V. G., Latonen, L., Auer, M., Tyers, M., & Schirmer, E. C. (2022). Chemical Interrogation of Nuclear Size Identifies Compounds with Cancer Cell Line-Specific Effects on Migration and Invasion. *ACS Chemical Biology*, 17(3), 680–700. <https://doi.org/10.1021/acscchembio.2c00004>
- Tong, Z., Balzer, E. M., Dallas, M. R., Hung, W. C., Stebe, K. J., & Konstantopolous, K. (2012). Chemotaxis of cell populations through confined spaces at single-cell resolution. *PLoS One*, 7, 1–10.
- Tsai, J. W., Lian, W. N., Kemal, S., Kriegstein, A. R., & Vallee, R. B. (2010). Kinesin 3 and cytoplasmic dynein mediate interkinetic nuclear migration in neural stem cells. *Nature Neuroscience*, 13(12), 1463–1472. <https://doi.org/10.1038/nn.2665>
- Ullah, M., Liu, D. D., & Thakor, A. S. (2019). Mesenchymal Stromal Cell Homing: Mechanisms and Strategies for Improvement. *IScience*, 15, 421–438. <https://doi.org/10.1016/J.ISCI.2019.05.004>
- van Helvert, S., Storm, C., & Friedl, P. (2018). Mechanoreciprocity in cell migration. *Nature Cell Biology*, 20(1), 8–20. <https://doi.org/10.1038/s41556-017-0012-0>
- Vanessa, C. C., Yamamoto, D., Ketna, G. K., Vanessa, D. A., Maria, C. F., Renato, A. M., Yoshida, N., Julia, M. A. M., & Rabinovitch, M. (2007). Enucleated L929 Cells Support Invasion, Differentiation, and Multiplication of *Trypanosoma cruzi* Parasites. *Infection and Immunity*, 75(8), 3700–3706. <https://doi.org/10.1128/IAI.00194-07>
- Veltri, R. W., & Christudass, C. S. (2014). Nuclear morphometry, epigenetic changes, and clinical relevance in prostate cancer. *Advances in Experimental Medicine and Biology*, 773, 77–99. https://doi.org/10.1007/978-1-4899-8032-8_4
- Vennin, C., Rath, N., Pajic, M., Olson, M. F., & Timpson, P. (2020). Targeting ROCK activity to disrupt and prime pancreatic cancer for chemotherapy. In *Small GTPases* (Vol. 11, Issue 1, pp. 45–52). Taylor and Francis Inc. <https://doi.org/10.1080/21541248.2017.1345712>
- Wang, H., Alarcón, C. N., Liu, B., Watson, F., Searles, S., Lee, C. K., Keys, J., Pi, W., Allen, D., Lammerding, J., Bui, J. D., & Klemke, R. L. (2021). Genetically engineered and enucleated human mesenchymal stromal cells for the targeted delivery of therapeutics to diseased tissue. *Nature Biomedical Engineering*. <https://doi.org/10.1038/s41551-021-00815-9>
- Wang, P., Dreger, M., Madrazo, E., Craig, J. W., Samaniego, R., Nigel, W. H., Monroy, F., Baena, E., Sánchez-Mateos, P., Hurlstone, A., & Redondo-Muñoz, J. (2018). WDR5 modulates cell motility and morphology and controls nuclear changes induced by a 3D environment. *Proceedings of the National Academy of Sciences*, 115(34), 8581–8586. <https://doi.org/10.1073/pnas.1719405115>
- Weigel, B., Bakker, G.-J., & Friedl, P. (2012). Intravital third harmonic generation microscopy of collective melanoma cell invasion. *IntraVital*, 1(1), 32–43. <https://doi.org/10.4161/intv.21223>

- Wiggan, O., Schroder, B., Krapf, D., Bamburg, J. R., & DeLuca, J. G. (2017). Cofilin Regulates Nuclear Architecture through a Myosin-II Dependent Mechanotransduction Module. *Scientific Reports*, 7(1), 40953. <https://doi.org/10.1038/srep40953>
- Wigler, M. H., Neugut, A. I., & Weinstein, I. B. (1976). Chapter 7 Eucleation of Mammalian Cells in Suspension. *Methods in Cell Biology*, 14(C), 87–93. [https://doi.org/10.1016/S0091-679X\(08\)60471-9](https://doi.org/10.1016/S0091-679X(08)60471-9)
- Wirtz, D., Konstantopoulos, K., & Searson, P. C. (2011). The physics of cancer: the role of physical interactions and mechanical forces in metastasis. *Nature Reviews Cancer*, 11(7), 512–522. <https://doi.org/10.1038/nrc3080>
- Wolbank, S., Stadler, G., Peterbauer, A., Gillich, A., Karbiener, M., Streubel, B., Wieser, M., Katinger, H., van Griensven, M., Redl, H., Gabriel, C., Grillari, J., & Grillari-Voglauer, R. (2009). Telomerase Immortalized Human Amnion- and Adipose-Derived Mesenchymal Stem Cells: Maintenance of Differentiation and Immunomodulatory Characteristics. *Tissue Engineering Part A*, 15(7), 1843–1854. <https://doi.org/10.1089/ten.tea.2008.0205>
- Wolf, K., Mazo, I., Leung, H., Engelke, K., von Andrian, U. H., Deryugina, E. I., Strongin, A. Y., Bröcker, E. B., & Friedl, P. (2003). Compensation mechanism in tumor cell migration: Mesenchymal-amoeboid transition after blocking of pericellular proteolysis. *Journal of Cell Biology*, 160(2), 267–277. <https://doi.org/10.1083/jcb.200209006>
- Wolf, K., te Lindert, M., Krause, M., Alexander, S., te Riet, J., Willis, L. A., Hoffman, R. M., Figdor, C. G., Weiss, S. J., & Friedl, P. (2013). Physical limits of cell migration: control ECM space and nuclear deformation and tuning by proteolysis and traction force. *J Cell Biol*, 201, 1069–1084.
- Wu, J., Kent, I. A., Shekhar, N., Chancellor, T. J., Mendonca, A., Dickinson, R. B., & Lele, T. P. (2014). Actomyosin pulls to advance the nucleus in a migrating tissue cell. *Biophysical Journal*, 106(1), 7–15. <https://doi.org/10.1016/j.bpj.2013.11.4489>
- Wu, J., Lee, K. C., Dickinson, R. B., & Lele, T. P. (2011). How dynein and microtubules rotate the nucleus. *Journal of Cellular Physiology*, 226(10), 2666–2674. <https://doi.org/10.1002/jcp.22616>
- Xia, Y., Ivanovska, I. L., Zhu, K., Smith, L., Irianto, J., Pfeifer, C. R., Alvey, C. M., Ji, J., Liu, D., Cho, S., Bennett, R. R., Liu, A. J., Greenberg, R. A., & Discher, D. E. (2018). Nuclear rupture at sites of high curvature compromises retention of DNA repair factors. *Journal of Cell Biology*, 217(11), 3796–3808. <https://doi.org/10.1083/jcb.201711161>
- Yadav, S. K., Feigelson, S. W., Roncato, F., Antman-Passig, M., Shefi, O., Lammerding, J., & Alon, R. (2018). Frontline Science: Elevated nuclear lamin A is permissive for granulocyte transendothelial migration but not for motility through collagen I barriers. *Journal of Leukocyte Biology*, 104(2), 239–251. <https://doi.org/https://doi.org/10.1002/JLB.3HI1217-488R>
- Yamada, K. M., & Sixt, M. (2019). Mechanisms of 3D cell migration. *Nature Reviews Molecular Cell Biology*, 20(12), 738–752. <https://doi.org/10.1038/s41580-019-0172-9>

- Yanakieva, I., Erzberger, A., Matejčić, M., Modes, C. D., & Norden, C. (2019). Cell and tissue morphology determine actin-dependent nuclear migration mechanisms in neuroepithelia. *Journal of Cell Biology*, 218(10), 3272–3289. <https://doi.org/10.1083/JCB.201901077>
- Yip, A. K., Chiam, K. H., & Matsudaira, P. (2015). Traction stress analysis and modeling reveal that amoeboid migration in confined spaces is accompanied by expansive forces and requires the structural integrity of the membrane-cortex interactions. *Integrative Biology*, 7(10), 1196–1211. <https://doi.org/10.1039/c4ib00245h>
- Yoo, J. W., Irvine, D. J., Discher, D. E., & Mitragotri, S. (2011). Bio-inspired, bioengineered and biomimetic drug delivery carriers. In *Nature Reviews Drug Discovery* (Vol. 10, Issue 7, pp. 521–535). <https://doi.org/10.1038/nrd3499>
- Yoo, J.-W., Irvine, D. J., Discher, D. E., & Mitragotri, S. (2011). Bio-inspired, bioengineered and biomimetic drug delivery carriers. *Nature Reviews Drug Discovery*, 10(7), 521–535. <https://doi.org/10.1038/nrd3499>
- Zhu, R., Antoku, S., & Gundersen, G. G. (2017). Centrifugal Displacement of Nuclei Reveals Multiple LINC Complex Mechanisms for Homeostatic Nuclear Positioning. *Current Biology*, 27(20), 3097-3110.e5. <https://doi.org/10.1016/j.cub.2017.08.073>